

Supporting Information

The Effect of Twisting on the Capture and Release of Singlet Oxygen by Tethered Twisted Acenes

Anjan Bedi, Amit Manor Armon and Ori Gidron*

*Institute of Chemistry, The Hebrew University of Jerusalem, Edmond J. Safra Campus,
Jerusalem, Israel.

Table of Contents

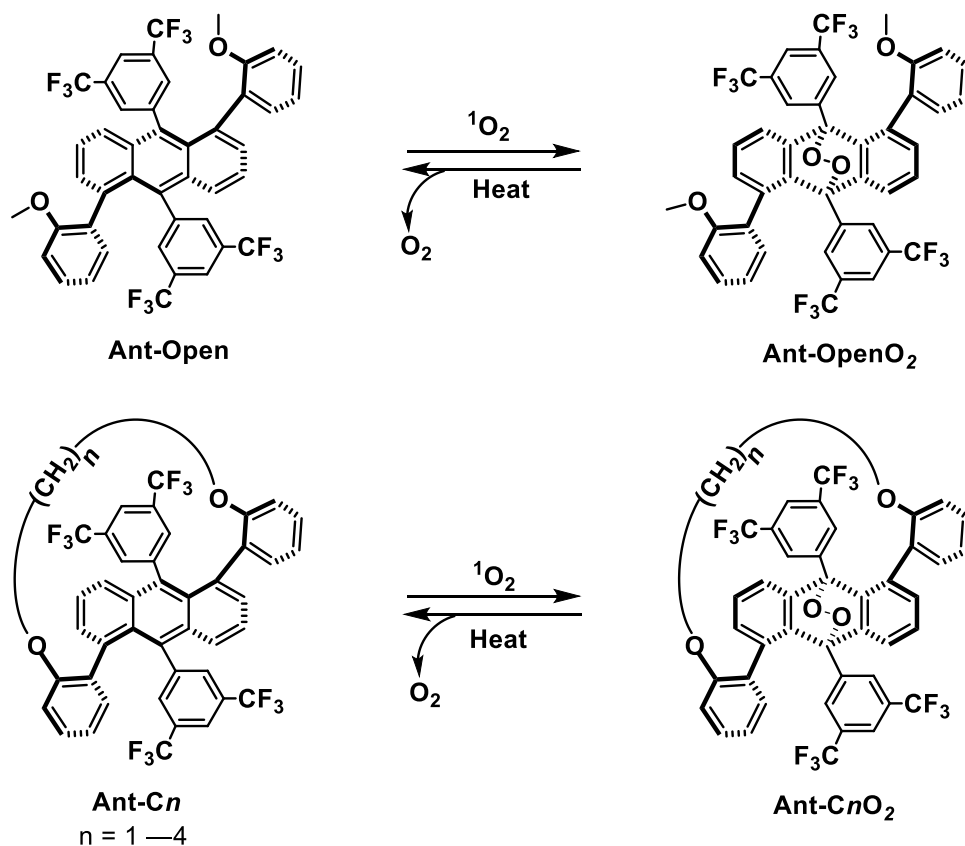
S1 General.....	3
S2 Synthesis	4
Scheme S1. Synthetic route to the peroxides.....	4
General procedure for the photochemical synthesis of Ant- <i>C_n</i> -O ₂	4
S2.1 Synthesis of Ant-open-O ₂	5
S2.2 Synthesis of Ant-C6-O ₂	6
S2.3 Synthesis of Ant-C5-O ₂	7
S2.4 Synthesis of Ant-C4-O ₂	8
S2.5 Synthesis of Ant-C3-O ₂	9
S3 Characterization.....	10
S3.1 Characterization of Ant-Open-O ₂	10
S3.2 Characterization of Ant-C6O ₂	16
S3.3 Characterization of Ant-C5-O ₂	21
S3.4 Characterization of Ant-C4-O ₂	26
S3.5 Characterization of Ant-C3-O ₂	31
S3.6 HRMS investigation to non-quantitative photo-oxidation for Ant-Open-O ₂	36
S3.7 HRMS investigation to non-quantitative photo-oxidation for Ant-C3-O ₂	37
S4 Time-dependent photo-oxidation of anthracenes	37
S4.1 Photo-oxidation studied at different wavelengths	37
S4.2 Photo-oxidation kinetics	40
S4.3 Low temperature photoswitching of Ant-C4.....	43
S4.4 High temperature photoswitching of Ant-C4	44
S5 UV-vis absorption spectra of the peroxides.....	45
S6 Kinetics of the thermal retro Diels-Alder reaction of the twistacene peroxides.....	46
S7 Single crystal X-ray diffraction crystallography (SCXRD)	52
S8 Computational analysis of the twistacene peroxides.....	54
Effect of tether on strain in the tethered anthracene-peroxide core	58
S9 References.....	62

S1 General

All reagent grade solvents were used as purchased without further purification. Members of the **Ant-C_n** series were synthesized according to our previous report.^[1] Photochemical reactions were performed using a Kessil® PR160–427 nm light source from DiCon Fiberoptics Inc. Flash chromatography (FC) was performed using CombiFlash EZ-Prep, using SiO₂ columns. The gradual photochemical reaction profile over time was followed by irradiating the twistacenes in a Spectroline® fluorescence analysis cabinet (model CM-10A) from Spectronics Corporation, USA. For photo/thermal switching studies of twistacenes/endoperoxides, absorbance was measured at the longest wavelength vibronic shoulder, because these species exhibit maximal optical contrast at that wavelength. ¹H-NMR and ¹³C-NMR spectra were recorded on Bruker AV 400 and Bruker AV 500 spectrometers in chloroform-*d* (CDCl₃) and kinetic measurements were performed in 1,1,2,2-tetrachloroethane-*d*₂ (C₂D₂Cl₄). Residual solvent peaks were used as internal references. The actual sample temperatures were accurately measured using an external standard (78.96 wt% ethylene glycol in dimethyl sulfoxide-*d*₆ (DMSO-*d*₆)). UV-vis absorption spectra were recorded using an Agilent Cary-5000 spectrophotometer. The spectra were measured using a quartz cuvette (1 cm) at 25 °C. The absorption wavelengths are reported in nm with the extinction coefficient ϵ (M⁻¹cm⁻¹) in brackets. The kinetics of photo-oxidation were measured under ambient conditions using the previously mentioned Kessil PR160–427 nm light source at 10% intensity. High resolution mass spectra were analyzed on an Agilent HR Q-TOF-MS mass spectrometer using the dual-ESI technique operating in the positive mode.

S2 Synthesis

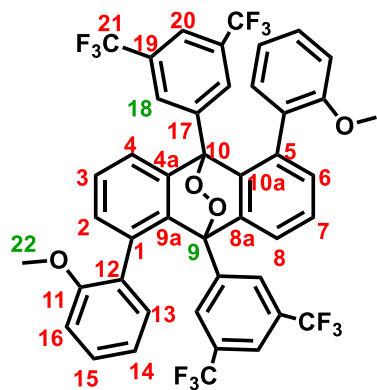
Scheme S1. Synthetic route to the peroxides



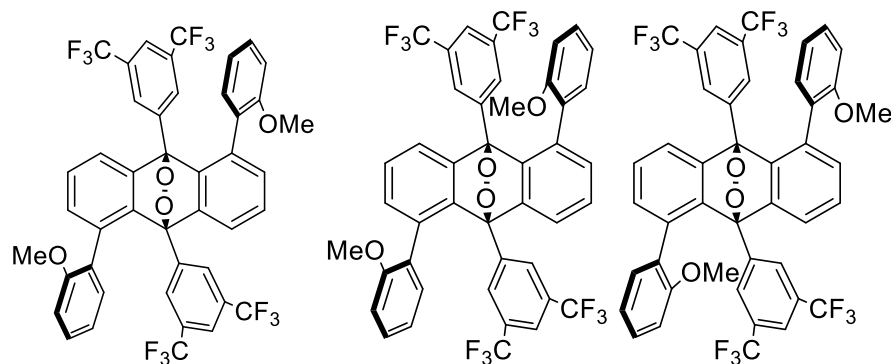
General procedure for the photochemical synthesis of Ant-C_n-O₂

Quantitative photosynthesis was achieved by exposing the anthracenes at 100% intensity to the Kessil PR160–427 nm light source. **Ant-C_n** (10^{−3} M) in chloroform (1 mL), kept at −5 °C in a screw-capped glass vial, was irradiated at 427 nm for 3 min. The reaction was monitored by the disappearance of the blue emission from the reaction mixture. Chloroform was distilled off the reaction mixture by rotavapor, kept at 35 °C and the resulting mass was washed with 2 × 0.5 mL hexane to afford a pure white solid.

S2.1 Synthesis of Ant-open-O₂



Ant-Open-O₂ was synthesized using an identical procedure to that used for the **Ant-Cn-O₂** series, with the exception that an extended irradiation time (5 min) was used for **Ant-Open** (8 mg, 9.82×10^{-6} mol). A purification procedure similar to that used for the **Ant-Cn-O₂** series afforded **Ant-Open-O₂** as a white solid (7.5 mg, 90%), which consisted of three isomers in solution:



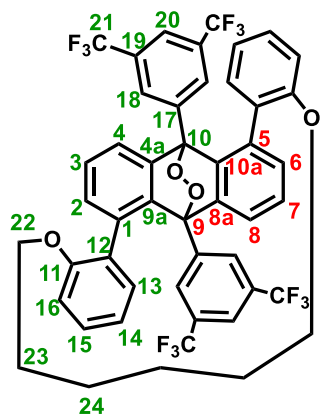
¹H NMR (400 MHz, Chloroform-*d*) δ 7.58 (s, 2H), 7.26 – 6.95 (m, 9H), 6.90 (t, $J = 7.4$ Hz, 2H), 6.81 – 6.73 (m, 2H), 6.68 (ddd, $J = 11.9, 7.5, 1.6$ Hz, 2H), 6.38 – 6.30 (m, 2H), 6.13 (d, $J = 8.3$ Hz, 2H), 3.79 (d, $J = 3.1$ Hz, 2H), 3.43 (s, 4H).

¹³C NMR (126 MHz, Chloroform-*d*) δ 154.75, 154.63, 154.60, 142.21, 141.78, 141.63, 141.17, 136.63, 135.76, 135.21, 135.18, 135.01, 134.64, 134.47, 134.16, 134.03, 133.62, 133.52, 133.26, 132.62, 132.59, 129.79, 129.46, 129.43, 129.37, 128.55, 128.11, 128.08, 127.48, 127.41, 126.67, 126.60, 123.29, 123.13, 122.98, 122.84, 122.21, 122.02, 120.87, 119.78, 110.68, 108.80, 84.61, 84.39, 84.16, 54.90, 54.06.

HRMS (ESI) m/z : $[M]^+$ Calcd for C₄₄H₂₆F₁₂O₄ 846.1639; found 846.1636.

UV-vis (H₂C₂Cl₄): λ_{\max} (ϵ) = 292 nm (7807 M⁻¹ cm⁻¹).

S2.2 Synthesis of Ant-C6-O₂



Prepared according to the general procedure, using **Ant-C6** (6 mg, 7.14 × 10⁻⁶ mol). Obtained a white solid (5.7 mg, 93%).

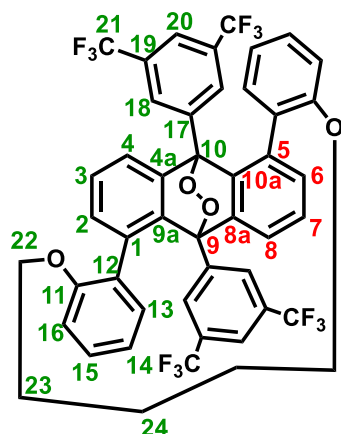
¹H NMR (500 MHz, Chloroform-*d*) δ 8.09 (s, 4H, H-C(18)), 7.60 (s, 2H, H-C(20)), 7.43 (dd, J = 7.9, 1.3 Hz, 2H, H-C(4)), 7.30 (t, J = 7.8 Hz, 2H, H-C(3)), 7.03 (ddd, J = 8.2, 7.4, 1.7 Hz, 2H, H-C(15)), 6.89 (dd, J = 7.7, 1.3 Hz, 2H, H-C(2)), 6.66 (d, J = 8.2 Hz, 2H, H-C(16)), 6.46 (td, J = 7.4, 1.0 Hz, 2H, H-C(14)), 6.38 (dd, J = 7.4, 1.7 Hz, 2H, H-C(13)), 3.97 (ddd, J = 8.9, 5.2, 3.8 Hz, 2H, H-C(22), diastereotopic), 3.64 (td, J = 9.1, 2.9 Hz, 2H, H-C(22), diastereotopic), 1.48 (m, 2H, H-C(23), diastereotopic), 1.07 (m, 2H, H-C(23), diastereotopic), 0.85 (m, 3H, H-C(24), diastereotopic), 0.77 – 0.67 (m, 2H, H-C(24), diastereotopic).

¹³C NMR (125 MHz, Chloroform-*d*) δ 154.8 (C11), 139.0(C9a), 135.7(C4a), 135.5(C1), 135.2(C17), 133.4(C2), 130.3(C12), 130.0 (C19), 129.3(C13), 128.4(C15), 128.3(C18), 127.2(C3), 126.4-119.9 (q, J = 275 Hz, C21), 122.7(C20), 122.6(C4), 120.2(C14), 111.3 (C16), 83.8(C10), 66.8(C22), 29.4(C23), 25.7(C24).

HRMS (ESI) m/z : [M]⁺ Calcd for C₄₈H₃₂F₁₂O₄ 900.2109; found 900.2166.

UV-vis (H₂C₂Cl₄): λ_{\max} (ϵ) = 271 (3267), 292 nm (2955 M⁻¹ cm⁻¹).

S2.3 Synthesis of Ant-C5-O₂



Prepared according to the general procedure, using **Ant-C5** (5 mg, 5.85×10^{-6} mol). Obtained white solid (5.0 mg, 96%).

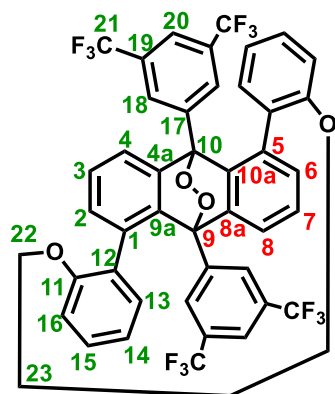
¹H NMR (400 MHz, Chloroform-*d*) δ 8.04 (s, 4H, H-C(18)), 7.61 (s, 2H, H-C(20)), 7.50 (dd, $J = 7.9, 1.3$ Hz, 2H, H-C(4)), 7.33 (t, $J = 7.8$ Hz, 2H, H-C(3)), 7.08 (td, $J = 7.8, 1.8$ Hz, 2H, H-C(15)), 6.93 (dd, $J = 7.6, 1.3$ Hz, 2H, H-C(2)), 6.76 (d, $J = 8.2$ Hz, 2H, H-C(16)), 6.53 (td, $J = 7.5, 1.1$ Hz, 2H, H-C(14)), 6.40 (dd, $J = 7.5, 1.8$ Hz, 2H), 3.82-3.67 (m, 2H, H-C(22), diastereotopic), 3.58 (td, $J = 8.3, 3.4$ Hz, 2H, H-C(22), diastereotopic), 1.33 (m, 2H, H-C(23), diastereotopic), 1.17 (d, $J = 8.5$ Hz, 2H, H-C(23), diastereotopic), 0.58 (p, $J = 8.1$ Hz, 2H, H-C(24)).

¹³C NMR (100 MHz, Chloroform-*d*) δ 155.5 (C11), 141.0 (C9a), 135.3 (C4a), 134.6 (C17), 132.6 (C2), 132.0 (C12), 130.3-130.0 (C19), 128.6 (C13), 128.6 (C15), 128.4 (C18), 126.4-119.9 (q, $J = 275$ Hz, C21), 122.7 (C4), 122.6 (C20), 121.5 (C14), 114.7 (C16), 83.8 (C9), 69.6 (C22), 30.3 (C23), 22.4 (C24).

HRMS (ESI) m/z : $[M]^+$ Calcd for C₄₇H₃₀F₁₂O₄ 886.1952; found 886.1964.

UV-vis (H₂C₂Cl₄): λ_{\max} (ϵ) = 272 nm (3276 M⁻¹ cm⁻¹).

S2.4 Synthesis of Ant-C4-O₂



Prepared according to the general procedure, using **Ant-C4** (4 mg, 4.76×10^{-6} mol). Obtained a white solid (4.0 mg, 96%).

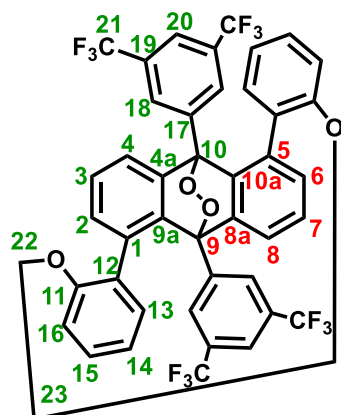
¹H NMR (500 MHz, Chloroform-*d*) δ 8.02 (s, 4H, H-C(18)), 7.63 (s, 2H, H-C(20)), 7.61 (dd, $J = 7.7, 1.2$ Hz, 4H, H-C(4)), 7.35 (t, $J = 7.7$ Hz, 2H, H-C(3)), 7.09 (td, $J = 7.9, 1.7$ Hz, 2H, H-C(15)), 6.90 (dd, $J = 7.5, 1.2$ Hz, 2H, H-C(2)), 6.59-6.59 (m, 4H, H-C(14) and H-C(16)), 6.46 (dd, $J = 7.4, 1.7$ Hz, 2H, H-C(13)), 3.94 (d, $J = 8.3$ Hz, 2H, H-C(22), diastereotopic), 3.25 (dd, $J = 12.1, 8.5$ Hz, 2H, H-C(22), diastereotopic), 1.06 (m, 2H, H-C(23), diastereotopic), 0.78 (m, 2H, H-C(23), diastereotopic).

¹³C NMR (125 MHz, Chloroform-*d*) δ 155.1 (C11), 144.6 (C9a), 135.4 (C17), 133.9 (C1), 133.2 (C4a), 131.9 (C2), 130.9 (C12), 130.6-129.8 (q, $J = 33.8$ Hz, C19), 128.9 (C15), 128.4 (C18), 127.2 (C3), 127.1 (C13), 126.4-119.9 (q, $J = 275$ Hz, C21), 122.5 (C20), 121.9 (C4), 120.7 (C16), 110.6 (C14), 83.6 (C10), 66.7 (C22), 25.7 (C23).

HRMS (ESI) m/z : $[M]^+$ Calcd for C₄₆H₂₈F₁₂O₄ 872.1796; found 872.1753.

UV-vis (H₂C₂Cl₄): λ_{\max} (ϵ) = 285 nm (4695 M⁻¹ cm⁻¹).

S2.5 Synthesis of Ant-C3-O₂



Prepared according to the general procedure, using **Ant-C3** (4 mg, 4.84×10^{-6} mol). Obtained a white solid (4.0 mg, 96%).

¹H NMR (500 MHz, Chloroform-*d*) δ 8.00 (s, 4H, H-C(18)), 7.72 (dd, $J = 7.7, 1.2$ Hz, 2H, H-C(4)), 7.66 (s, 2H, H-C(20)), 7.42 (t, $J = 7.7$ Hz, 2H, H-C(3)), 7.10 (td, $J = 7.8, 1.7$ Hz, 2H, H-C(15)), 7.01 (dd, $J = 7.6, 1.2$ Hz, 2H, H-C(2)), 6.77 (dd, $J = 8.1, 1.3$ Hz, 2H, H-C(16)), 6.69 (td, $J = 7.5, 1.2$ Hz, 2H, H-C(14)), 6.48 (dd, $J = 7.4, 1.7$ Hz, 2H, H-C(13)), 3.10 (dt, $J = 9.3, 5.7$ Hz, 2H, H-C(22)), 2.73 (dt, $J = 9.2, 5.9$ Hz, 2H, H-C(22)), 1.21 (p, $J = 5.8$ Hz, 2H, H-C(23)).

¹³C NMR (125 MHz, Chloroform-*d*) δ 156.7 (C11), 146.2 (C9a), 135.5 (C4a), 134.0 (C12), 133.21 (C1), 133.18 (C17), 132.0 (C2), 130.8-130.0 (q, $J = 37.5$ Hz, C19), 129.5 (C15), 128.34-128.31 (C18), 127.4 (C3), 127.2 (C13), 126.3-119.8 (q, $J = 275$ Hz, C21), 123.6 (C14), 122.4 (C20), 122.0 (C4), 120.2 (C16), 83.5 (C10), 68.4 (C22), 31.3 (C23).

HRMS (ESI) m/z : $[M]^+$ Calcd for C₄₅H₂₆F₁₂O₄ 858.1639; found 858.1639.

UV-vis (H₂C₂Cl₄): λ_{\max} (ϵ) = 286 (4745 M⁻¹ cm⁻¹).

S3 Characterization

S3.1 Characterization of Ant-Open-O₂

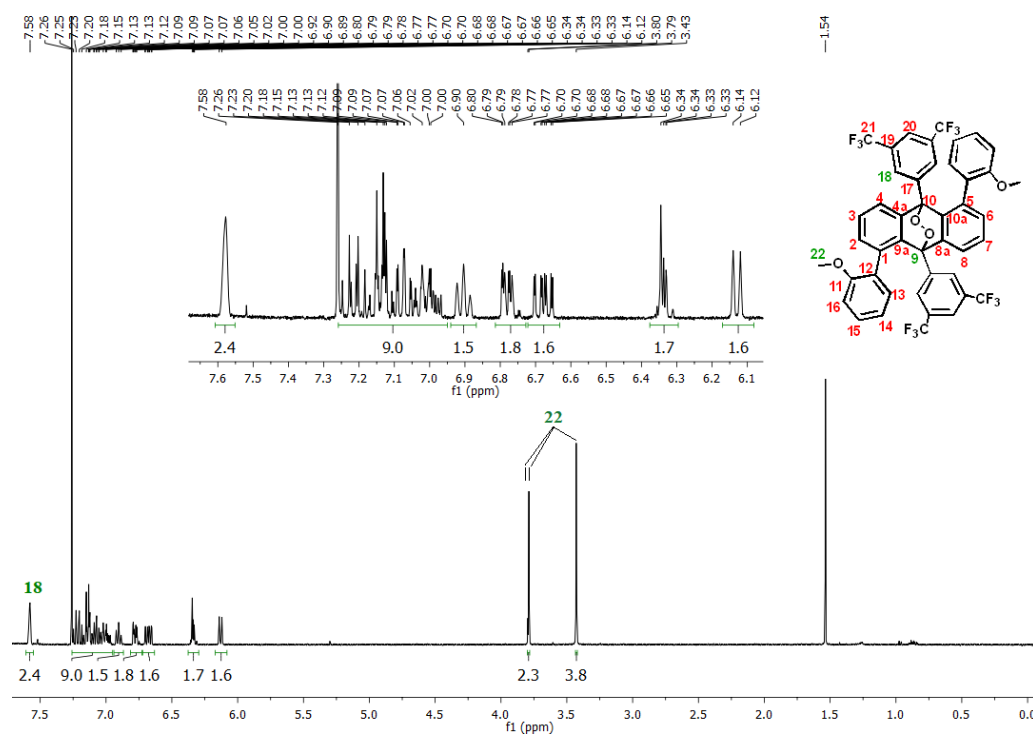


Figure S1. ¹H NMR (400 MHz) of Ant-Open-O₂ in CDCl₃, measured at 298 K. (Inset: expansion in the aromatic region).

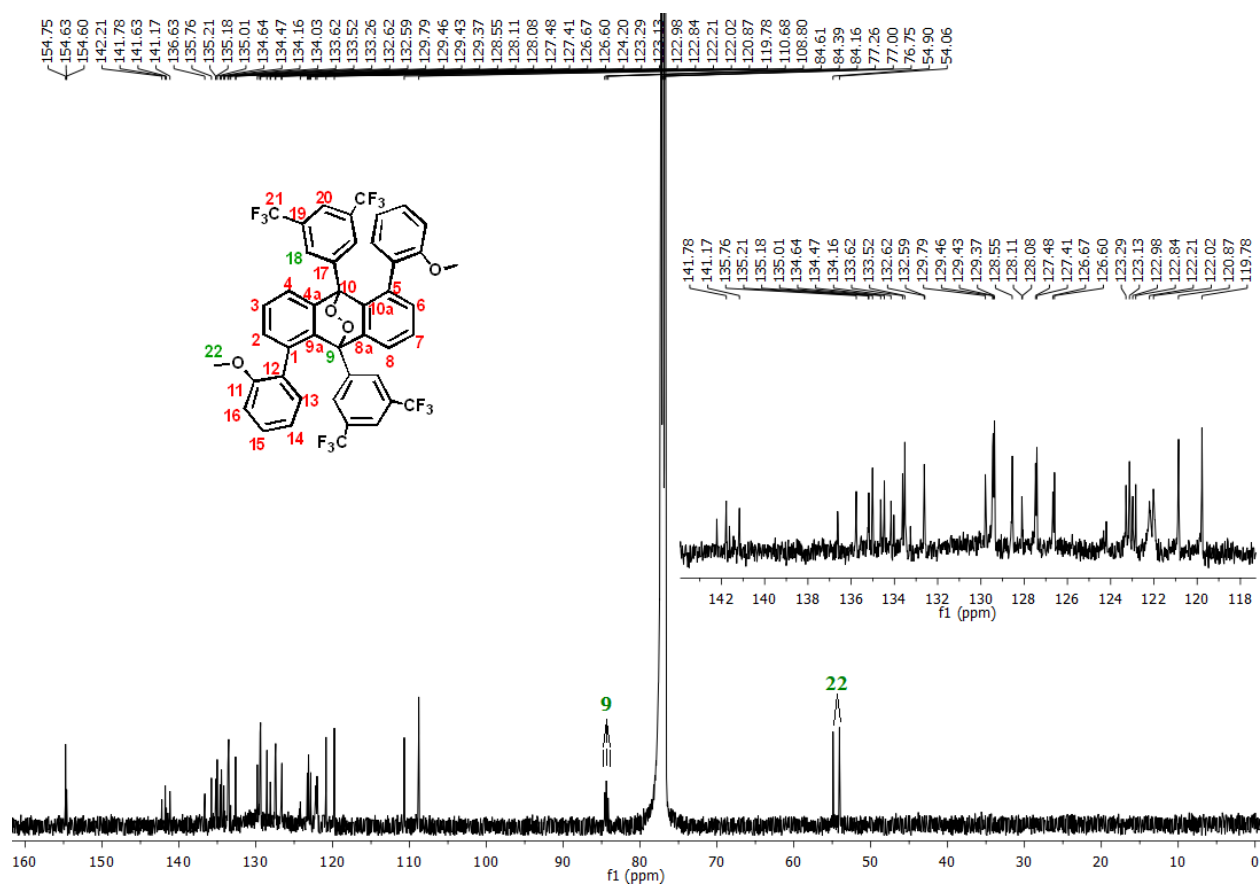


Figure S2. ^{13}C NMR (125 MHz) of Ant-Open-O₂ in CDCl_3 , measured at 298 K.

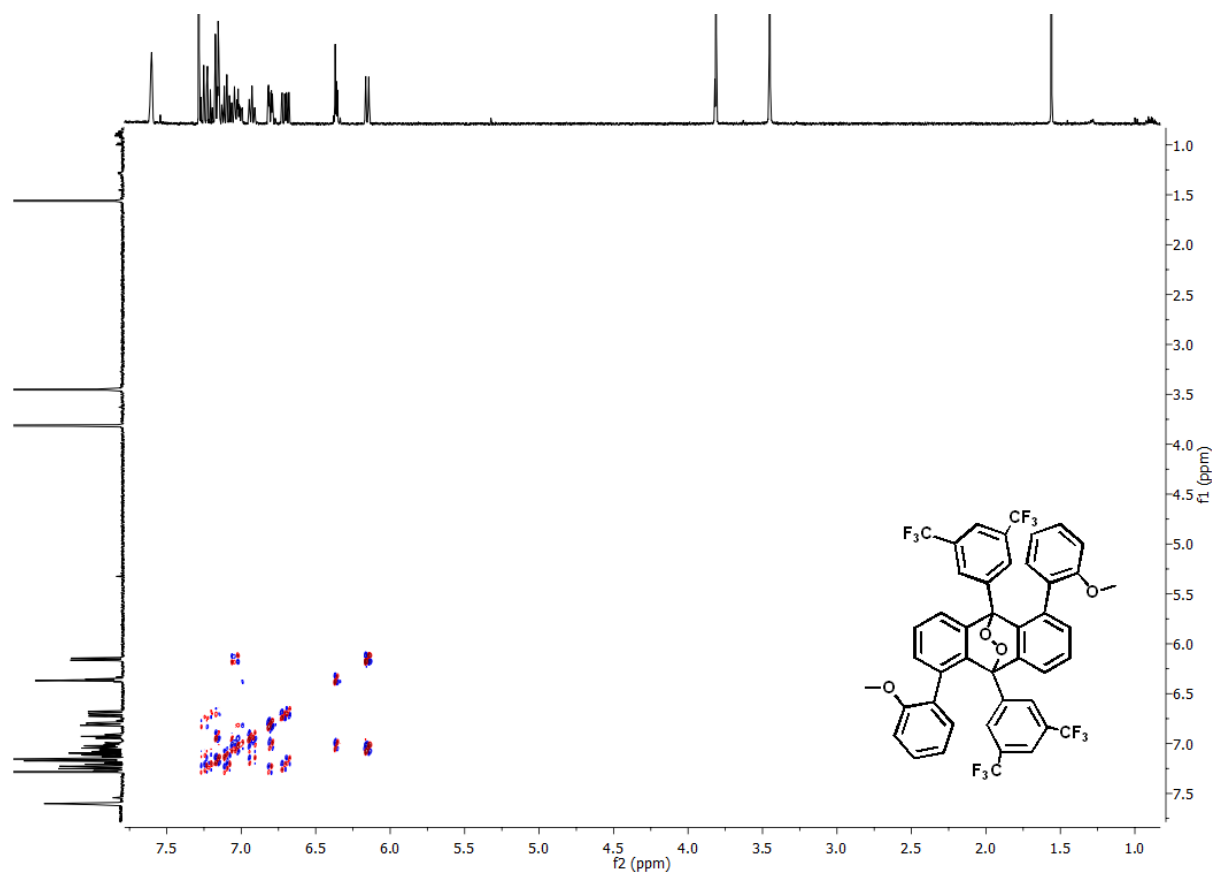


Figure S3. COSY NMR (400 MHz) of **Ant-Open-O₂** in CDCl₃, measured at 298 K.

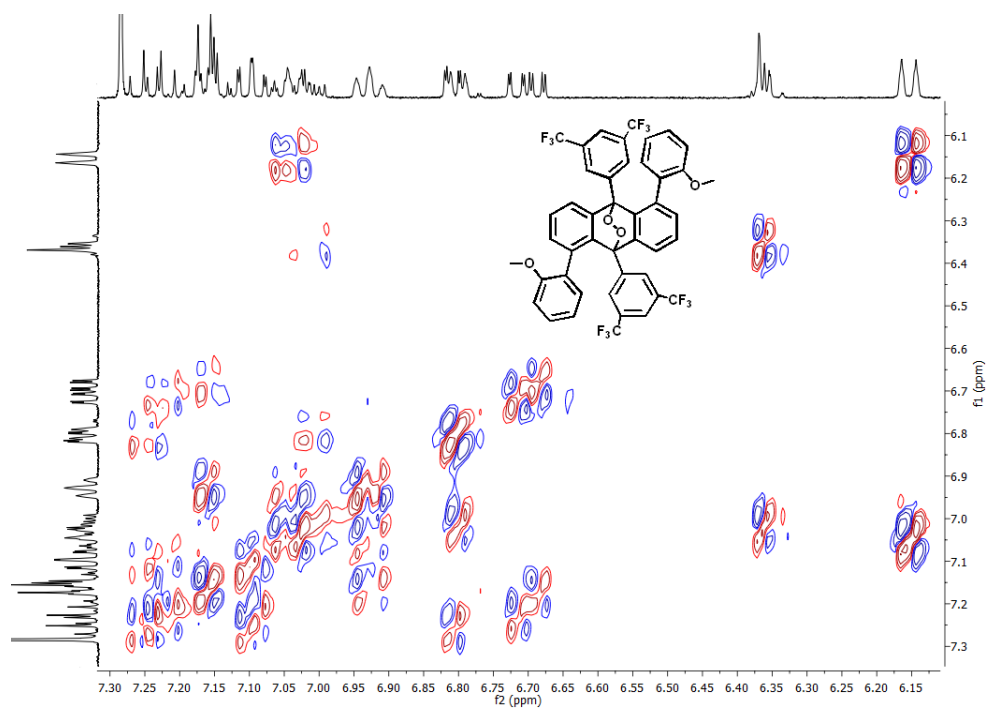


Figure S4. COSY NMR (400 MHz) of **Ant-Open-O₂** in CDCl₃, measured at 298 K. The plot is an expanded view of the aromatic region.

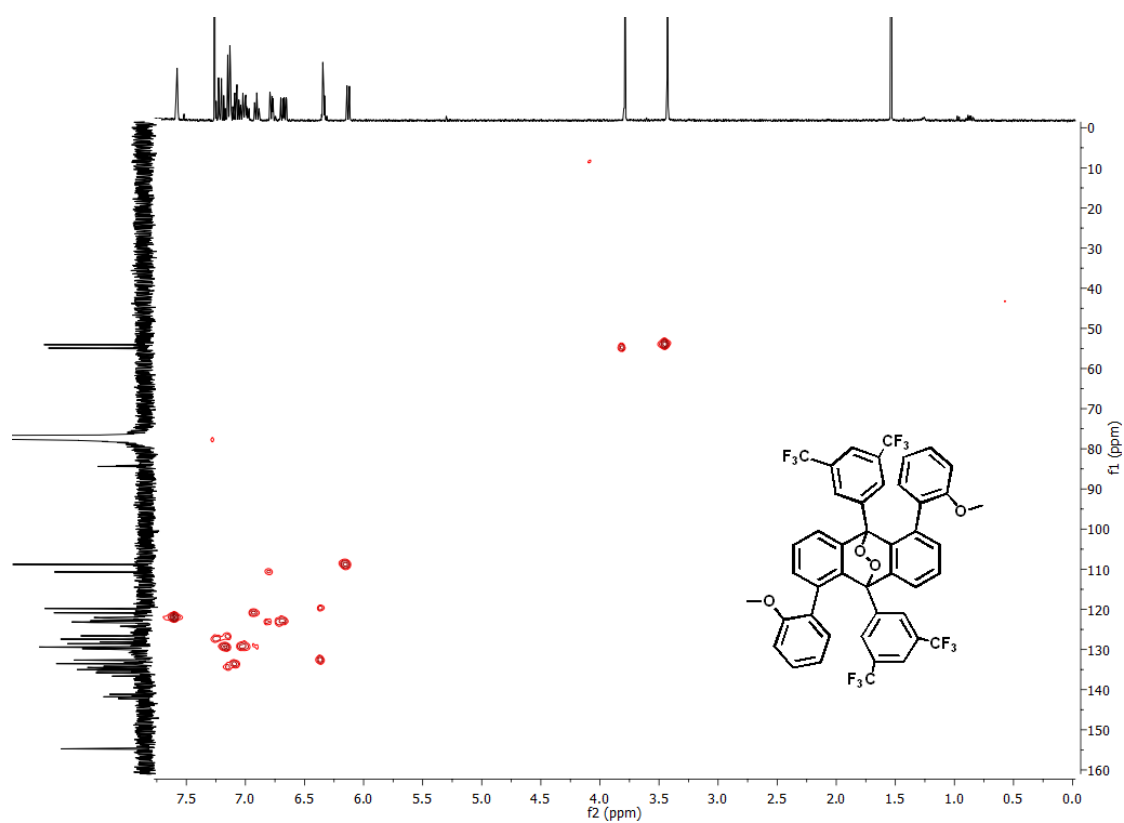


Figure S5. HSQC NMR (400 MHz) of **Ant-Open-O₂** in CDCl₃, measured at 298 K.

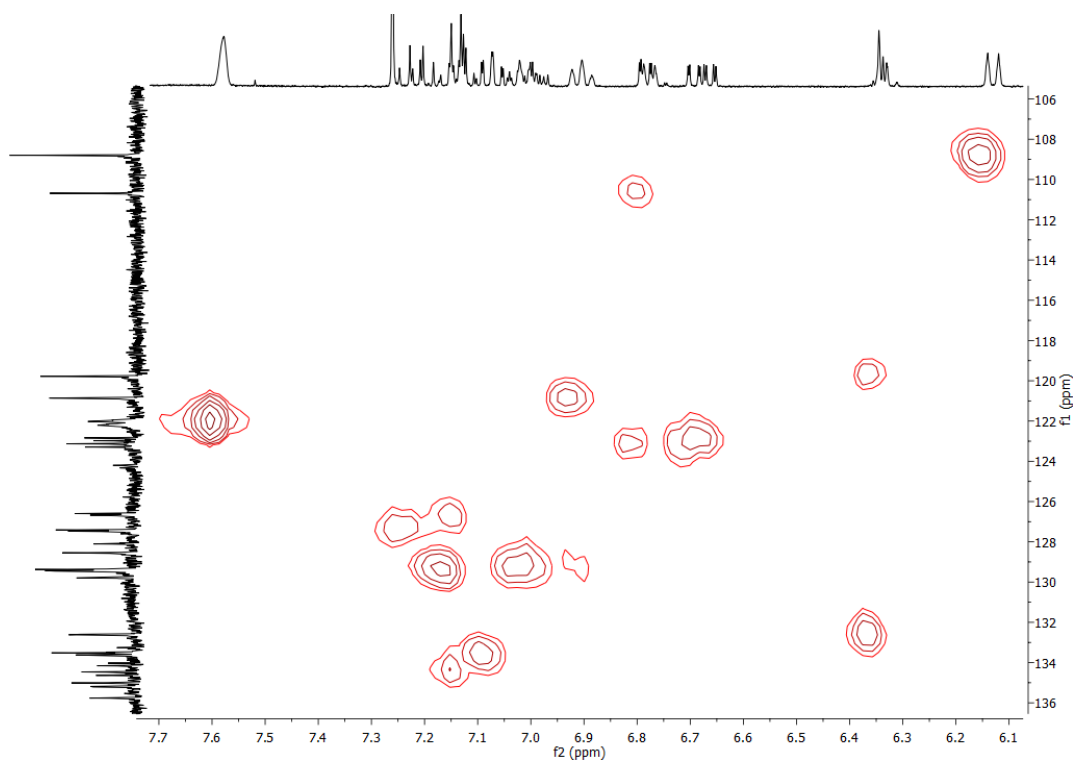


Figure S6. HSQC NMR (400 MHz) of **Ant-Open-O₂** in CDCl₃, measured at 298 K. The plot is an expanded view of the aromatic region.

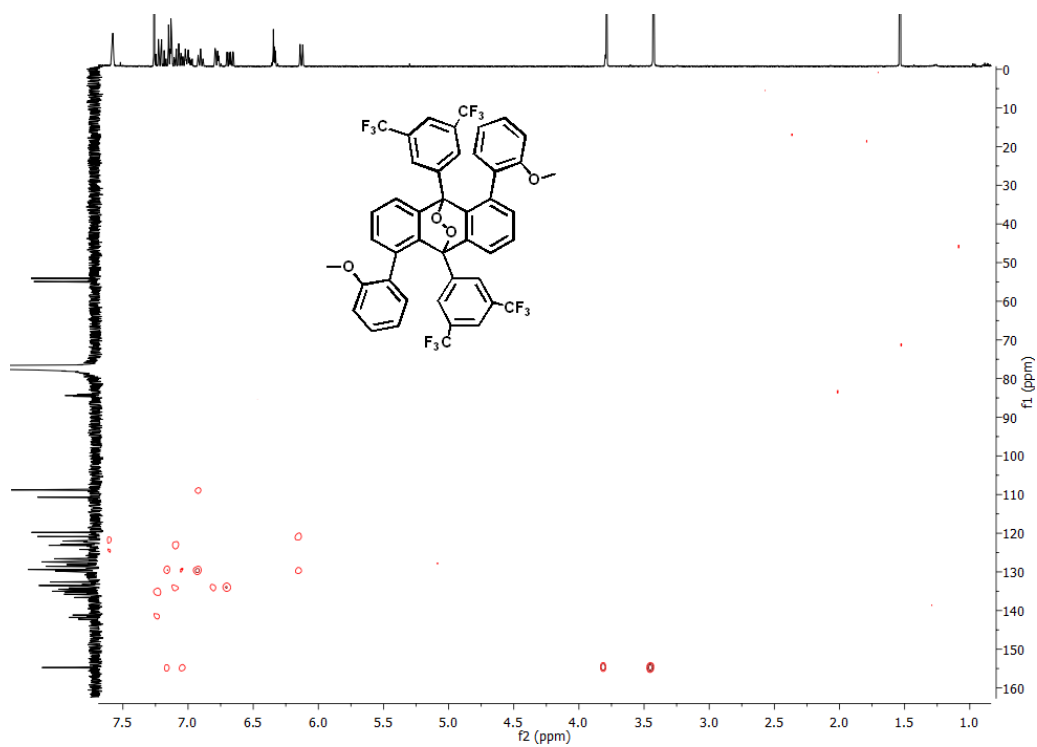


Figure S7. HMBC NMR (400 MHz) of **Ant-Open-O₂** in CDCl₃, measured at 298 K.

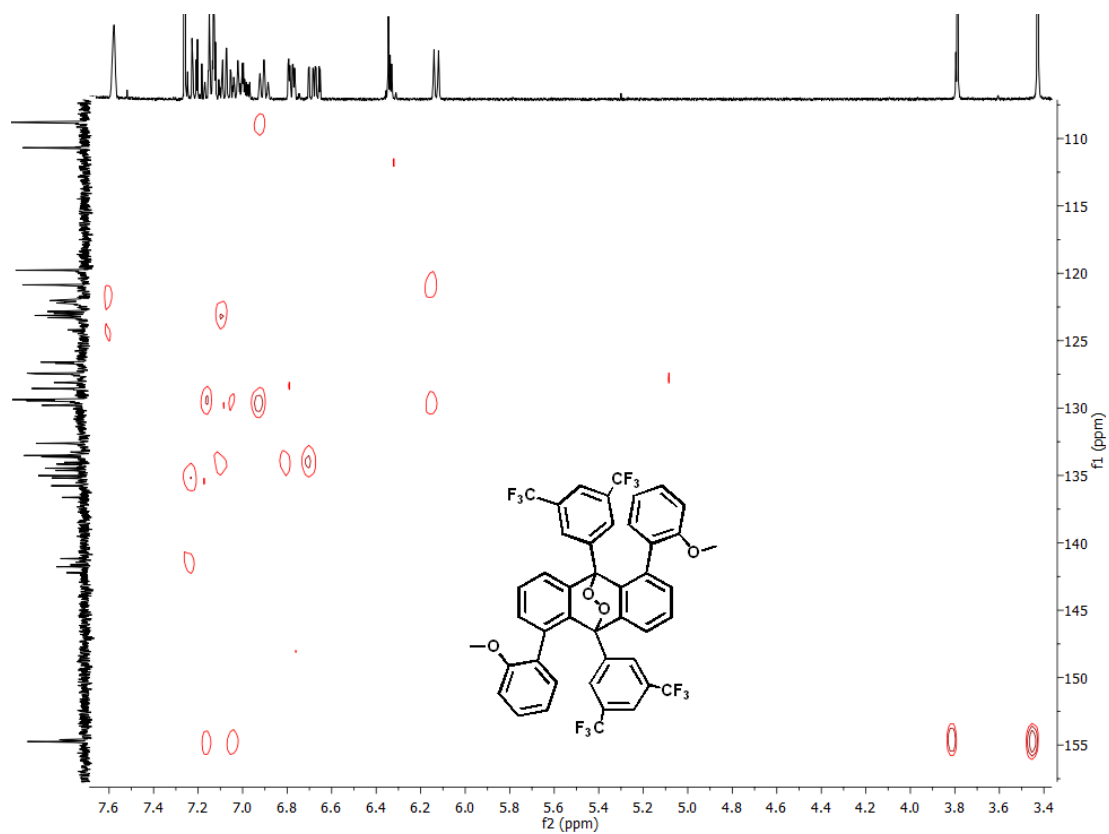


Figure S8. HMBC NMR (400 MHz) of **Ant-Open-O₂** in CDCl₃, measured at 298 K.

S3.2 Characterization of Ant-C6O₂

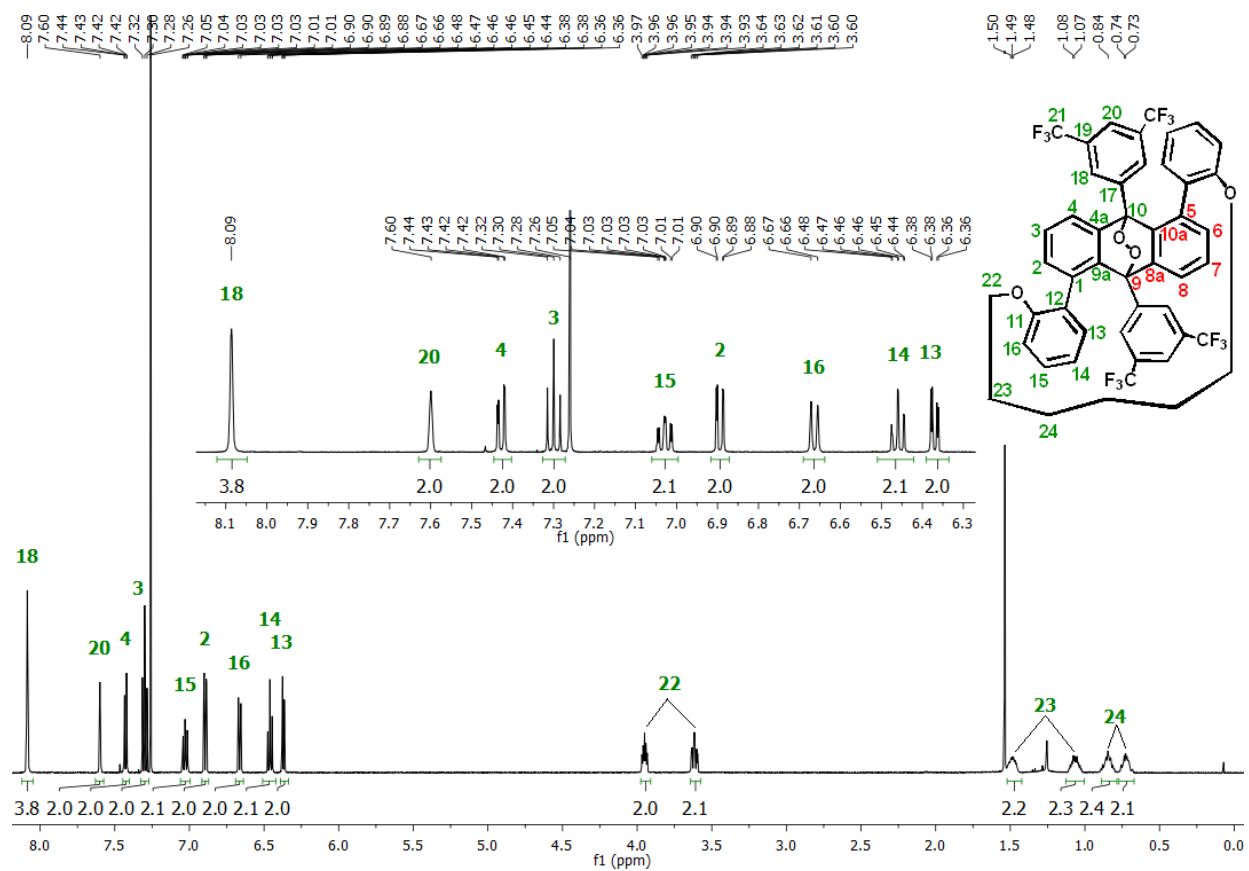


Figure S9. ¹H NMR (400 MHz) of Ant-C6-O₂ in CDCl₃, measured at 298 K.

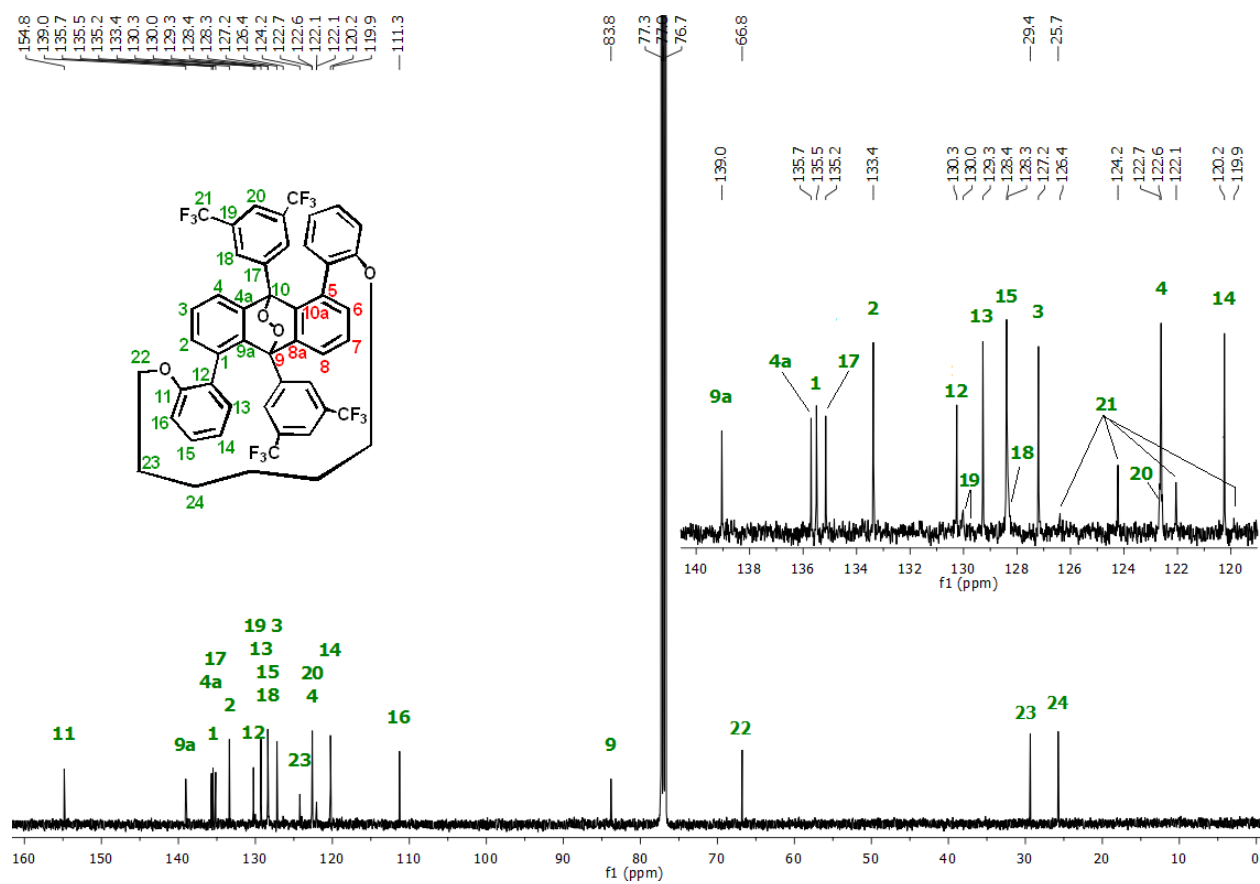


Figure S10. ^{13}C NMR (125 MHz) of Ant-C6-O₂ in CDCl_3 , measured at 298 K.

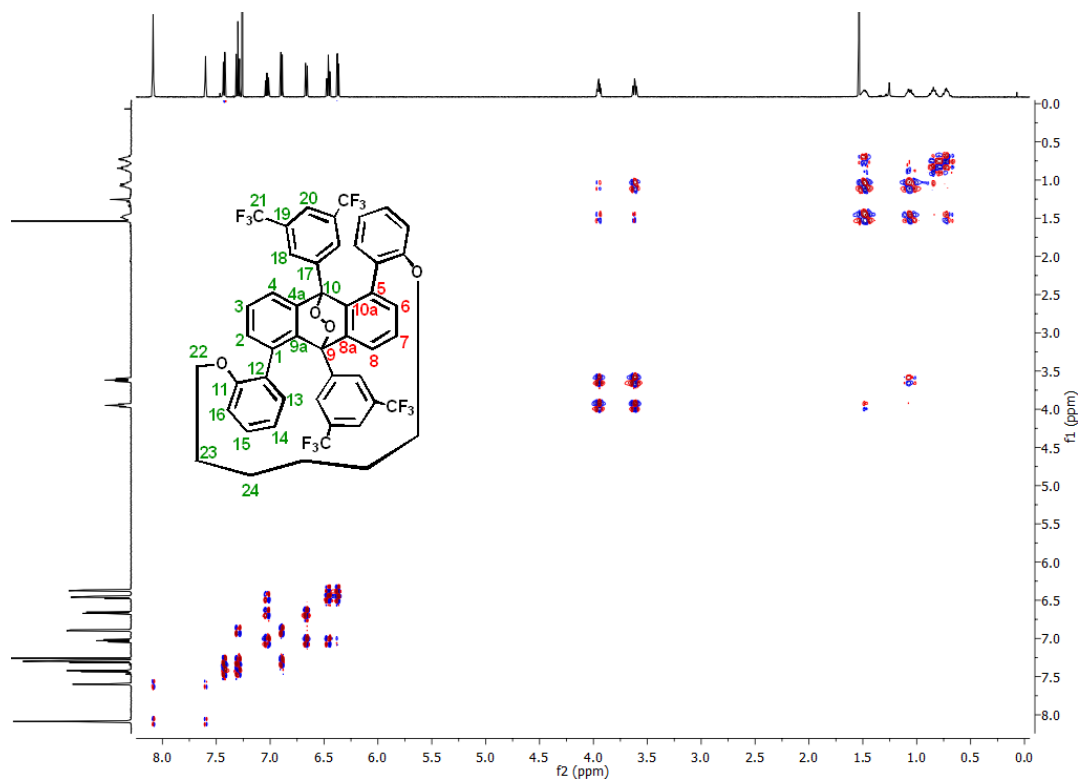


Figure S11. COSY NMR (500 MHz) of **Ant-C6-O₂** in CDCl₃, measured at 298 K.

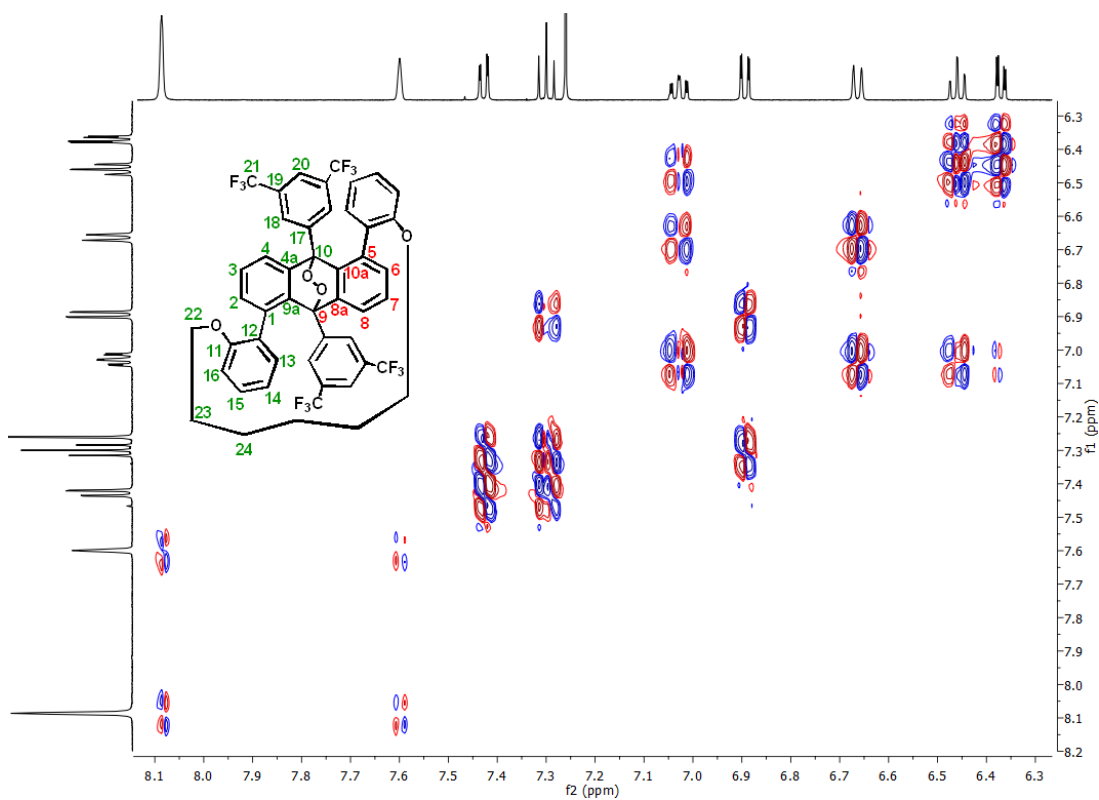


Figure S12. ¹H NMR (500 MHz) of **Ant-C6-O₂** in CDCl₃, measured at 298 K. The plot is an expanded view of the aromatic region.

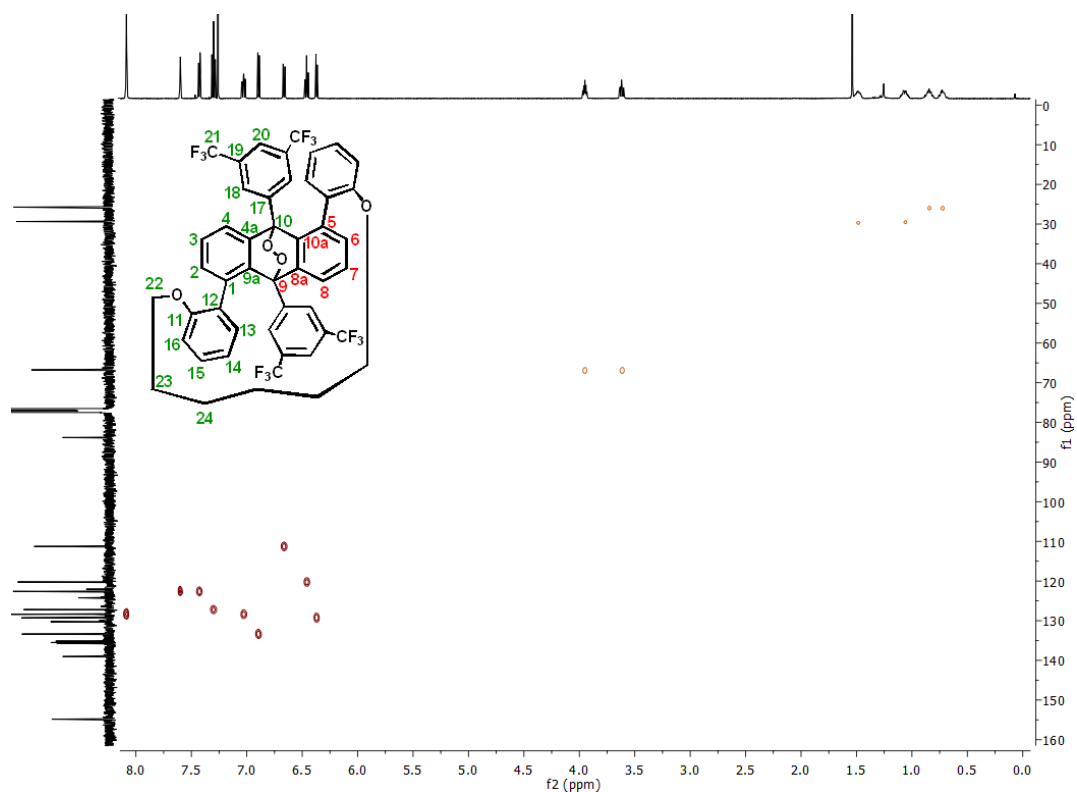


Figure S13. HSQC NMR (500 MHz) of **Ant-C6-O₂** in CDCl₃, measured at 298 K.

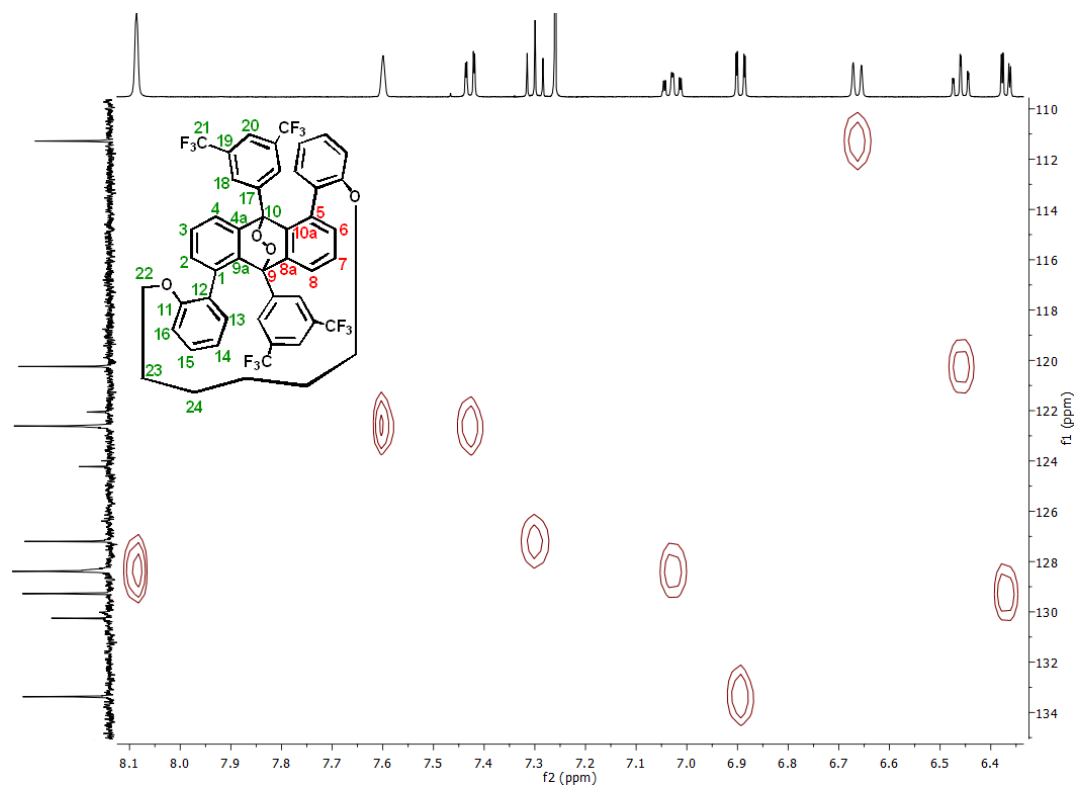


Figure S14. HSQC NMR (500 MHz) of **Ant-C6-O₂** in CDCl₃, measured at 298 K. The plot is an expanded view of the aromatic region.

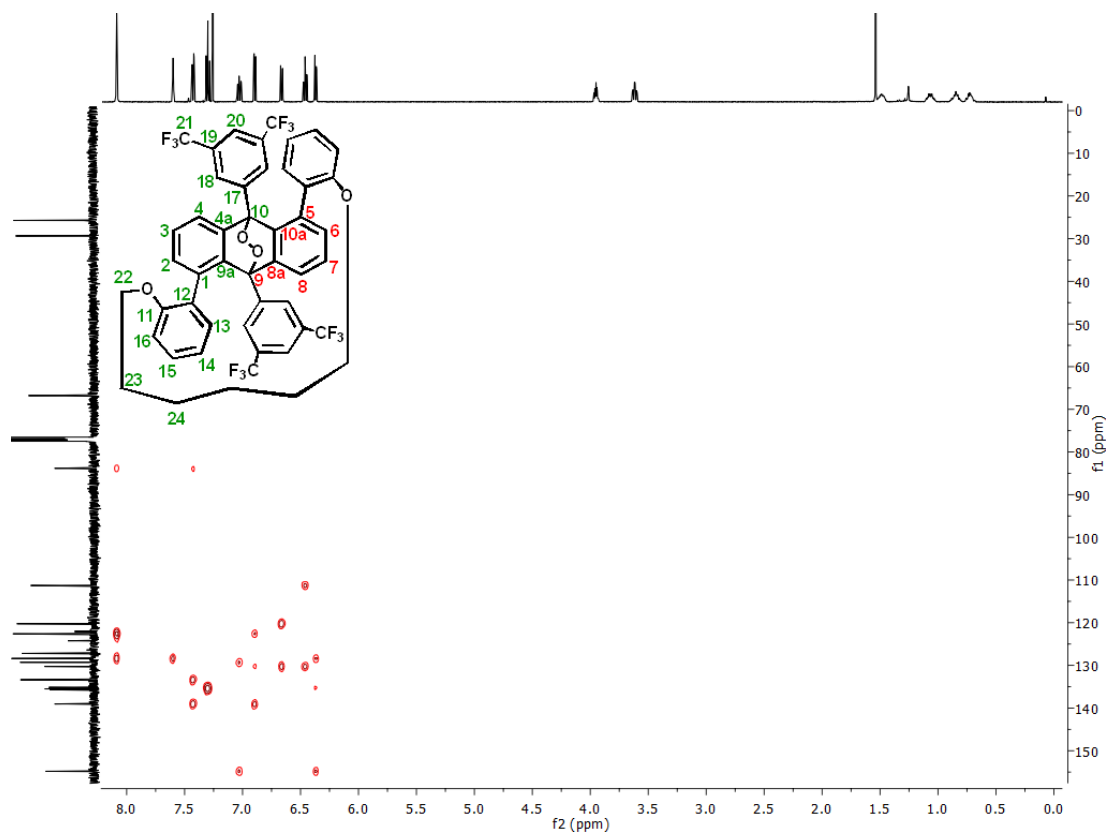


Figure S15. HMBC NMR (500 MHz) of **Ant-C6-O₂** in CDCl₃, measured at 298 K.

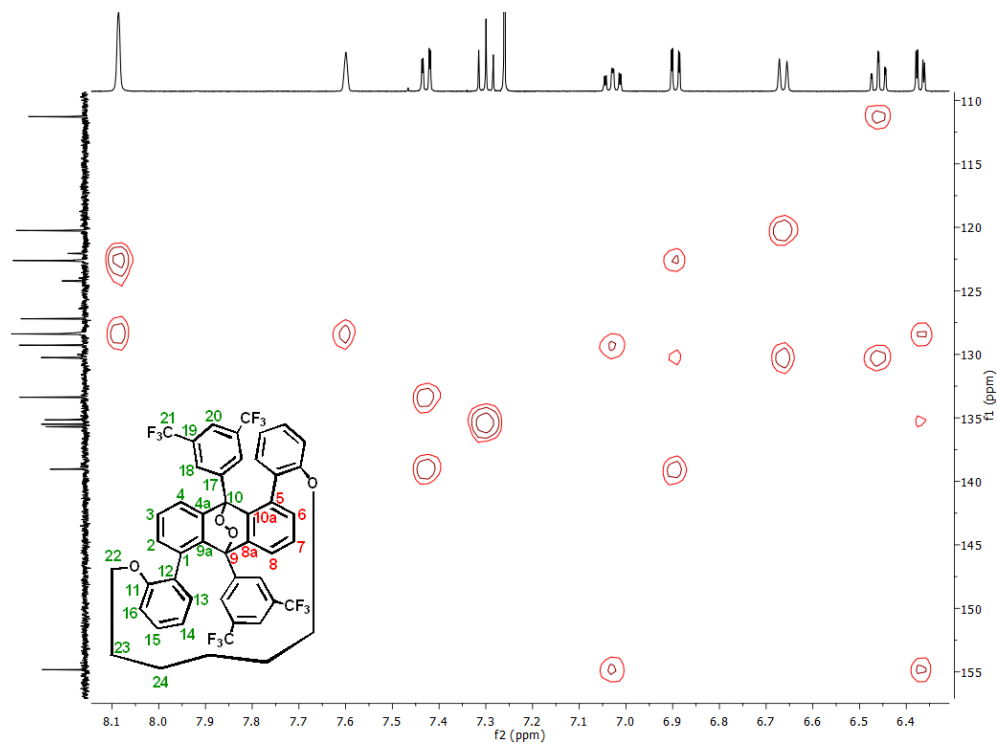


Figure S16. HMBC NMR (500 MHz) of **Ant-C6-O₂** in CDCl₃, measured at 298 K.

S3.3 Characterization of Ant-C5-O₂

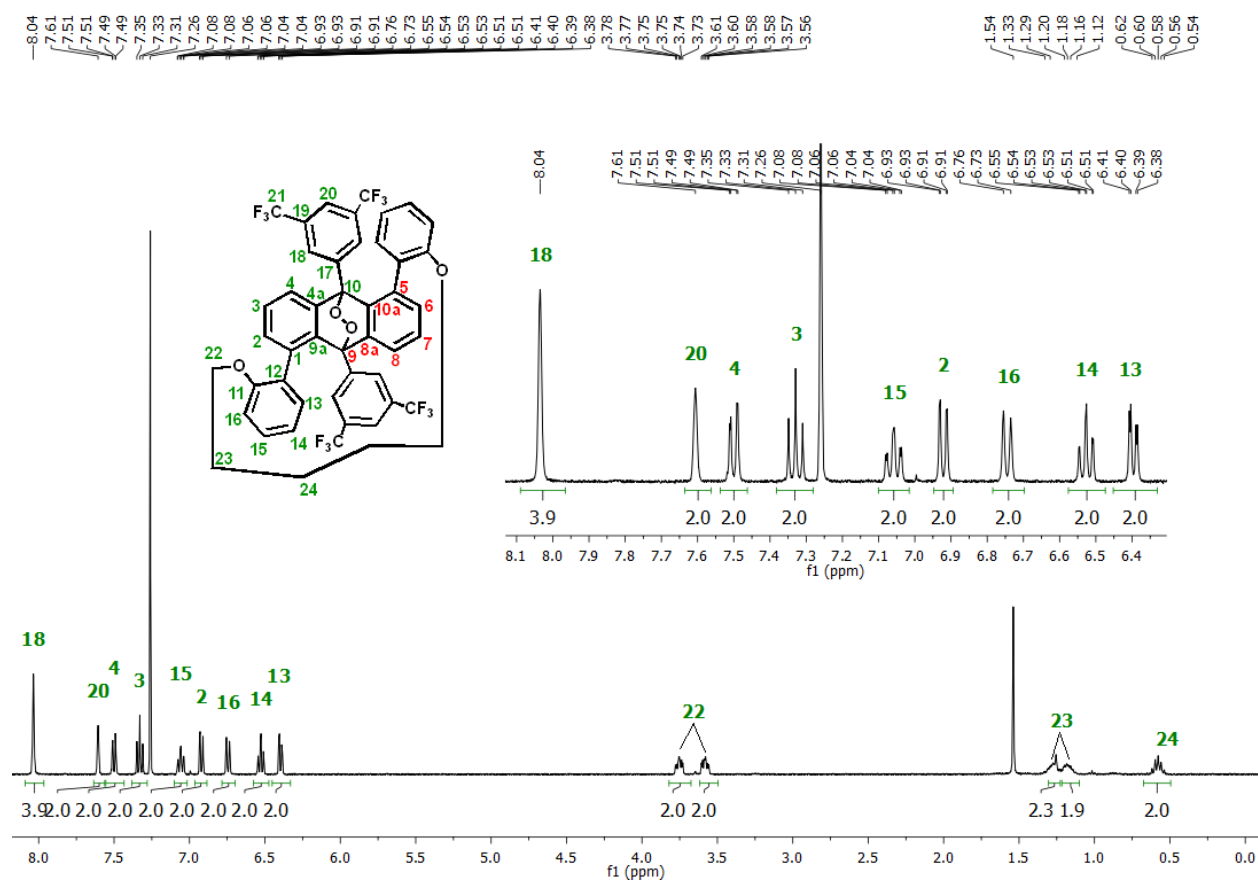


Figure S17. ¹H NMR (400 MHz) of Ant-C5-O₂ in CDCl₃, measured at 298 K.

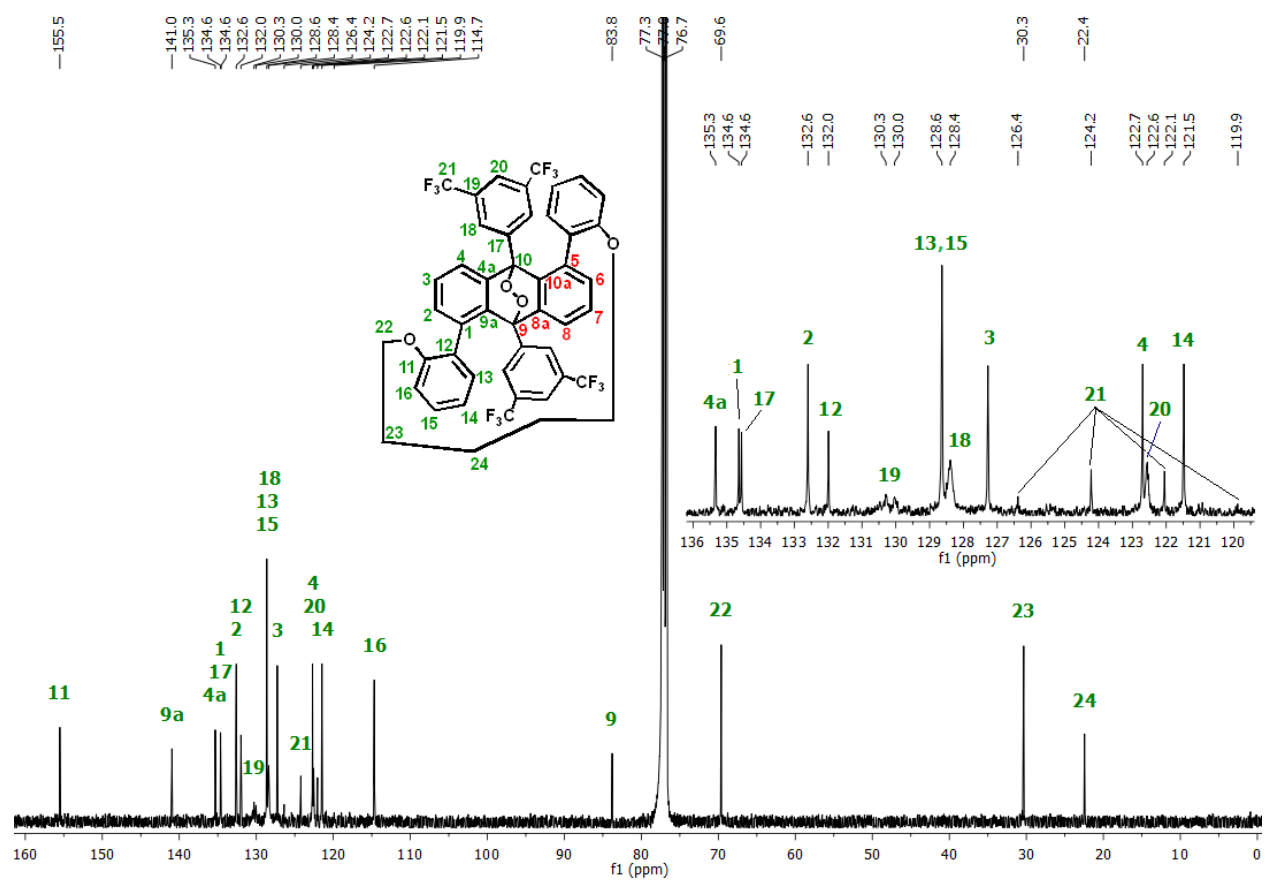


Figure S18. ^{13}C NMR (100 MHz) of **Ant-C5-O₂** in CDCl_3 , measured at 298 K.

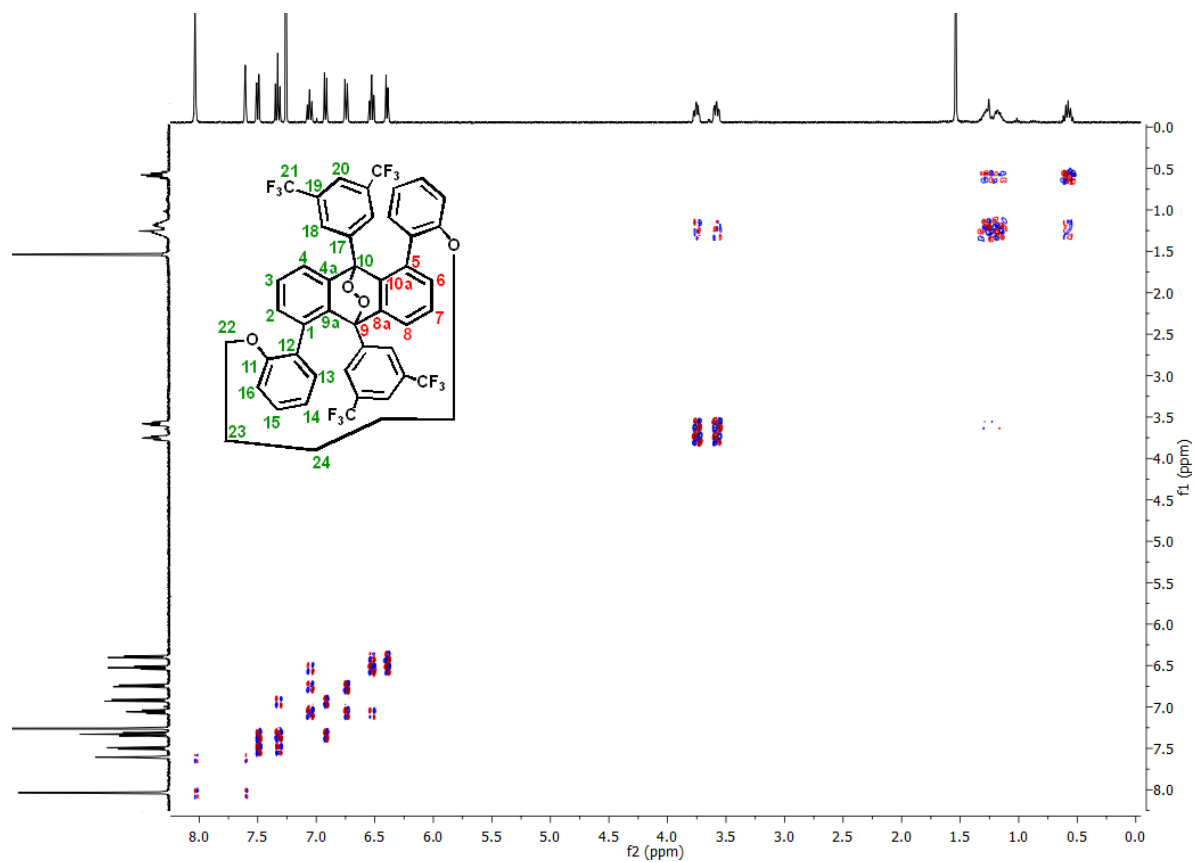


Figure S19. COSY NMR (400 MHz) of **Ant-C5-O₂** in CDCl₃, measured at 298 K.

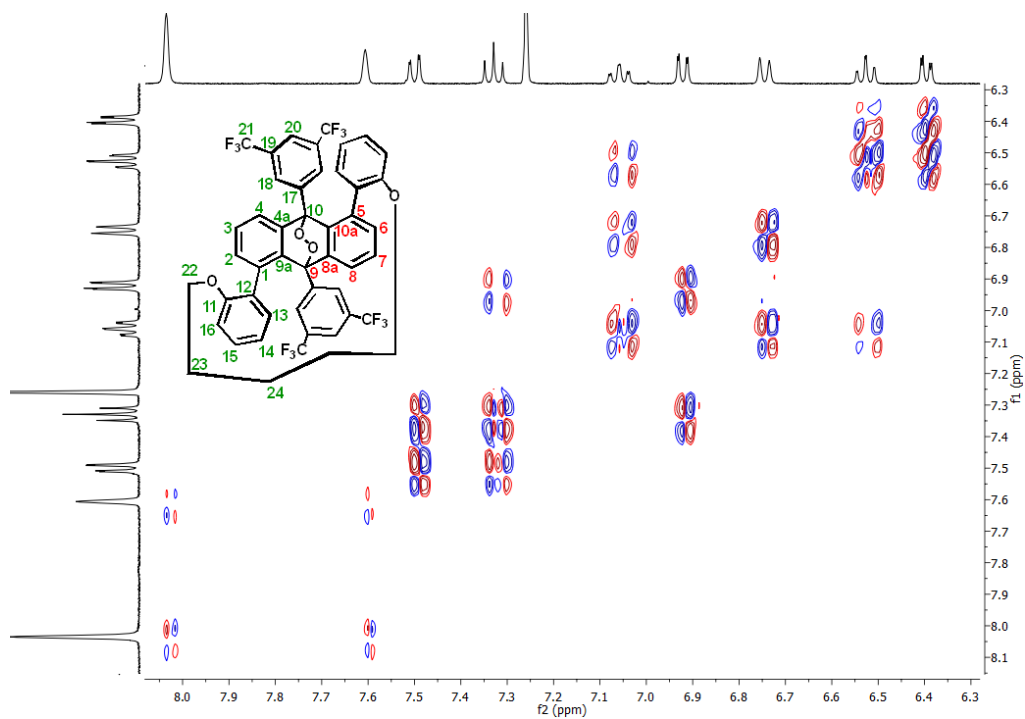


Figure S20. COSY NMR (400 MHz) of **Ant-C5-O₂** in CDCl₃, measured at 298 K. The plot is an expanded view of the aromatic region.

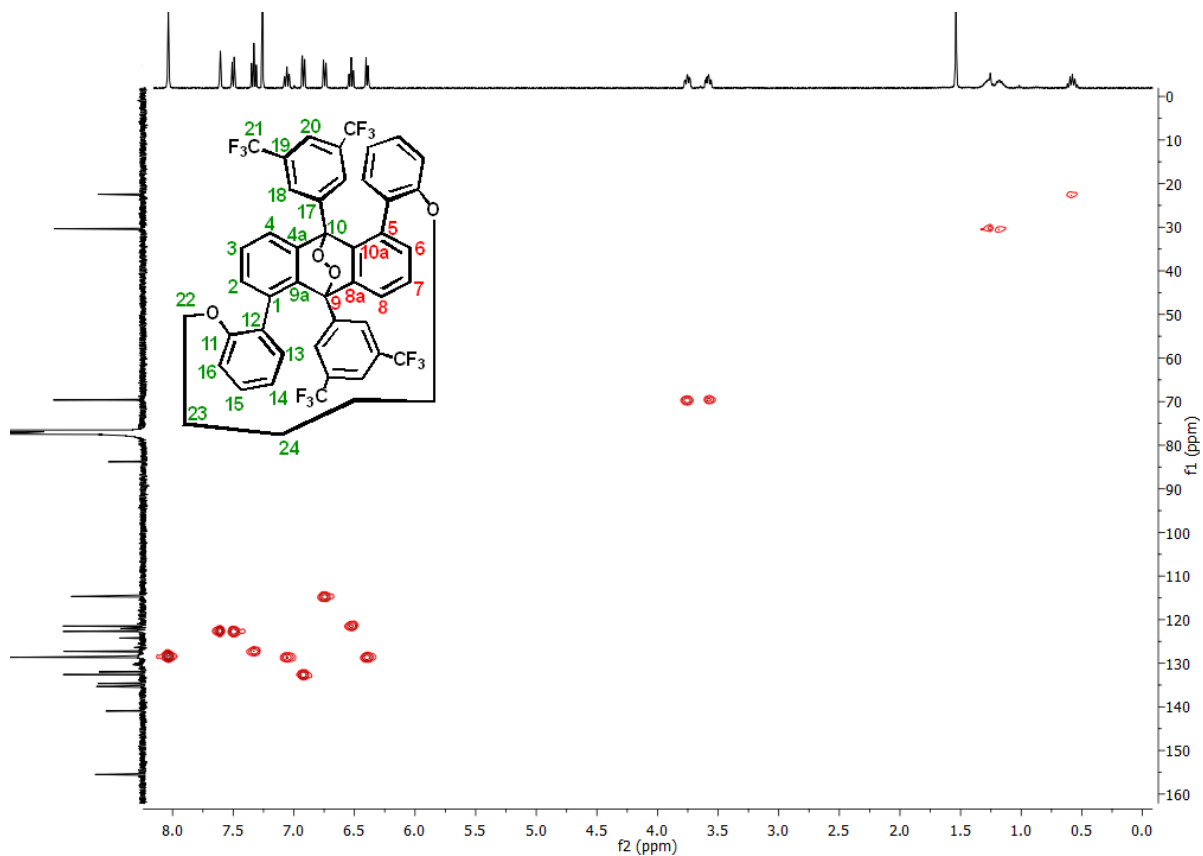


Figure S21. HSQC NMR (400 MHz) of **Ant-C5-O₂** in CDCl₃, measured at 298 K.

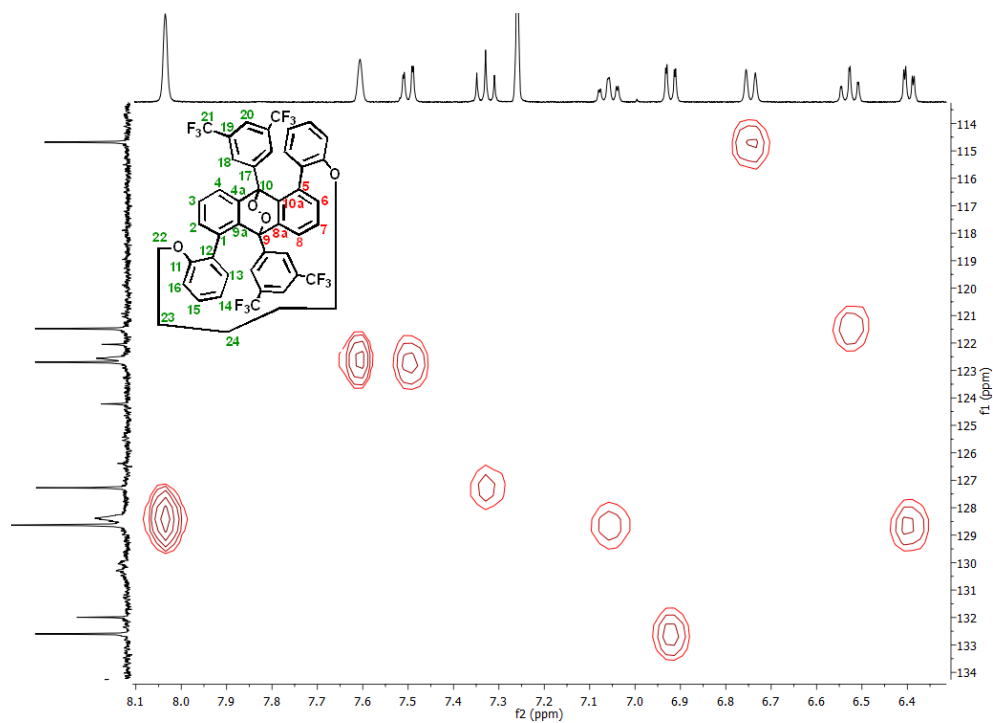


Figure S22. HSQC NMR (400 MHz) of **Ant-C5-O₂** in CDCl₃, measured at 298 K. The plot is an expanded view of the aromatic region.

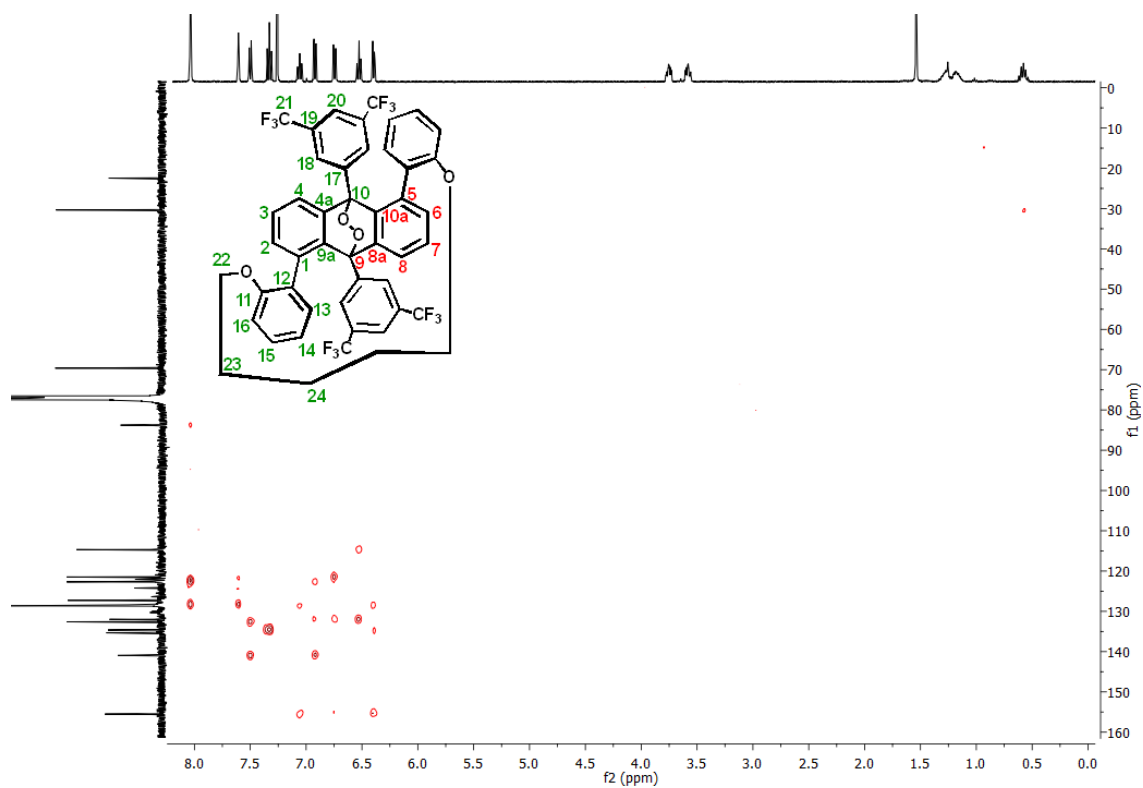


Figure S23. HMBC NMR (400 MHz) of **Ant-C5-O₂** in CDCl₃, measured at 298 K.

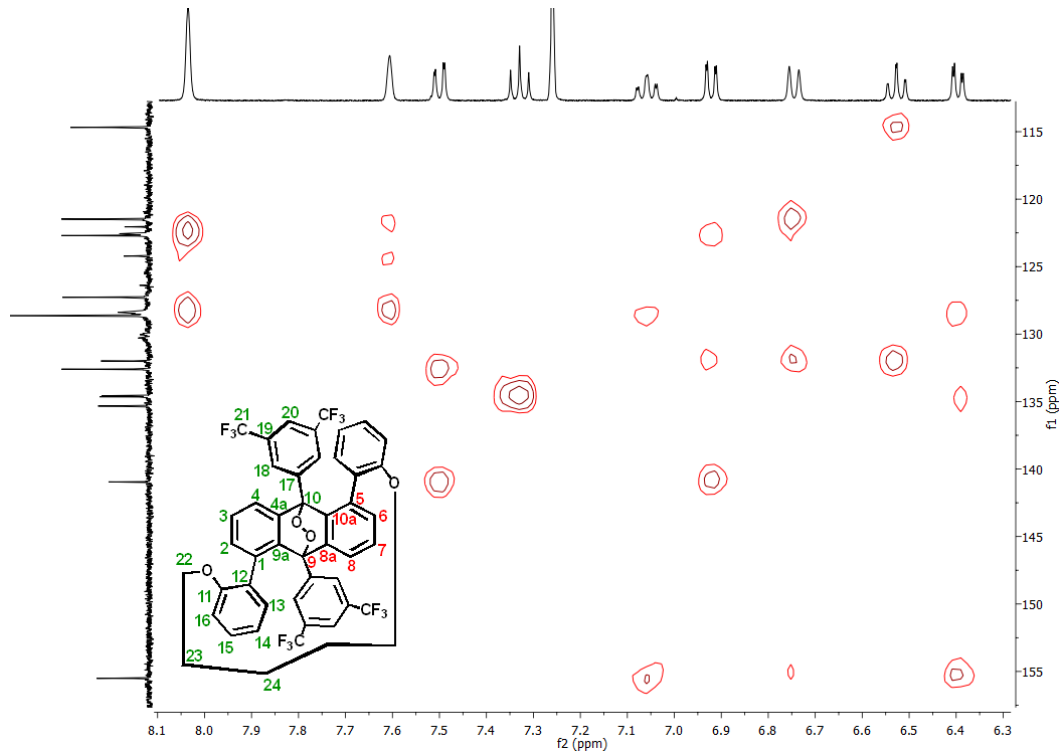


Figure S24. HMBC NMR (400 MHz) of **Ant-C5-O₂** in CDCl₃, measured at 298 K. The plot is an expanded view of the aromatic region.

S3.4 Characterization of Ant-C4-O₂

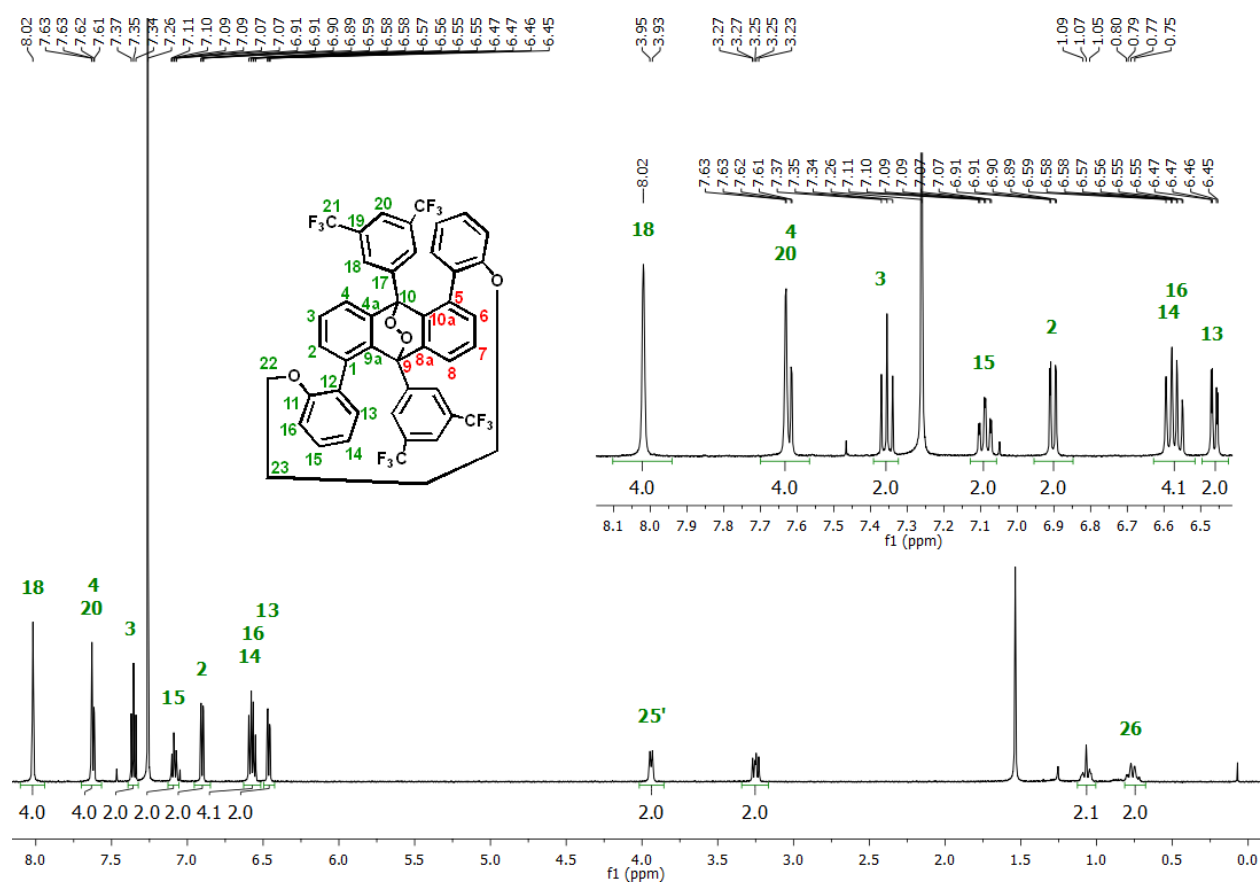


Figure S25. ¹H NMR (400 MHz) of Ant-C4-O₂ in CDCl₃, measured at 298 K.

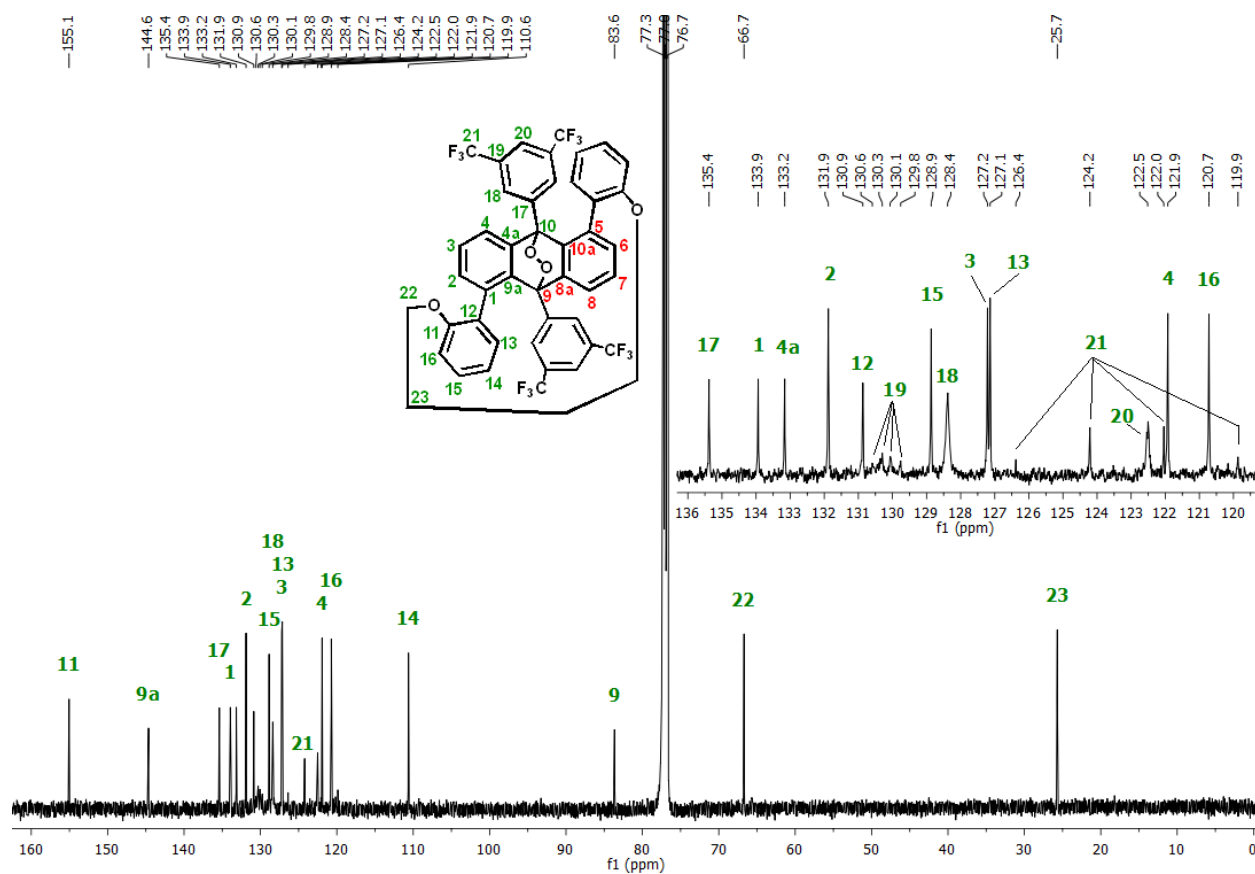


Figure S26. ¹³C NMR (125 MHz) of Ant-C4-O₂ in CDCl₃, measured at 298 K.

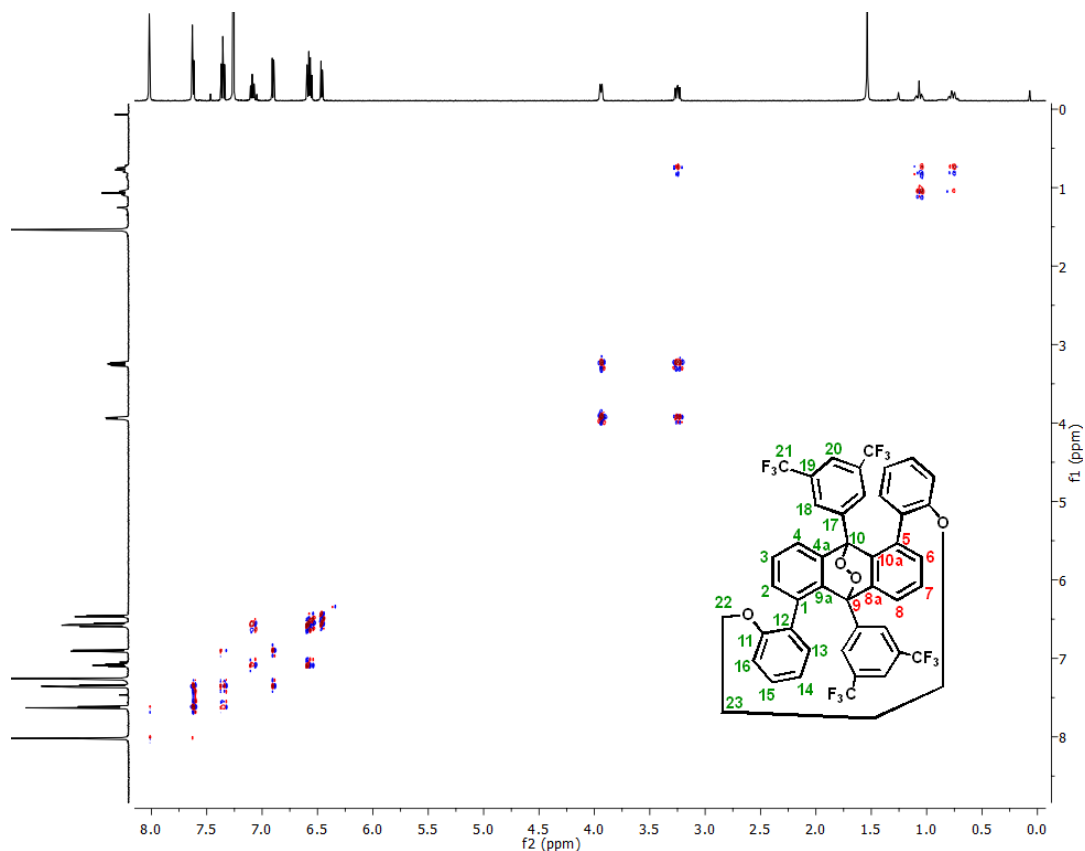


Figure S27. COSY NMR (400 MHz) of **Ant-C4-O₂** in CDCl₃, measured at 298 K.

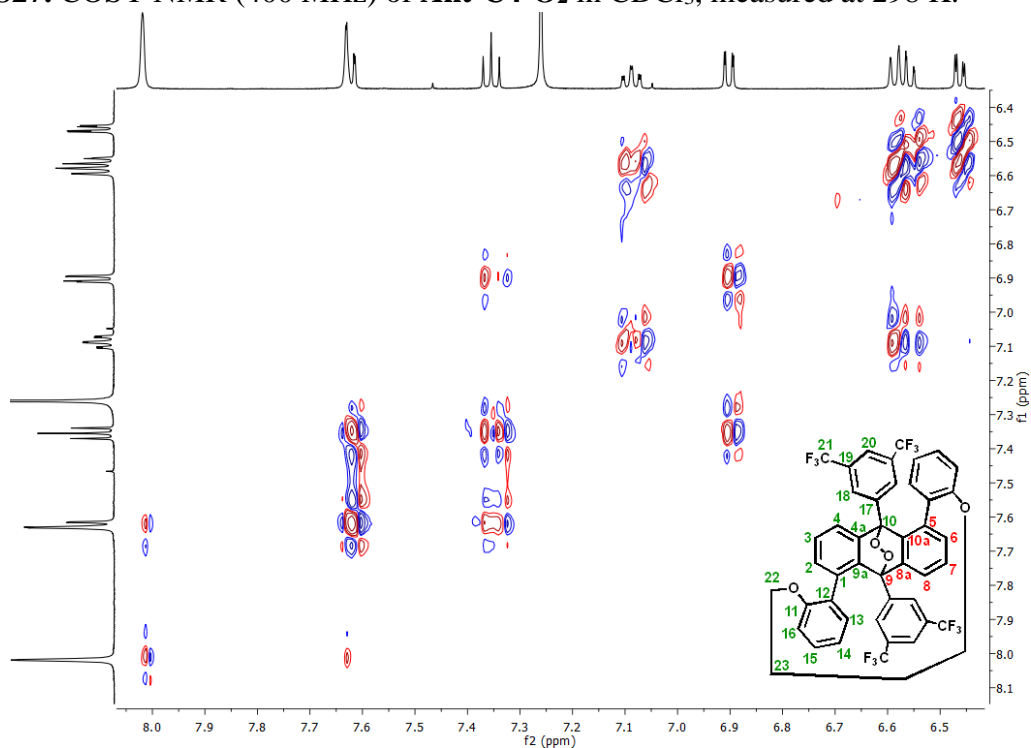


Figure S28. COSY NMR (400 MHz) of **Ant-C4-O₂** in CDCl₃, measured at 298 K. The plot is an expanded view of the aromatic region.

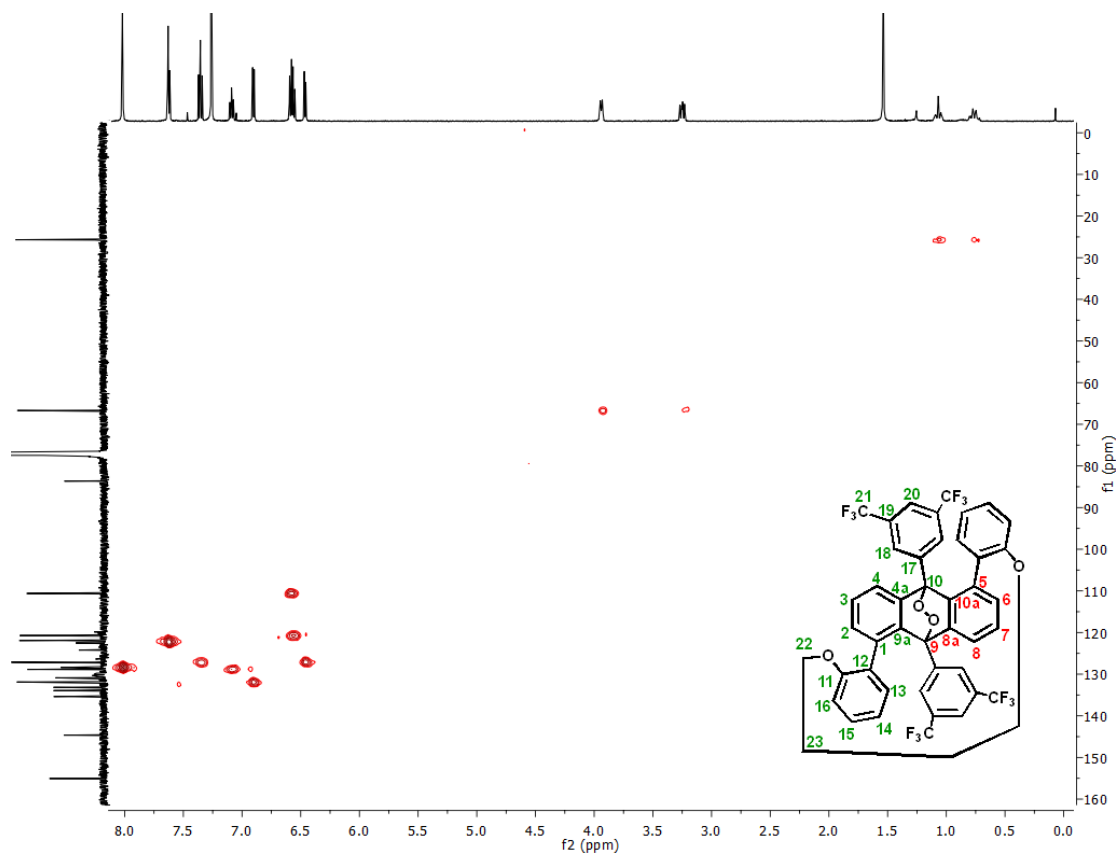


Figure S29. HSQC NMR (400 MHz) of **Ant-C4-O₂** in CDCl₃, measured at 298 K.

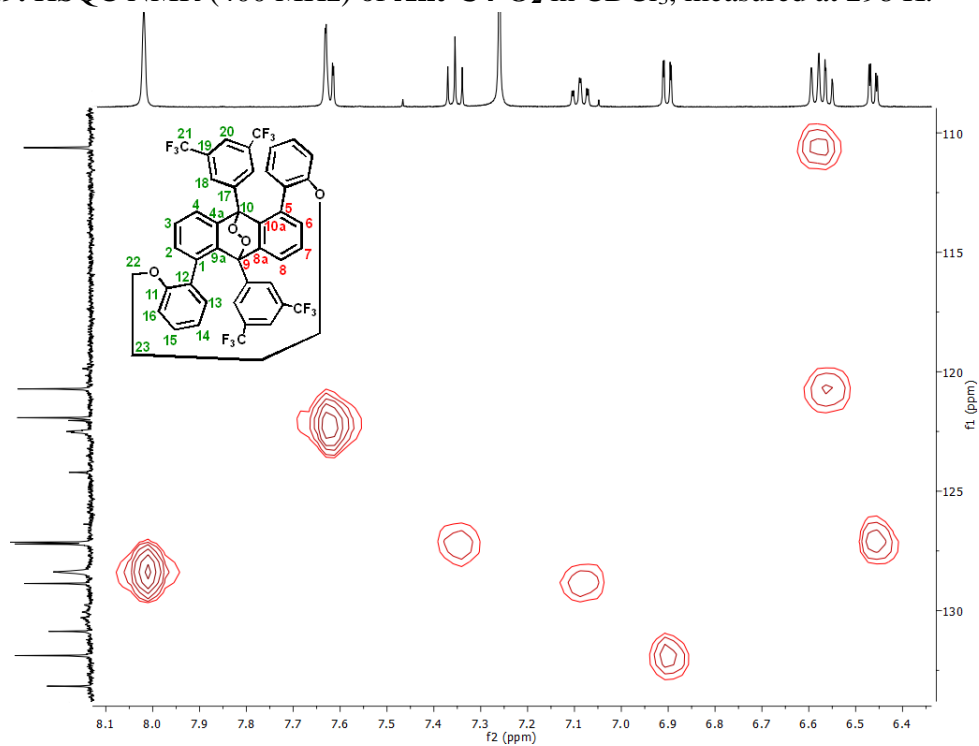


Figure S30. HSQC NMR (400 MHz) of **Ant-C4O₂** in CDCl₃, measured at 298 K. The plot is an expanded view of the aromatic region.

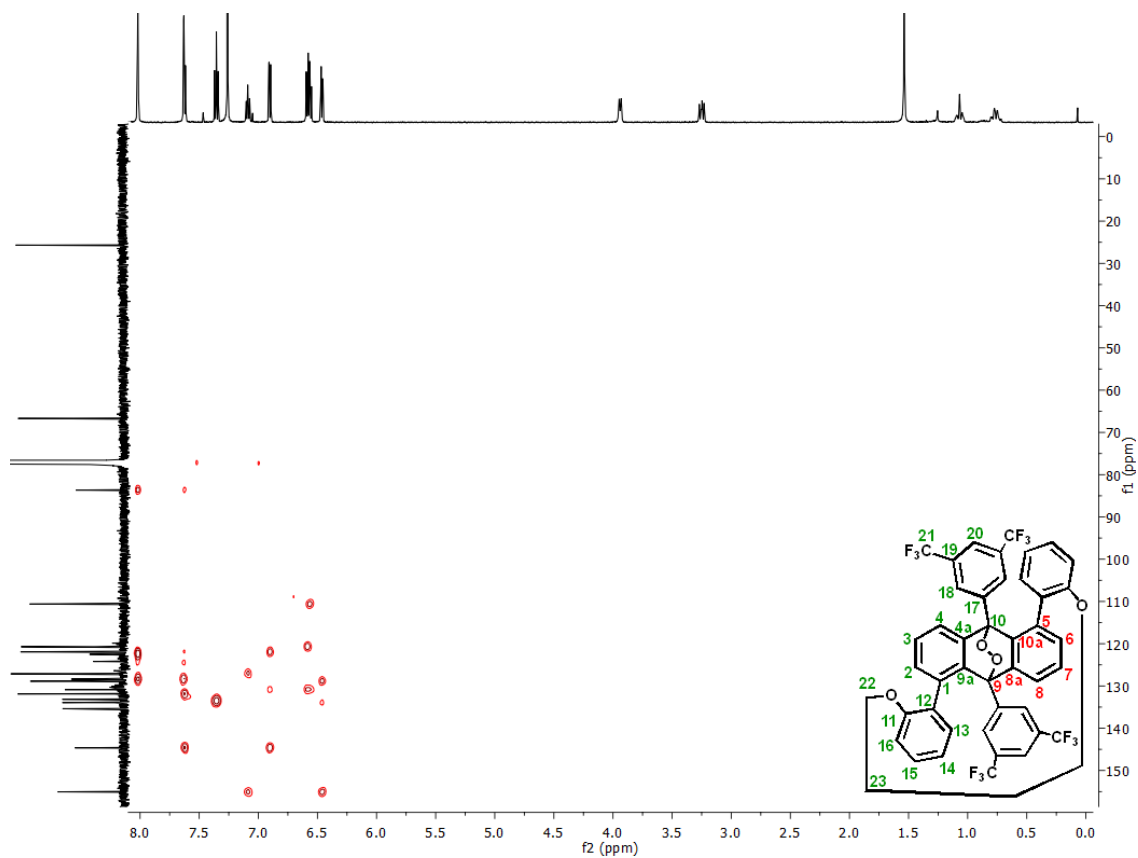


Figure S31. HMBC NMR (400 MHz) of **Ant-C4-O₂** in CDCl₃, measured at 298 K.

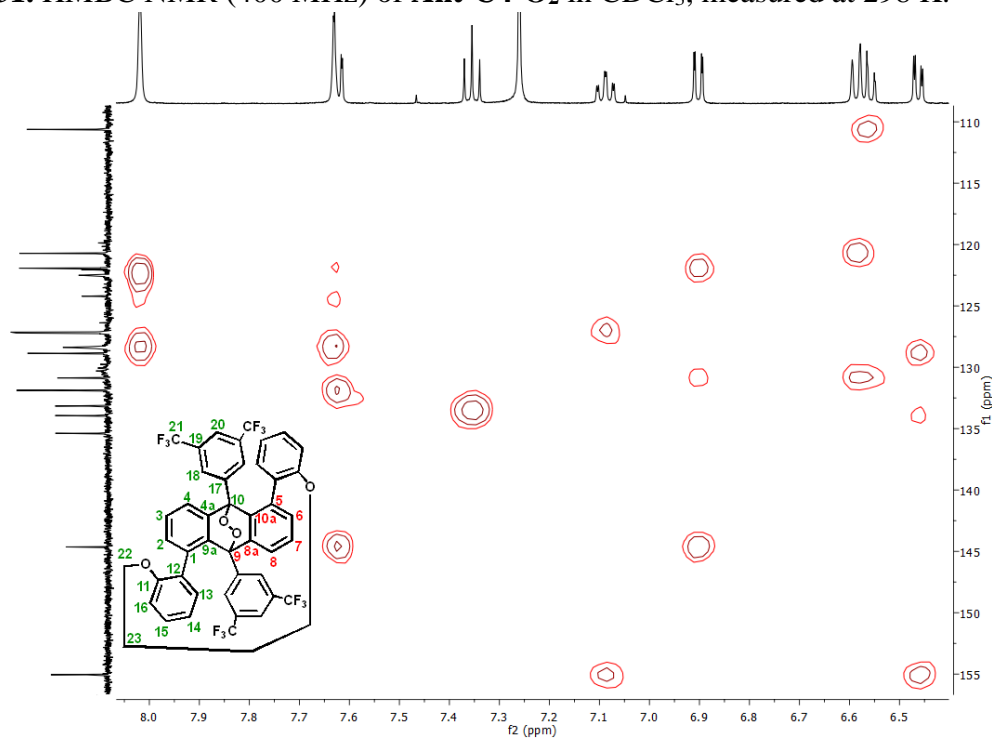


Figure S32. HMBC NMR (400 MHz) of **Ant-C4-O₂** in CDCl₃, measured at 298 K. The plot is an expanded view of the aromatic region.

S3.5 Characterization of Ant-C3-O₂

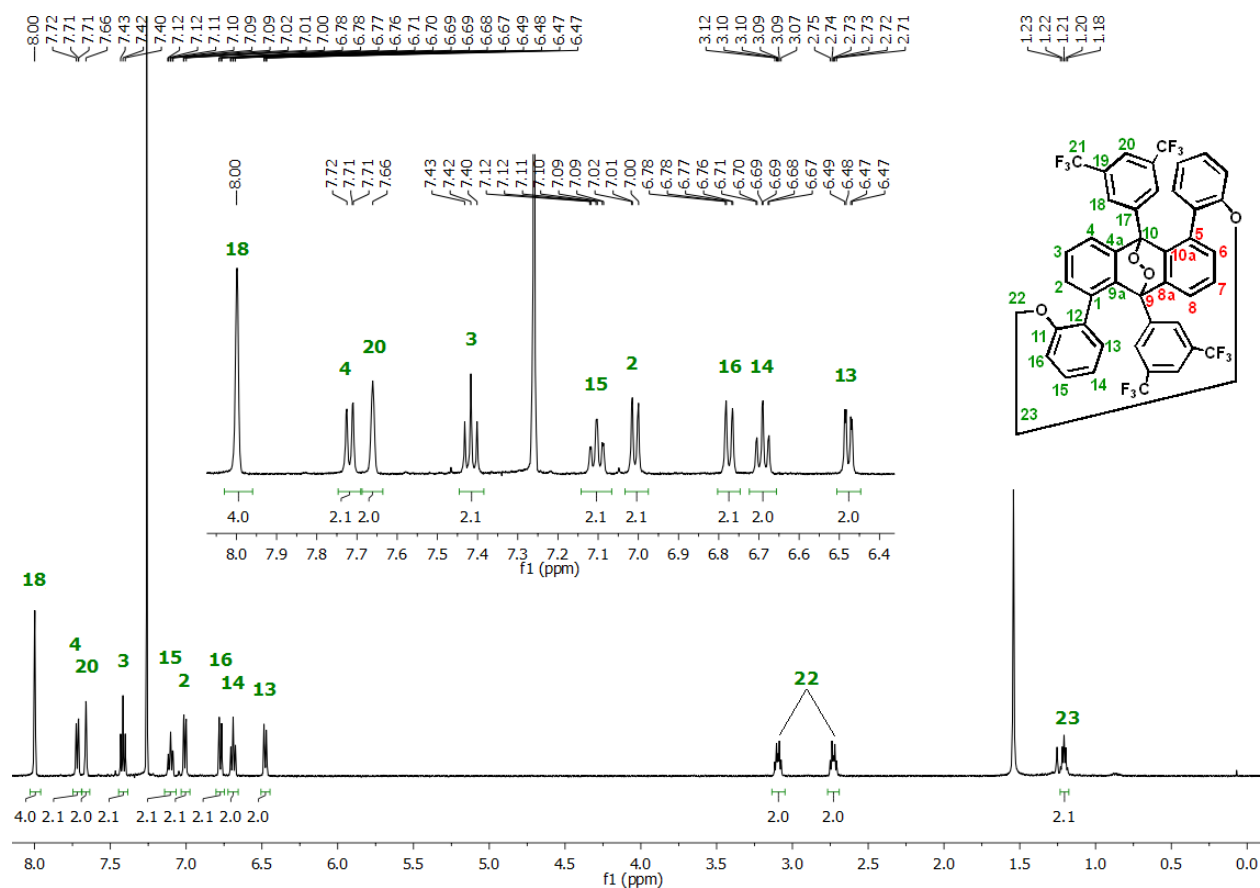


Figure S33. ¹H NMR (400 MHz) of Ant-C3-O₂ in CDCl₃, measured at 298 K.

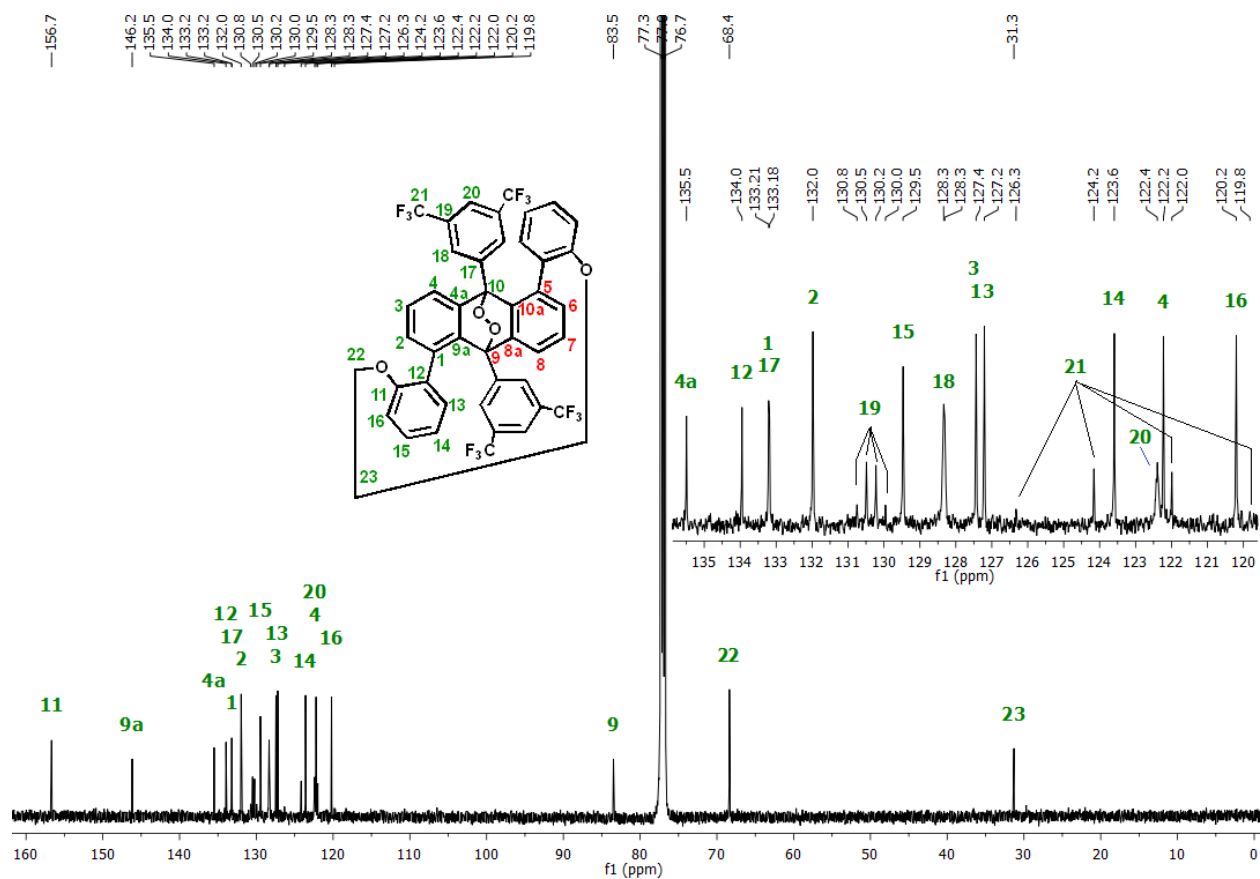


Figure S34. ^{13}C NMR (125 MHz) of **Ant-C3-O₂** in CDCl_3 , measured at 298 K.

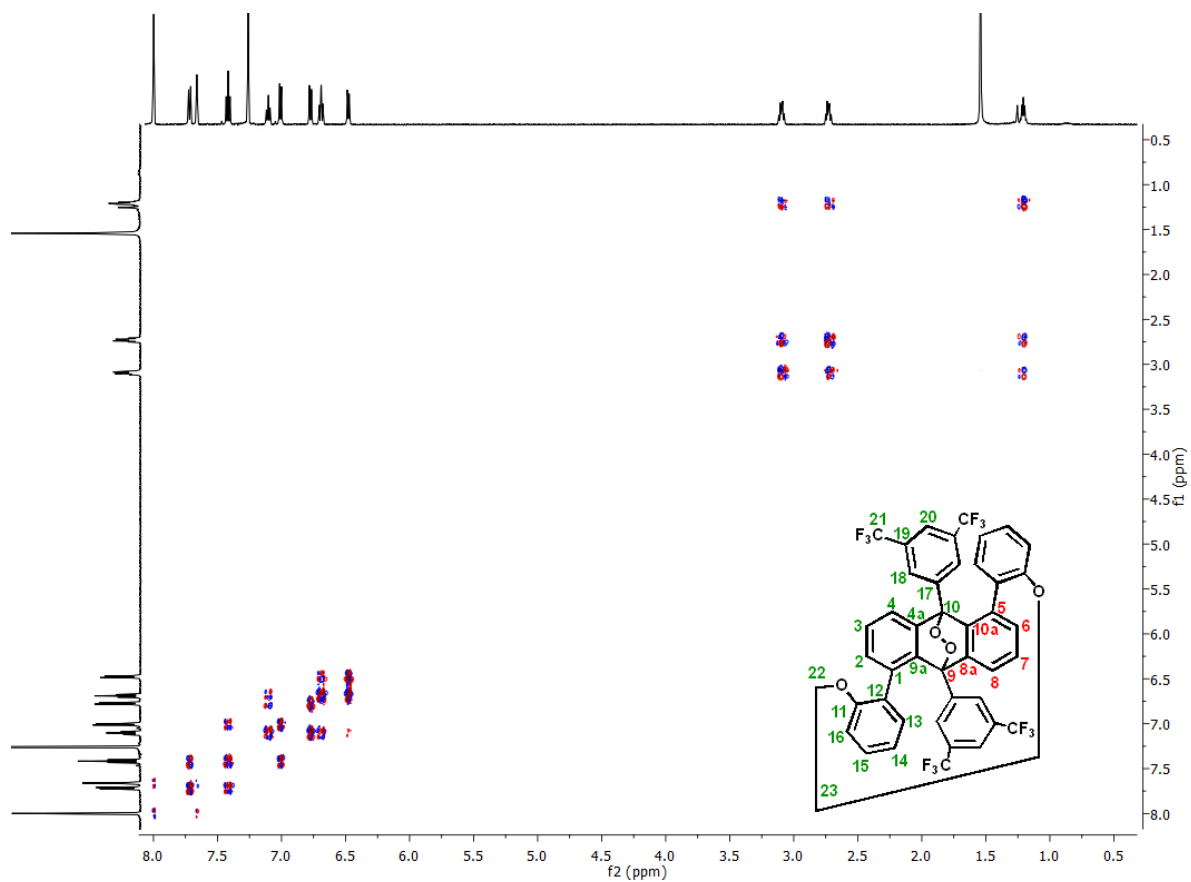


Figure S35. COSY NMR (400 MHz) of **Ant-C3-O₂** in CDCl₃, measured at 298 K.

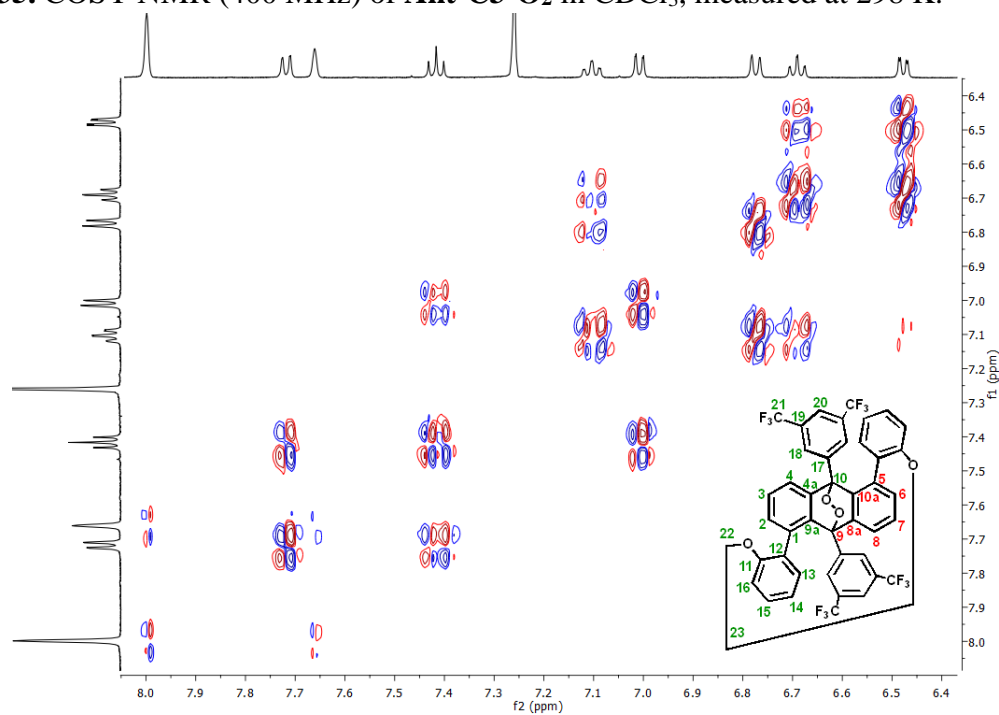


Figure S36. COSY NMR (400 MHz) of **Ant-C3-O₂** in CDCl₃, measured at 298 K. The plot is an expanded view of the aromatic region.

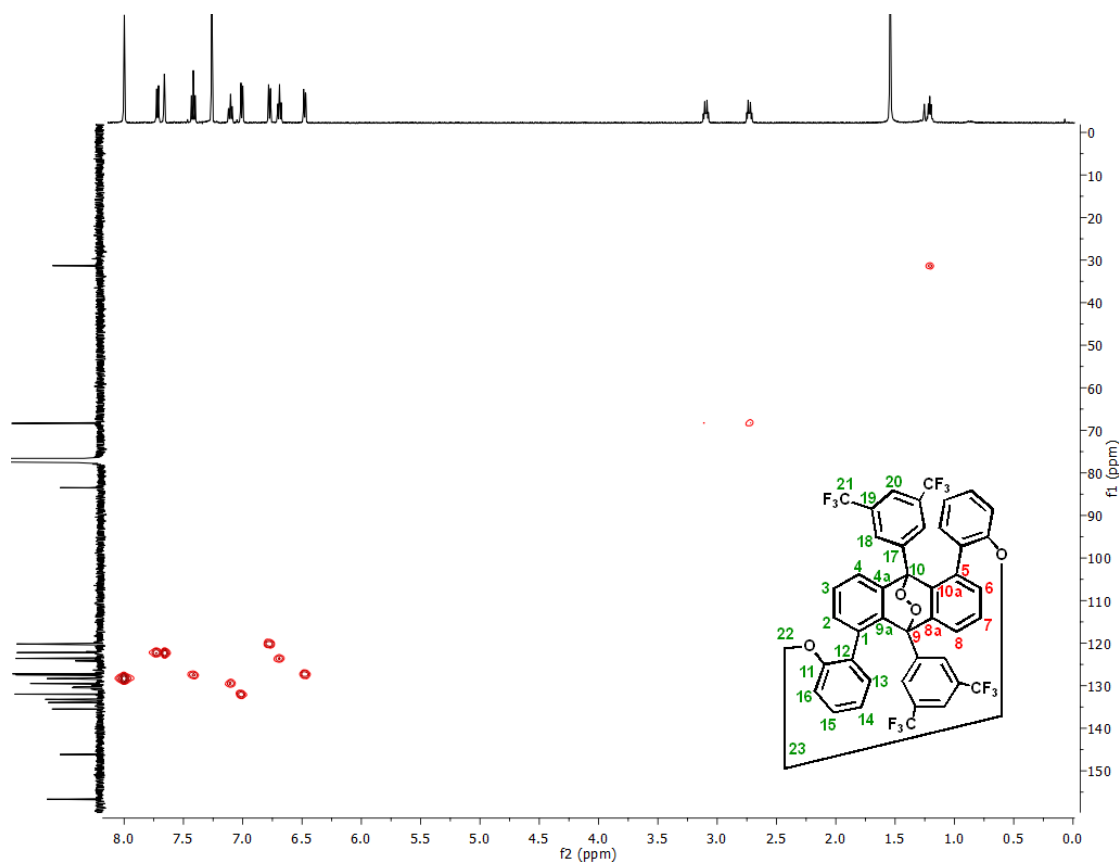


Figure S37. HSQC NMR (400 MHz) of **Ant-C3-O₂** in CDCl₃, measured at 298 K.

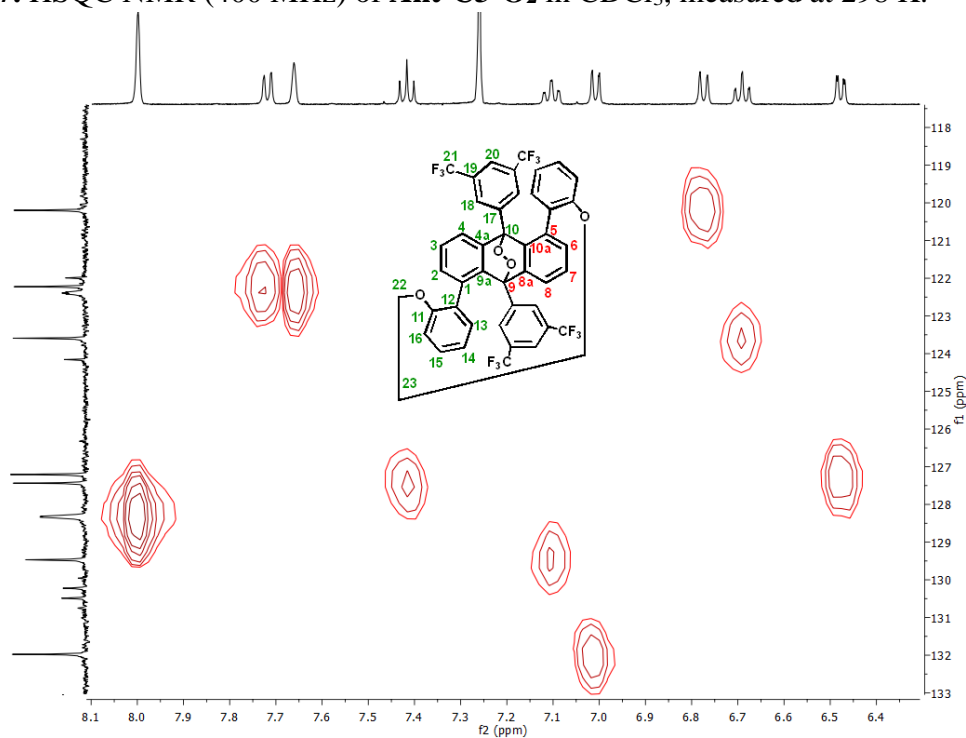


Figure S38. HSQC NMR (400 MHz) of **Ant-C3-O₂** in CDCl₃, measured at 298 K. The plot is an expanded view of the aromatic region.

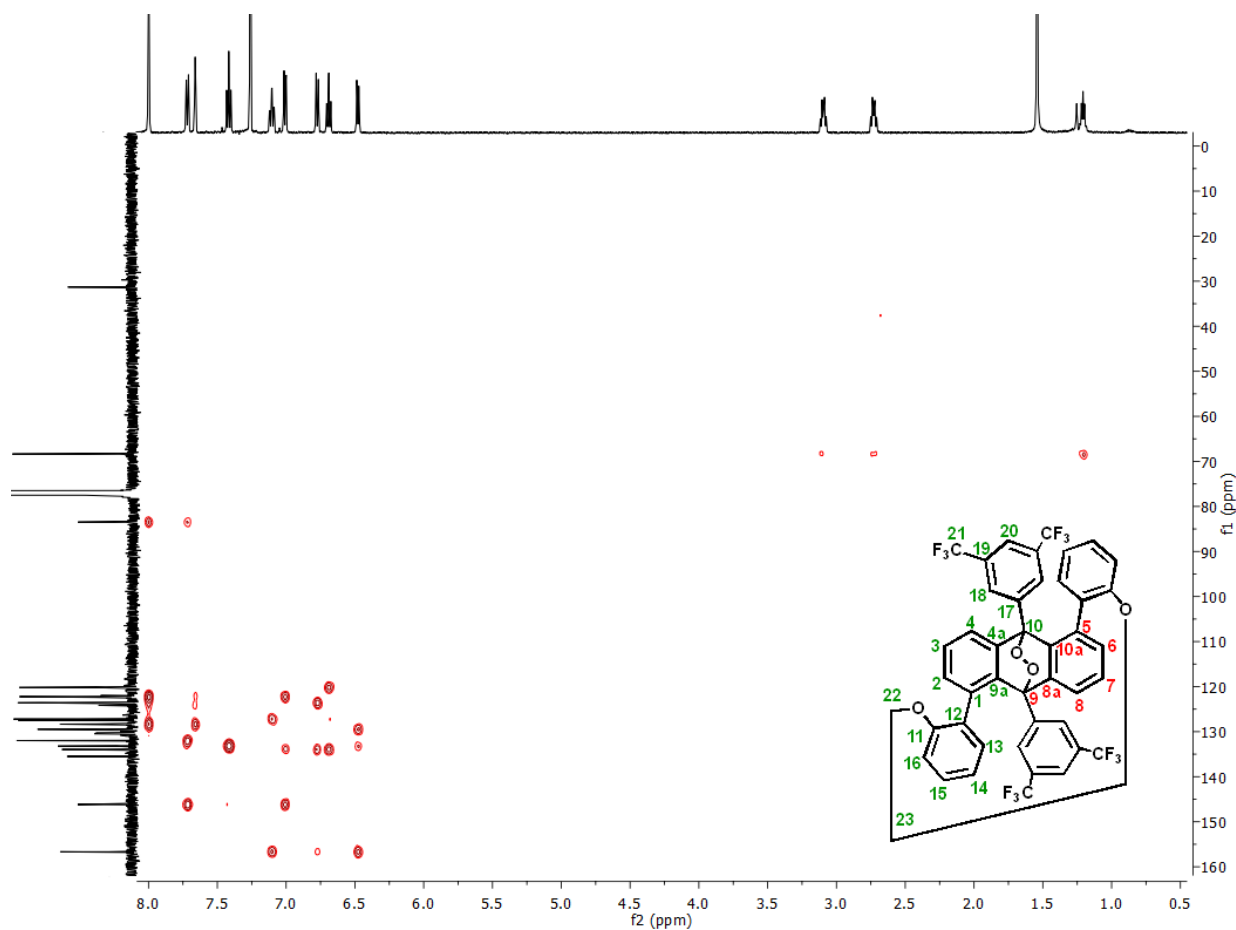


Figure S39. HMBC NMR (400 MHz) of **Ant-C3-O₂** in CDCl₃, measured at 298 K.

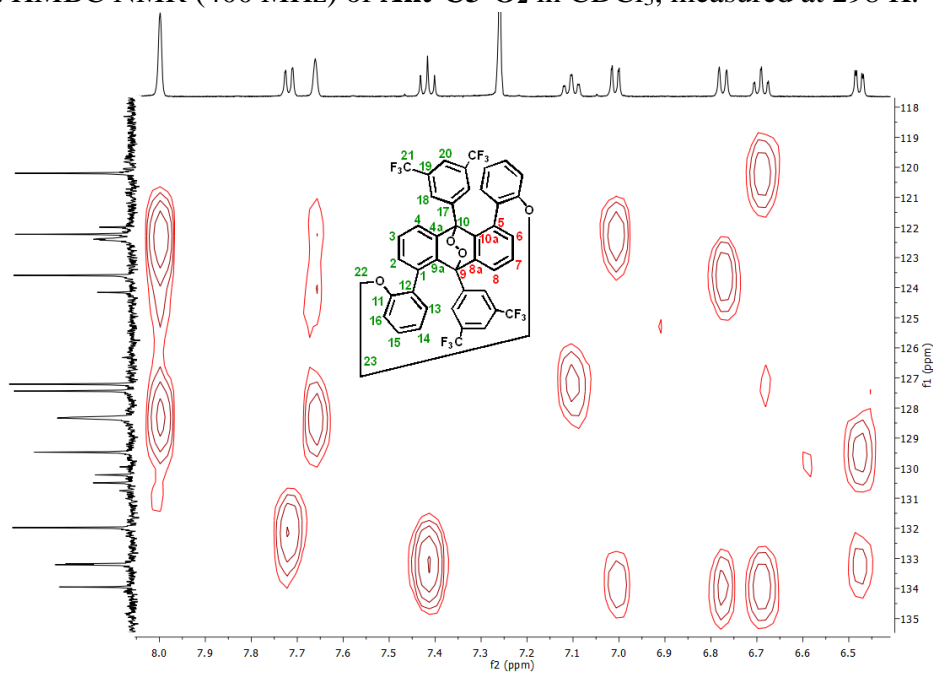


Figure S40. HMBC NMR (400 MHz) of **Ant-C3-O₂** in CDCl₃, measured at 298 K. The plot is an expanded view of the aromatic region.

S3.6 HRMS investigation to non-quantitative photo-oxidation for Ant-Open-O₂

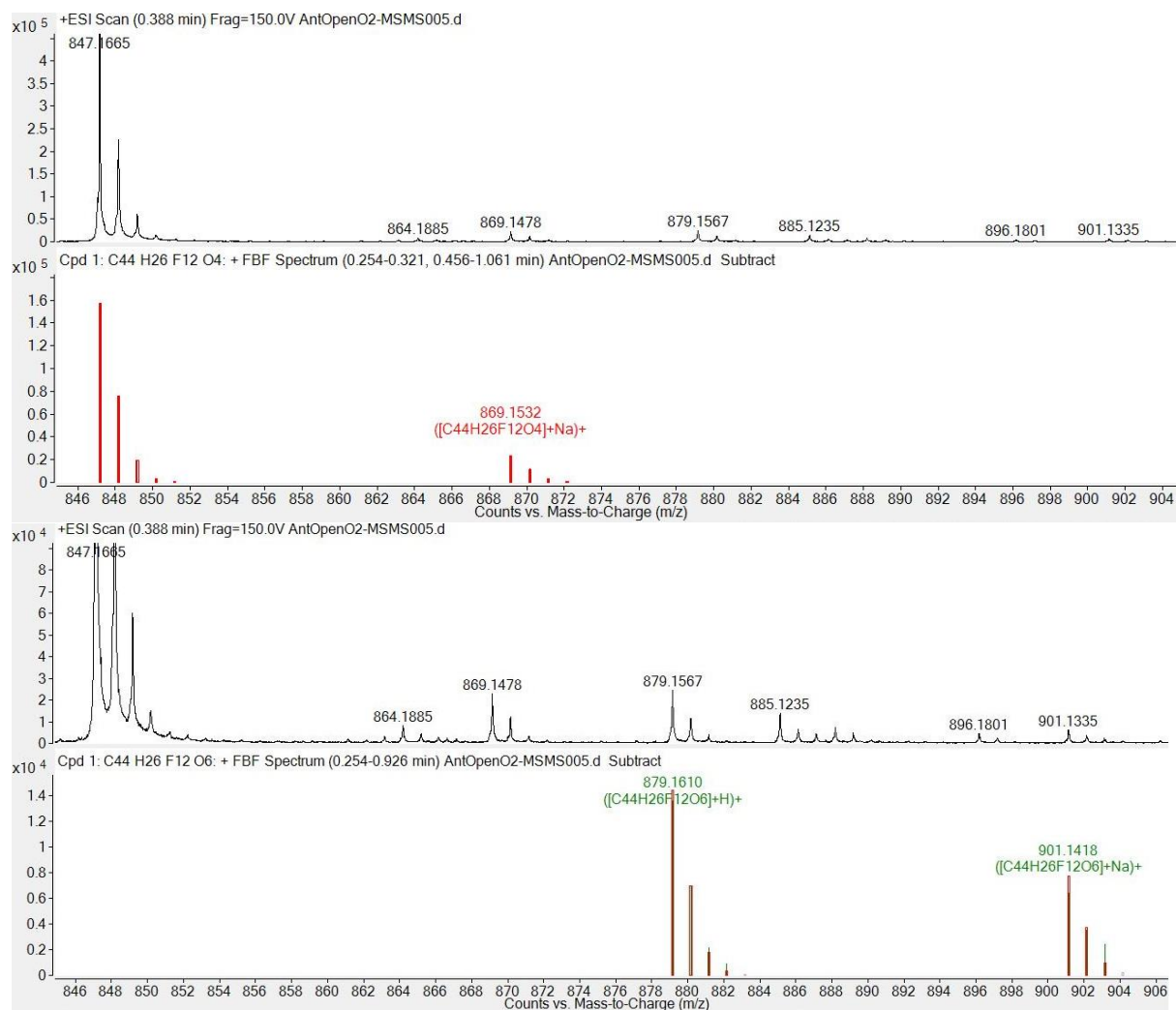


Figure S41. HRMS spectra of the reaction mixture of **Ant-Open-O₂** (top) and **Ant-Open-O₄** (bottom) in acetonitrile.

S3.7 HRMS investigation to non-quantitative photo-oxidation for Ant-C3-O₂

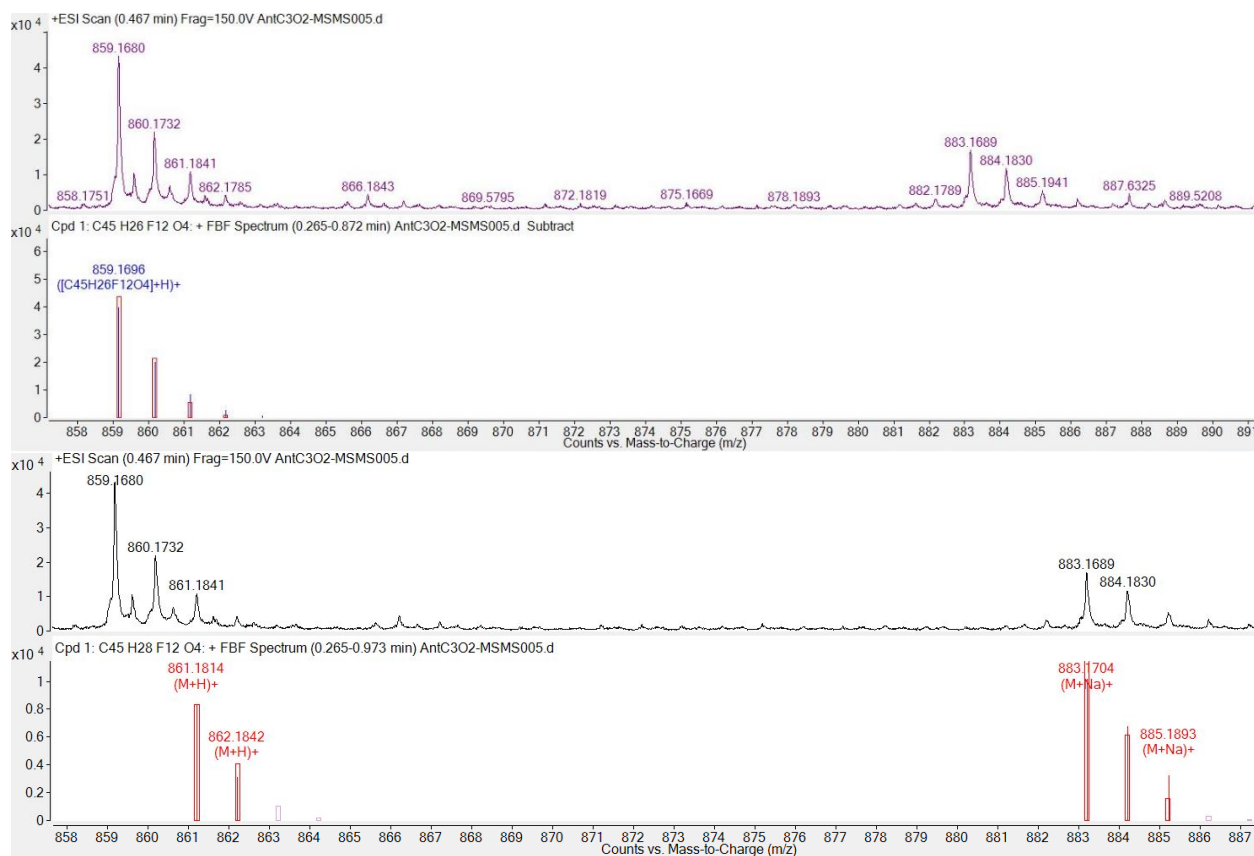


Figure S42. HRMS spectra of the reaction mixture of **Ant-C3-O₂** (top) and **Ant-C3-(OH)₂** (bottom) in acetonitrile.

S4 Time-dependent photo-oxidation of anthracenes

S4.1 Photo-oxidation studied at different wavelengths

The photochemical reaction was followed over time, where at least 90% conversion of the parent twistacenes was considered. The twistacenes were exposed to a 365 nm lamp as the molar absorptivities (ϵ) of all the twistacenes at this wavelength are almost identical. Moreover, the dependence of wavelength was also observed when the photo-oxidation was studied at 427 nm.

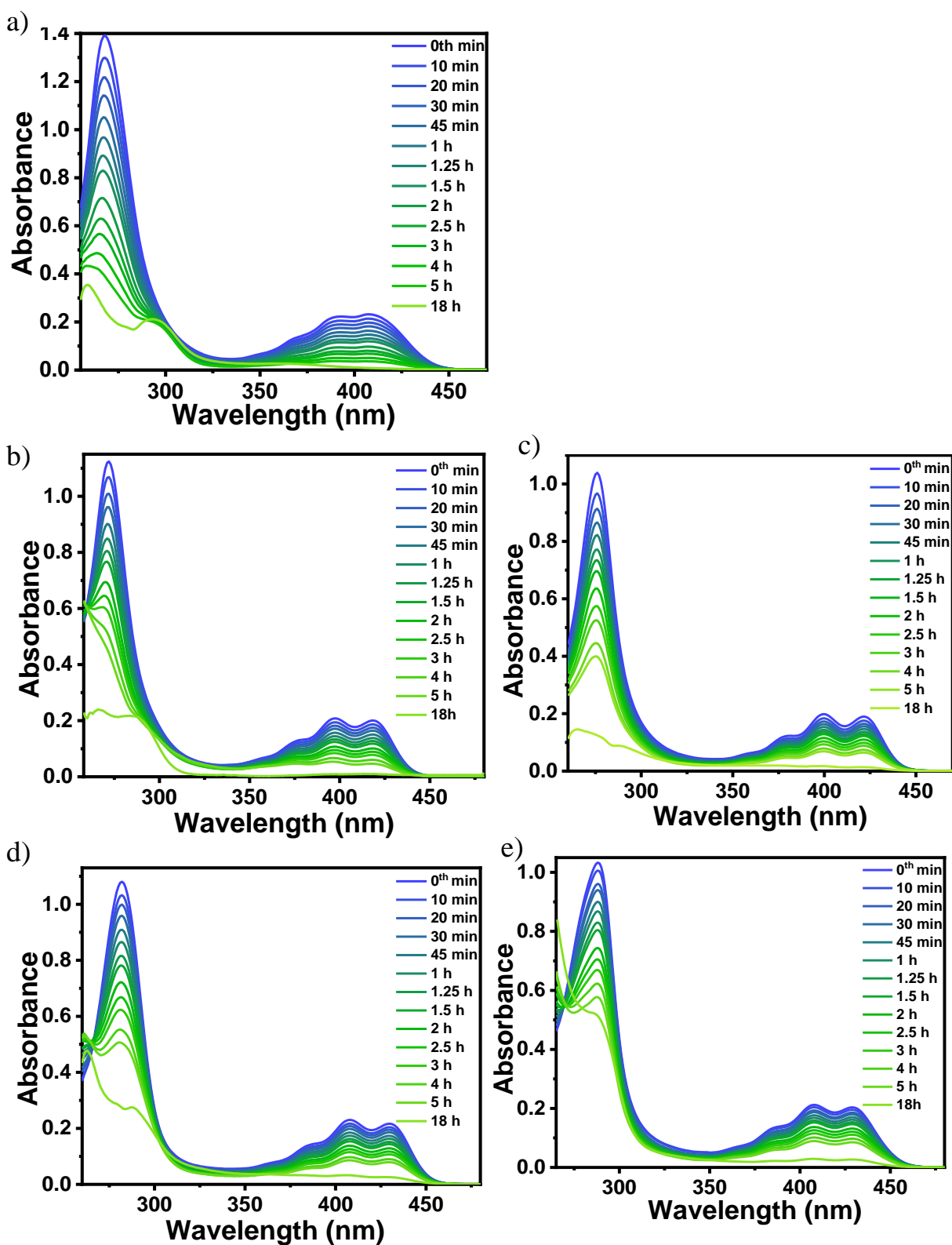


Figure S43. Gradual photo-oxidation of (a) **Ant-Open**, (b) **Ant-C6**, (c) **Ant-C5**, (d) **Ant-C4** and (e) **Ant-C3** in chloroform at room temperature under a 365 nm lamp.

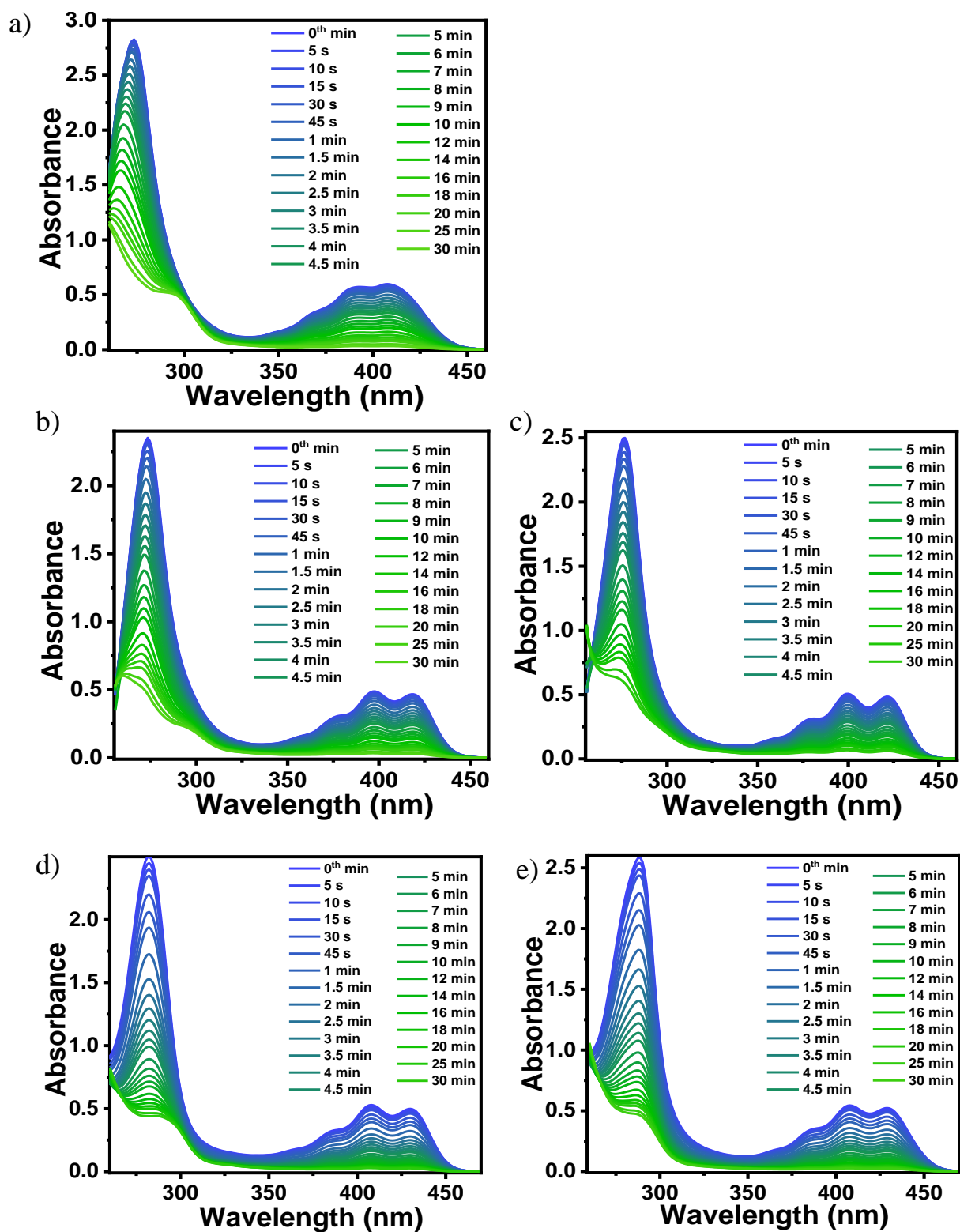


Figure S44. Gradual photo-oxidation of (a) **Ant-Open**, (b) **Ant-C6**, (c) **Ant-C5**, (d) **Ant-C4** and (e) **Ant-C3** in chloroform at room temperature under a 427 nm lamp.

S4.2 Photo-oxidation kinetics

The electronic transition in the photo products centers on the 1B_b band of the parent molecules. However, photobleaching could be studied unambiguously from the bleaching of the 1L_a transitions of the parent twistacenes because of the absence of any absorbance from the anthracene peroxides in that spectral region. Consequently, photo-oxidation kinetics was monitored from the change in the absorbance of the lowest energy vibronic shoulder of the 1L_a transition against time. The kinetic data could be established from the change in absorbance because twistacene concentration was kept constant and because oxygen concentration could be assumed to be constant as solvent conditions (solvent and amount) were identical in all experiments.

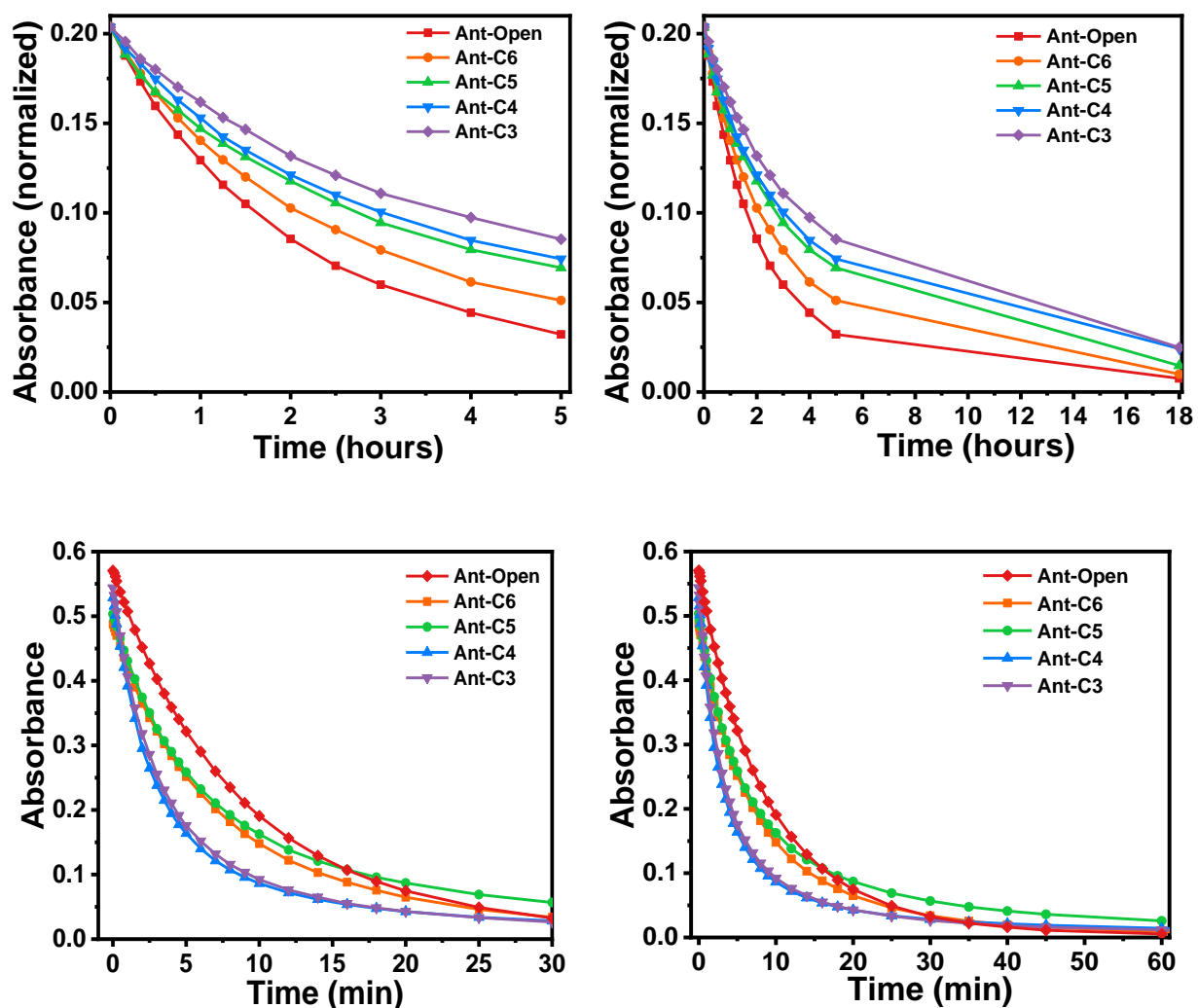


Figure S45. Gradual photo-oxidation of the twistacenes at 365 nm (top) 427 nm (bottom).

S4.2.1 Photo-oxidation in the presence of methylene blue

Anthracenes are excellent singlet quenchers because of their ability to act as both photosensitizer and singlet state reagent to singlet oxygen ($^1\text{O}_2$). To gain further insight into the mechanism of the photo-oxidation reaction of the twistacenes and $^1\text{O}_2$, methylene blue (MB) was used as an external sensitizer. The photooxidation was performed by irradiation of the twistacene (2.96×10^{-5} M) and MB (2.96×10^{-6} M, 0.1 equivalent) at 617 nm using a Mightex LED lamp. This allowed us to monitor the photo-oxidation reaction of the singlet states of both twistacene and atmospheric oxygen under conditions in which twistacenes were not expected to perform a sensitizer role. We performed the experiment at constant concentrations of **Ant-C6** and **Ant-C3** and we assumed that the oxygen concentrations were identical in both cases under atmospheric pressure. The presence of MB resulted in **Ant-C3** photo-oxidizing more quickly than **Ant-C6** (Figures S47c).

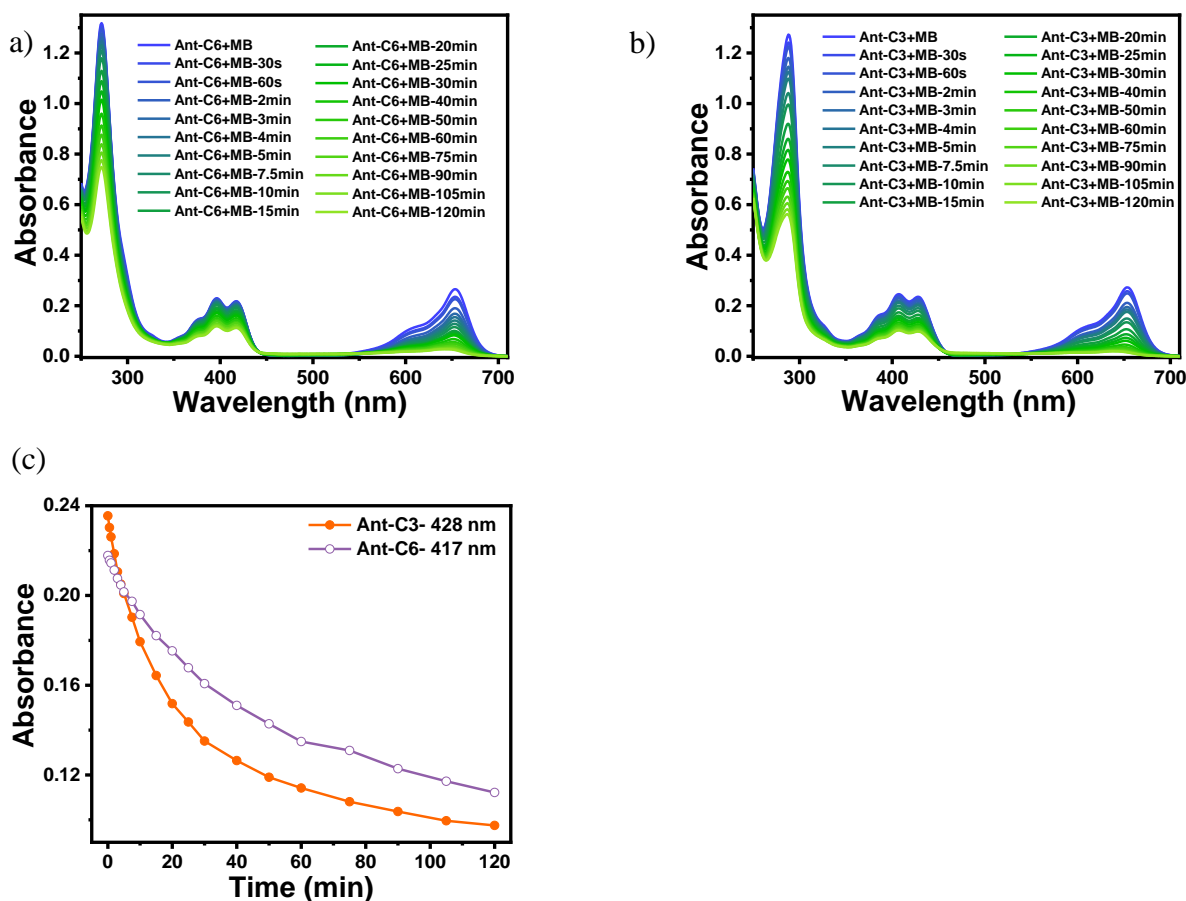


Figure S46. Spectral change during photo-oxidation of (a) **Ant-C6** and (b) **Ant-C3** in the presence of methylene blue (MB) in chloroform when irradiated at 617 nm; (c) the change in absorbance with time for the lowest-energy vibronic shoulder of the $^1\text{L}_a$ transition for **Ant-C6** and **Ant-C3**.

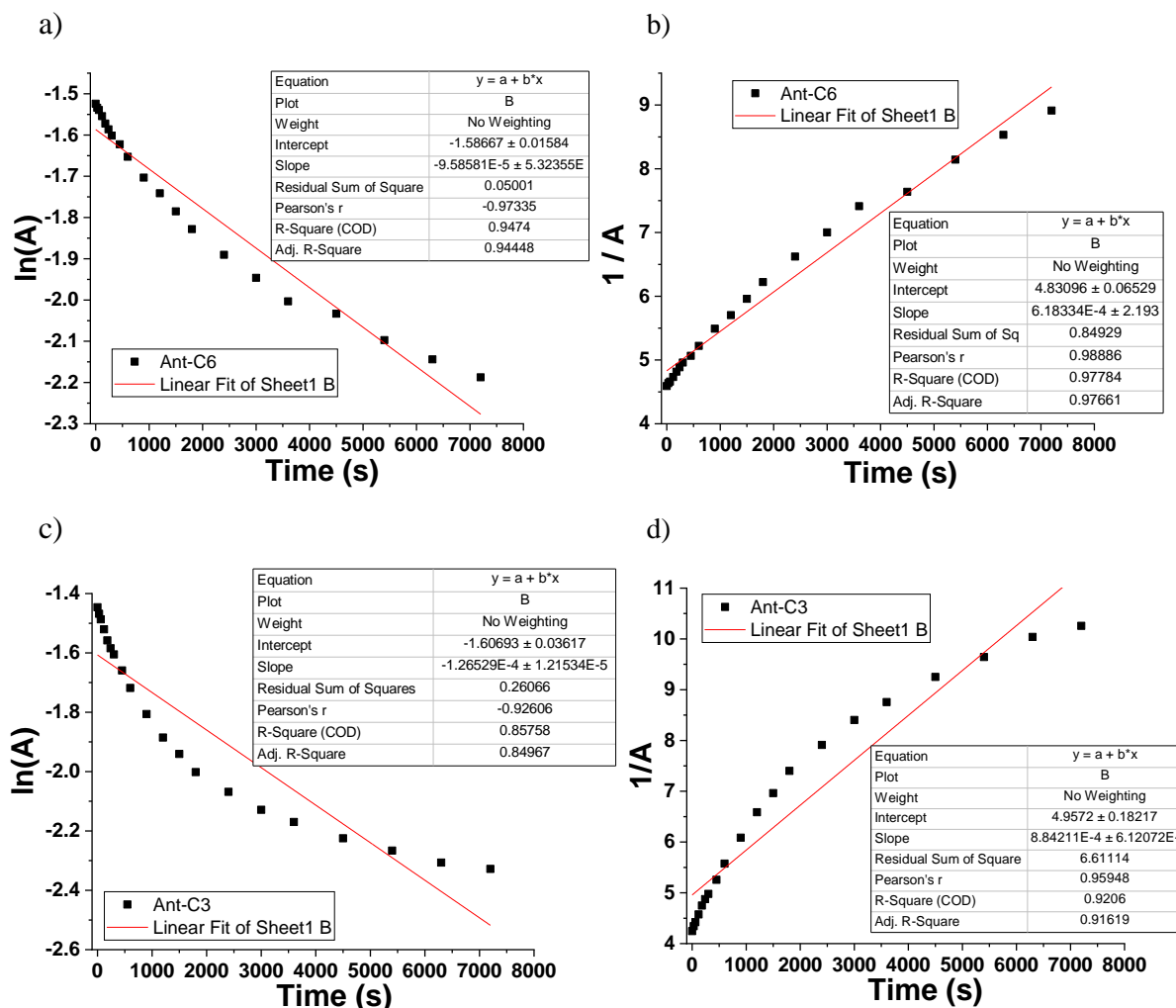


Figure S47. Kinetic fitting of the photooxidation of **Ant-C6** and **Ant-C3**. (a) First order to **Ant-C6**, (b) second order to **Ant-C6**, (c) first order to **Ant-C3** and (d) second order to **Ant-C3**.

S4.3 Low temperature photoswitching of Ant-C4

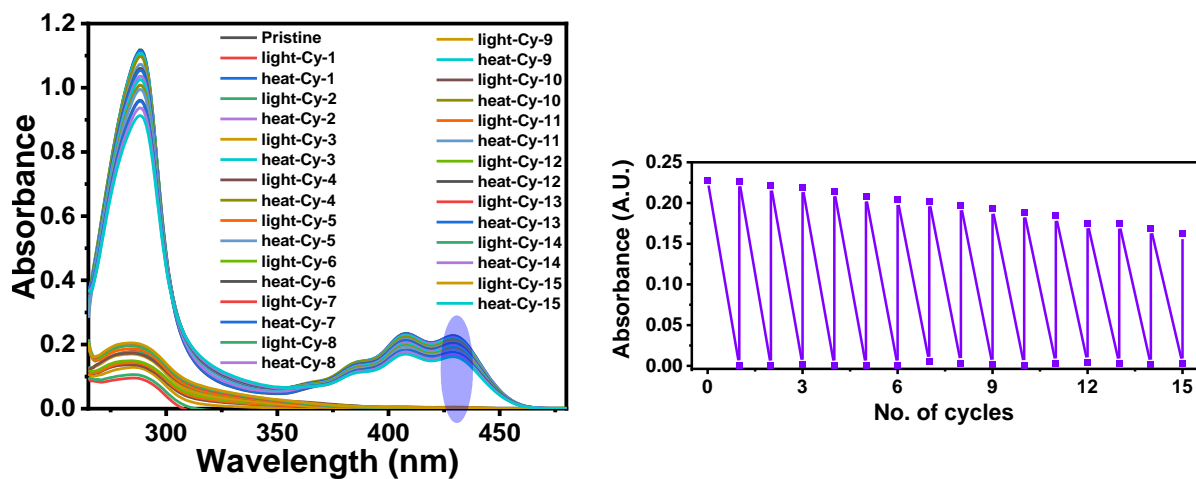


Figure S47. UV-vis spectral change of **Ant-C4** during *fifteen* repetitive cycles of photo-oxidation and thermal reduction in 1, 1, 2, 2-tetrachloroethane; room temperature (left) and -5 °C (right). Photoswitching of **Ant-C4** during repetitive cycles of oxidation/reduction in 1, 1, 2, 2-tetrachloroethane. Photo-oxidations were performed at -5 °C using a 427 nm light source, whereas the cycloreversion was studied at 110 °C.

S4.4 High temperature photoswitching of Ant-C4

Photoswitching of **Ant-C4** and **Ant-Open** was studied during *five* repetitive cycles of oxidation/reduction in 1, 1, 2, 2-tetrachloroethane. Photo-oxidation was performed here at -5 °C using a 427 nm light source, whereas the cycloreversion was studied at 135 °C.

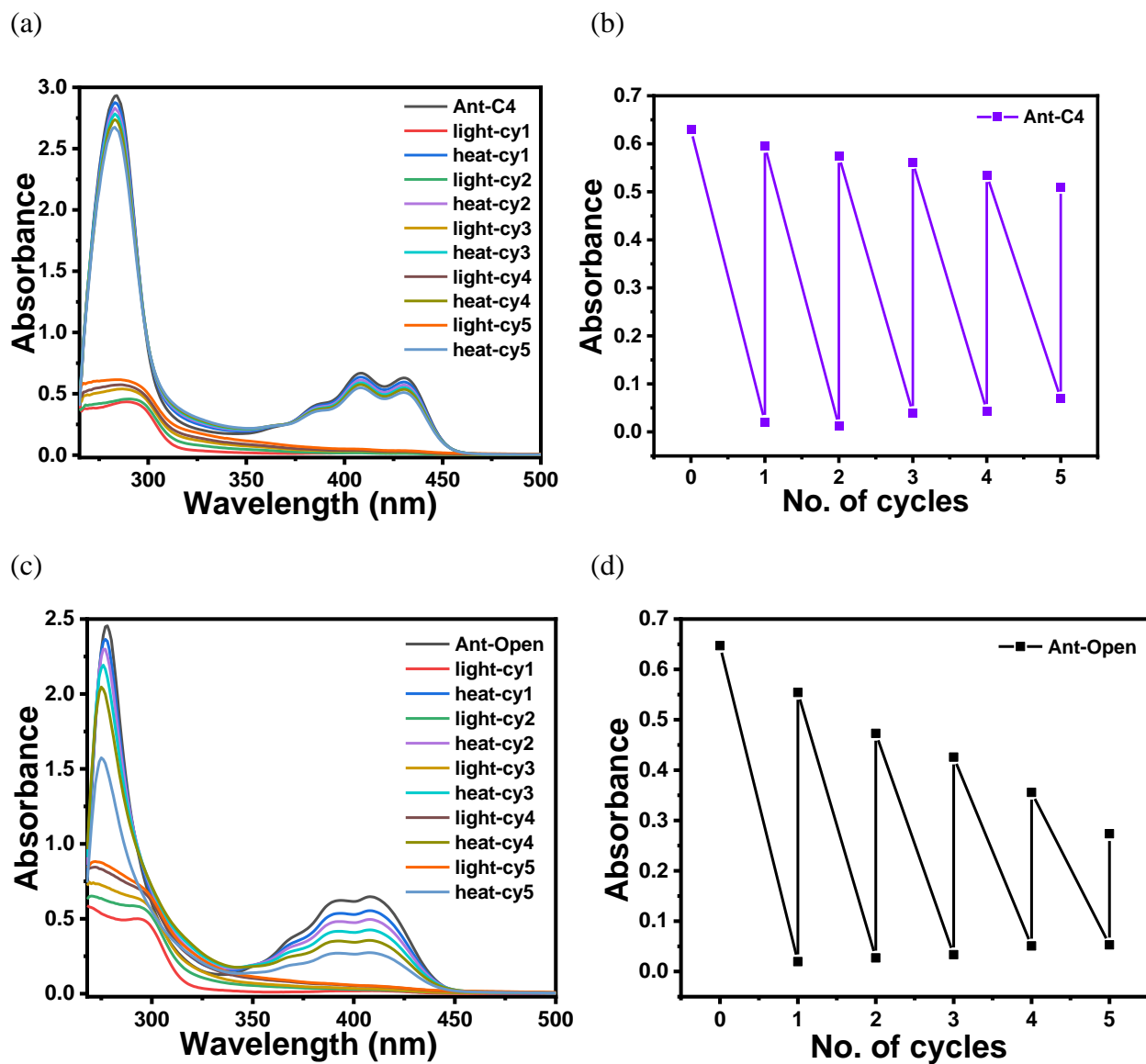


Figure S48. (a) Spectral changes during photoswitching and (b) change in absorbance with the number of switching cycle for **Ant-C4/Ant-C4-O₂**. (c) Spectral changes during photoswitching and (d) change in absorbance vs the number of switching cycles for **Ant-Open/Ant-Open-O₂**.

S5 UV-vis absorption spectra of the peroxides

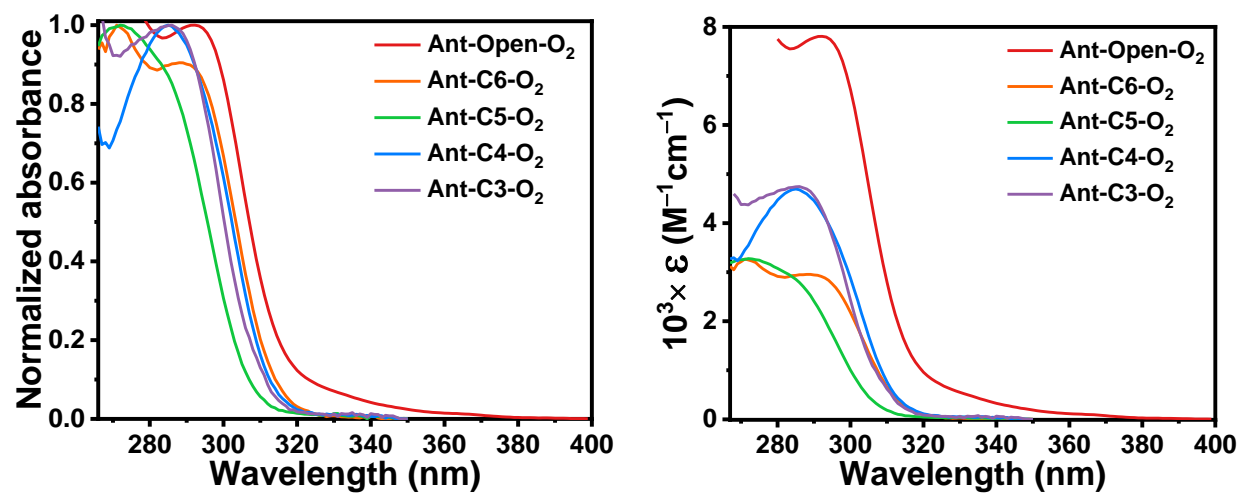


Figure S49. The experimental UV-vis absorption spectra of the twistacene peroxides; (a) normalized spectra and (b) molar absorptivity recorded in 1,1,2,2-tetrachloroethane at 298 K.

Table S1. Extinction coefficients (ϵ , $\text{M}^{-1}\text{cm}^{-1}$) of **Ant-Cn** at irradiation wavelengths 365 nm and 427 nm.

Compounds	365 nm	427 nm
Ant-Open	5227	4001
Ant-C6	3287	4570
Ant-C5	2743	5664
Ant-C4	2893	7666
Ant-C3	2863	7811

S6 Kinetics of the thermal retro Diels-Alder reaction of the twistacene peroxides

Ant-Open-O₂ was found to be completely robust under ambient conditions and to convert to the parent twistacene only at temperatures $>100\text{ }^{\circ}\text{C}$. However, the tethered peroxides started to convert to twistacenes via thermal retro Diels-Alder reaction at ambient conditions, although the conversion rate was very slow. Raising the temperature to $\geq 60\text{ }^{\circ}\text{C}$ raised the reaction rate. Thermochemical analyses of the cycloreversion reactions of endoperoxides were accomplished using ^1H NMR at variable temperatures. The conversion of the endoperoxides to the parent twistacenes was examined by plotting the number of moles (n) of the corresponding peroxides against time at four different temperatures (Figure S53). The activation parameters (enthalpy, entropy, and Gibbs free energy) of the retro Diels-Alder reactions were obtained using Eyring's equation by correlating between these rate constants and the corresponding temperatures (Figure S54).

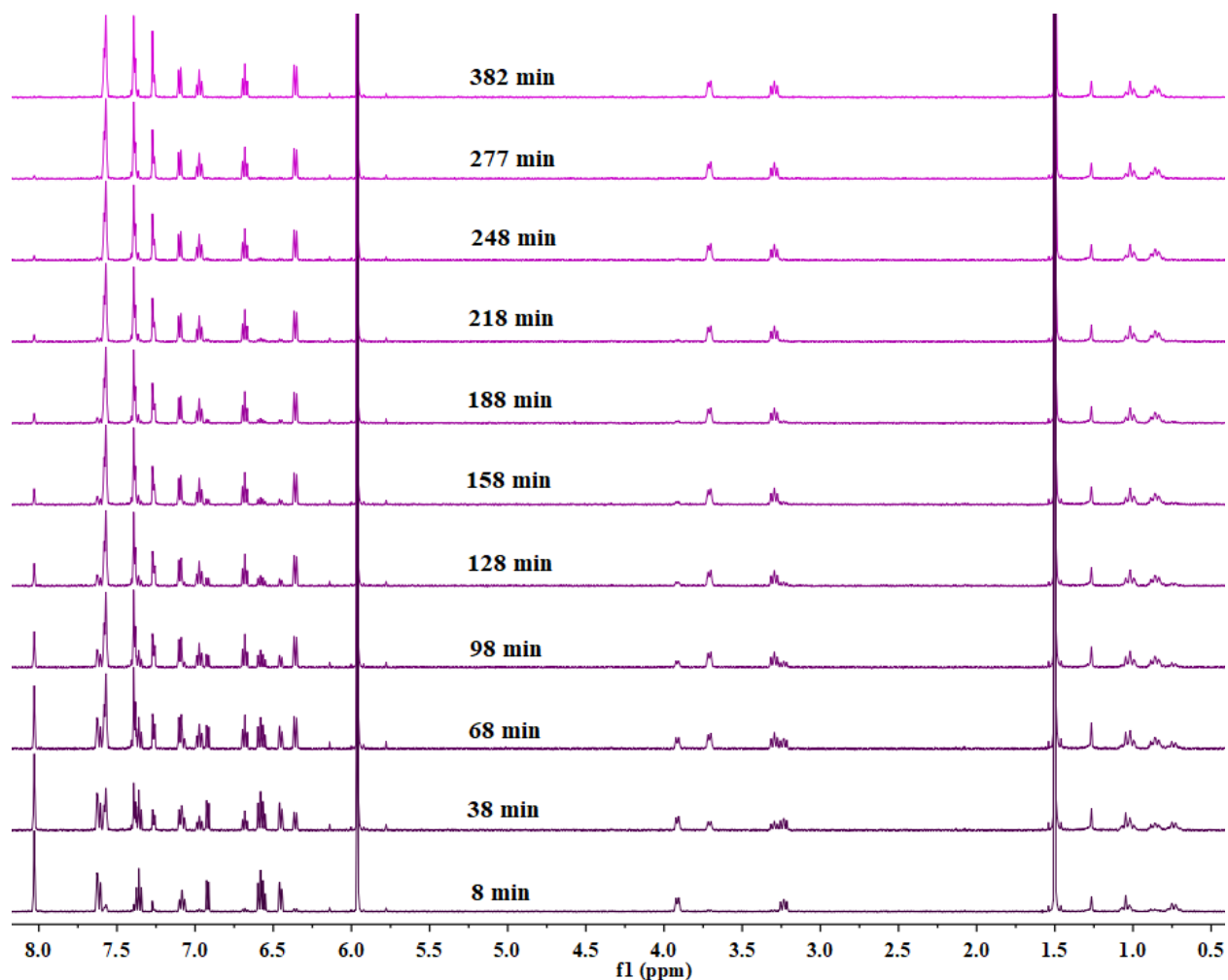


Figure 50. Cycloreversion reaction profile of **Ant-C4-O₂** to **Ant-C4** monitored by ^1H NMR spectra in $\text{C}_2\text{D}_2\text{Cl}_4$ at 338 K. These spectra are representative of all the variable temperature photo-oxidation rate measurements that were used in this work to extract the kinetic parameters for the cycloreversion reaction of the **Ant-Cn-O₂** series.

Table S2. Rate constants for the retro Diels-Alder reaction of the endoperoxides.

	Rate constants (s ⁻¹)				
T(K)	Ant-Open-O ₂	Ant-C6-O ₂	Ant-C5-O ₂	Ant-C4-O ₂	Ant-C3-O ₂
328	-	-	-	-	0.000076
333	-	-	-	0.000100	0.000134
338	-	-	0.000059	0.000200	0.000239
343	-	-	0.000110	0.000313	0.000412
348	-	-	0.000204		-
353	-	0.000069	0.000604	0.001070	-
358	-	0.000139	-	-	-
363	-	0.000230	-	-	-
368	-	0.000431	-	-	-
383	0.000047	-	-	-	-
388	0.000086	-	-	-	-
393	0.000154	-	-	-	-
403	0.000460	-	-	-	-

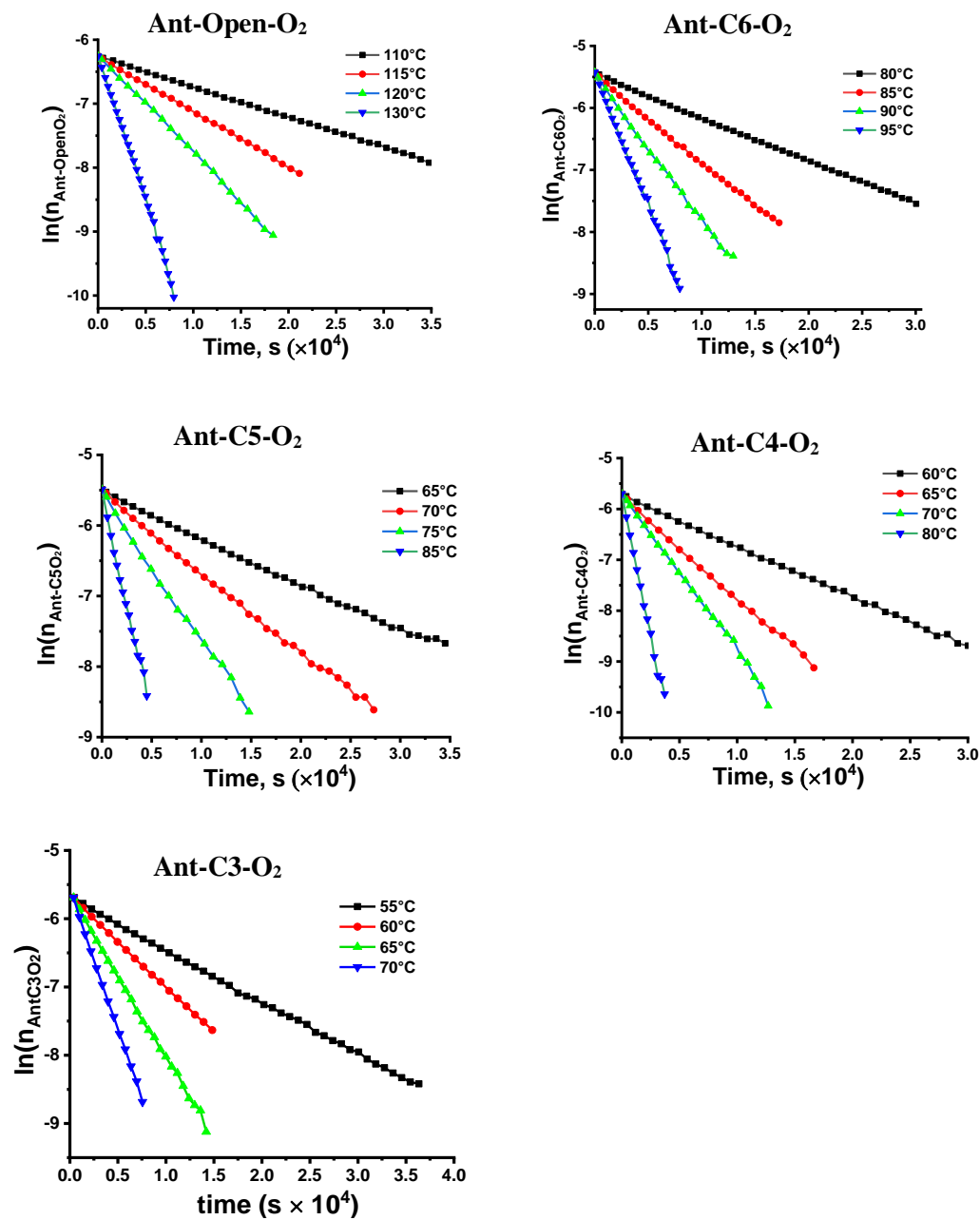


Figure S51. Rate constant determination of the retro-Diels-Alder reaction at different temperatures.

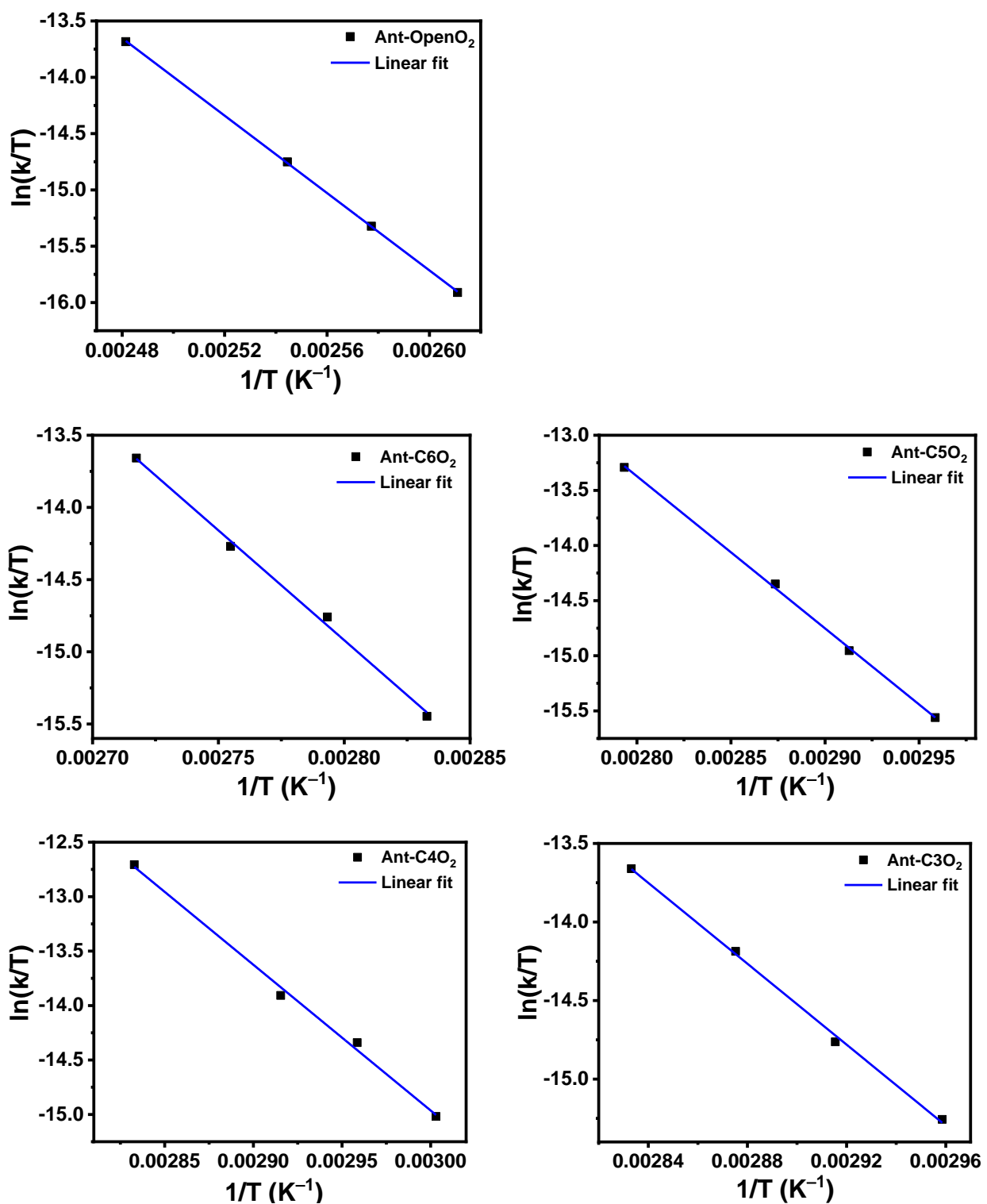


Figure S52. Eyring plot for the thermal retro Diels-Alder reactions of twistacene peroxides.

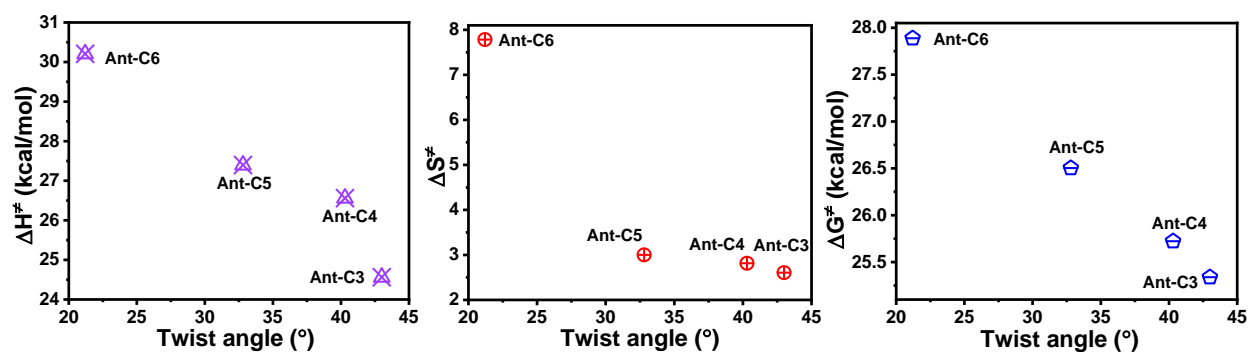


Figure S53. Experimental kinetic parameters of the thermal retro Diels-Alder reaction; (a) activation enthalpy (ΔH^\ddagger), (b) entropy (ΔS^\ddagger), and (c) Gibbs free energy (ΔG^\ddagger).

S7 Single crystal X-ray diffraction crystallography (SCXRD)

Single crystals of **Ant-C5-O₂** and **Ant-Open-O₂** were grown in a mixture of chloroform/hexane by the slow evaporation method. A single crystal of the peroxide was mounted onto a 400/50 MicroMesh™ with NVH Oil,^[2] and transferred to a Bruker SMART APEX CCD X-ray diffractometer equipped with a graphite-monochromator. The diffractogram for **Ant-C5-O₂** was recorded at 150 K using a Bruker KRYOFLEX nitrogen cryostat, whereas **Ant-Open-O₂** was recorded at room temperature. The system was controlled by a Pentium-based PC running the SMART software package.^[3] Data were collected using Mo-K α radiation ($\lambda=0.71073$ Å). The recorded raw data frames were subjected to integration and reduction by the SAINT program package.^[4] The structure was solved and refined by the SHELXTL software package.^[5]

Table S3. Crystal data and structure refinement for **Ant-C5-O₂** and **Ant-Open-O₂**.

Parameters	Ant-C5O₂	Ant-OpenO₂
Identification code	OriGi37LLT	OriGi34b
Empirical formula	C ₄₇ H ₃₀ F ₁₂ O ₄	C ₄₄ H ₂₆ F ₁₂ O ₄
Formula weight	886.71	846.65
Temperature/K	150.0(2)	283(18)
Crystal system	orthorhombic	triclinic
Space group	P2 ₁ 2 ₁ 2 ₁	P-1
a/Å	8.0911(4)	11.3632(4)
b/Å	30.0317(14)	11.7584(4)
c/Å	16.3685(6)	14.3144(4)
α /°	90	74.764(3)
β /°	90	89.892(3)
γ /°	90	83.317(3)
Volume/Å ³	3977.4(3)	1832.01(11)
Z	4	2
$\rho_{\text{calc}}/\text{cm}^3$	1.481	1.535
μ/mm^{-1}	0.131	0.139
F(000)	1808.0	860.0

Crystal size/mm³	0.372 × 0.06 × 0.027	0.147 × 0.054 × 0.024
Radiation	Mo K α (λ = 0.71073)	Mo K α (λ = 0.71073)
2θ range for data collection/°	4.77 to 51.998	4.018 to 61.156
Index ranges	-9 ≤ h ≤ 9, -37 ≤ k ≤ 36, -20 ≤ l ≤ 20	-16 ≤ h ≤ 16, -16 ≤ k ≤ 12, -19 ≤ l ≤ 19
Reflections collected	28259	22791
Independent reflections	7811 [R _{int} = 0.1091, R _{sigma} = 0.1022]	8787 [R _{int} = 0.0592, R _{sigma} = 0.0828]
Data/restraints/parameters	7811/0/568	8787/0/597
Goodness-of-fit on F²	1.025	1.033
Final R indexes [I ≥ 2σ (I)]	R ₁ = 0.0967, wR ₂ = 0.2441	R ₁ = 0.0881, wR ₂ = 0.1975
Final R indexes [all data]	R ₁ = 0.1353, wR ₂ = 0.2644	R ₁ = 0.1965, wR ₂ = 0.2423
Largest diff. peak/hole / e Å⁻³	0.50/-0.38	0.49/-0.21
CCDC deposition number	1982853	1989525

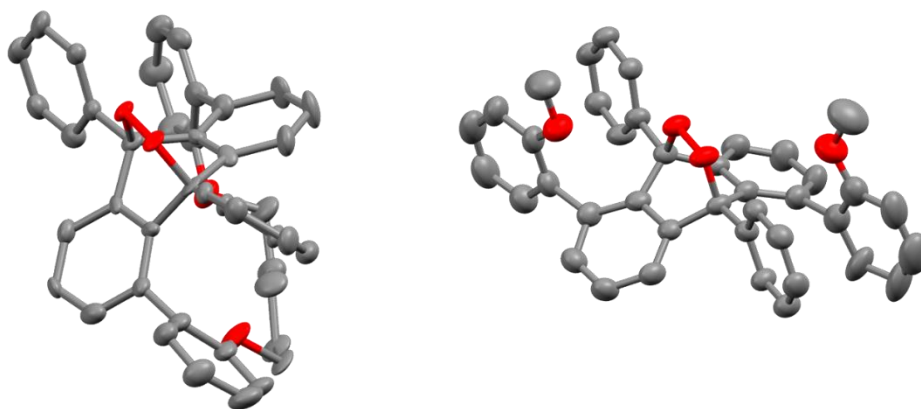


Figure S55. Ellipsoid representation (50%) probability of the single X-ray structure of Ant-C5-O₂ (left) and Ant-open-O₂ (right). Hydrogens and trifluoromethyl groups are omitted for clarity.

S8 Computational analysis of the twistacene peroxides

All calculations were carried out using the Gaussian 16 program applying density functional theory (DFT). All molecules were optimized using a hybrid density functional ^[9] and Becke's three-parameter exchange functional combined with the LYP correlation functional (B3LYP) ^[10] and with the 6-31G(d) basis set (B3LYP/6-31G(d)). Frequency calculations were performed at the same level of theory as geometry optimization for all stationary points to differentiate them as minima or saddle points. The UV spectra were simulated from time-dependent density functional theory (TDDFT) using the CAM-B3LYP functional and the 6-31G(d) basis set.

Table S4. Optimized structures of the peroxides.

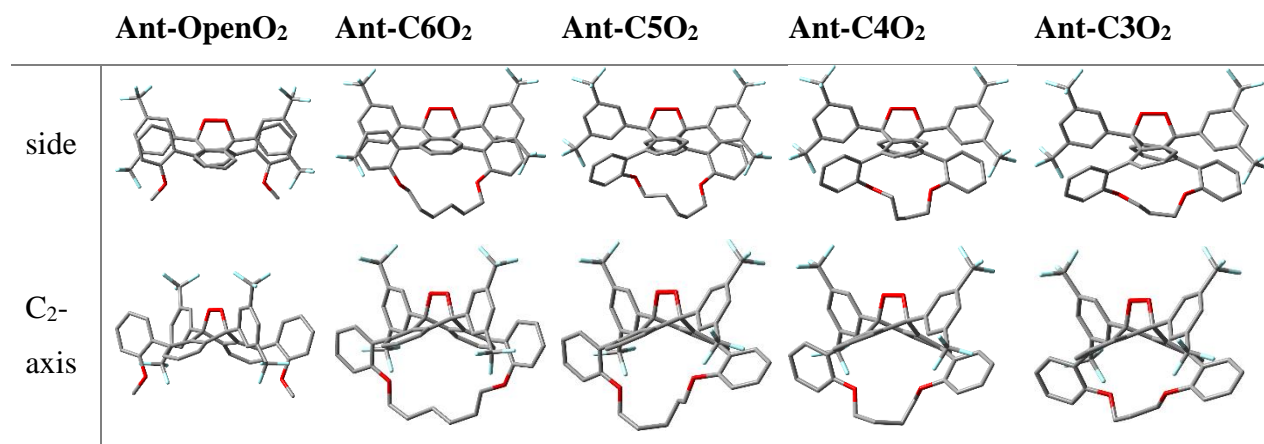
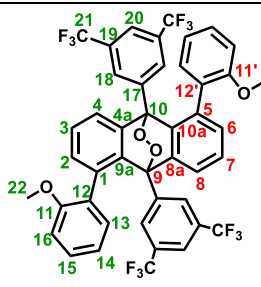
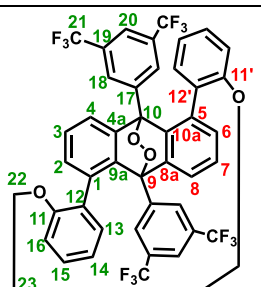
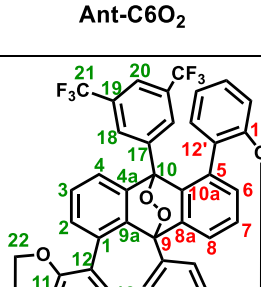
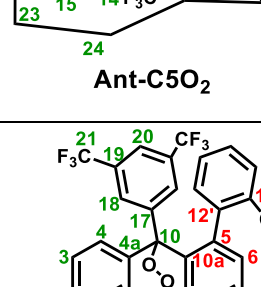


Table S5. Dihedral angles (ϕ) inside the anthracene-peroxide core

Compounds	$\phi_{9a-4a-10a-8a}$ ($^{\circ}$)	$\phi_{1-4-5-8}$ ($^{\circ}$)	$\phi_{2-3-6-7}$ ($^{\circ}$)
 <p>Ant-OpenO₂</p>	8.23	12.61	14.44
 <p>Ant-C6O₂</p>	4.40	7.58	8.67
 <p>Ant-C5O₂</p>	11.88	19.48	22.55
 <p>Ant-C4O₂</p>	13.94	23.29	27.02

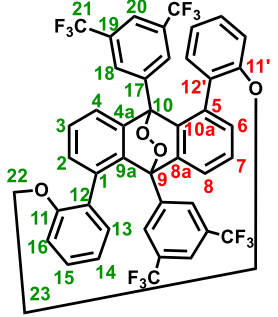
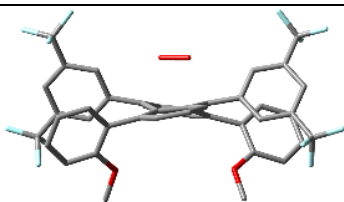
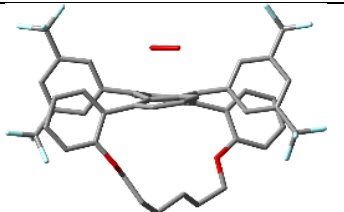
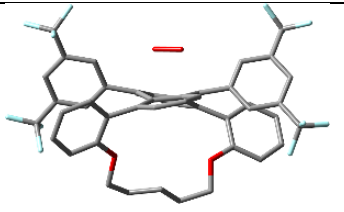
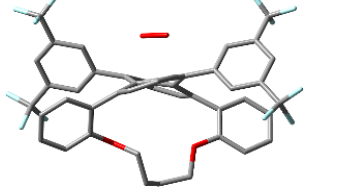
 <p>Ant-C3O₂</p>	14.87	24.81	28.76
---	-------	-------	-------

Table S6. Optimized (B3LYP-6-31G(d)) transition state (TS) in the reaction between the twistacenes and singlet oxygen ($^1\Delta_g$) and the relevant twistacene dihedral angles (ϕ) in the TS

Reactants	Optimized TS	$\phi_{9a-4a-10a-8a}$ ($^\circ$)	$\phi_{1-4-5-8}$ ($^\circ$)
Ant-Open + O₂		10.92	18.06
Ant-C6 + O₂		9.52	15.34
Ant-C5 + O₂		12.81	21.78
Ant-C4 + O₂		15.89	28.34

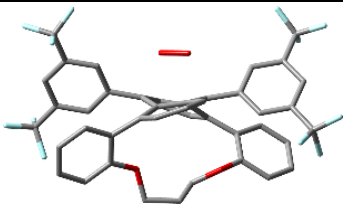
Ant-C3 +O₂		16.87	30.44
------------------------------	---	-------	-------

Table S7. Dihedral angles (ϕ) between the conjugated biaryl units in the peroxides

	$\phi_{11-12-1-2}(^{\circ})$	$\phi_{11-12-1-9a}(^{\circ})$	$\phi_{11'-12'-5-6}(^{\circ})$	$\phi_{11'-12'-5-10a}(^{\circ})$
Ant-Open-O₂	-65.05	122.56	-65.07	122.55
Ant-C6-O₂	-65.79	114.29	-84.22	92.26
Ant-C5-O₂	-111.08	59.97	-86.65	90.98
Ant-C4-O₂	-104.67	66.29	-92.71	78.84
Ant-C3-O₂	-109.47	62.10	-104.25	-67.00

Table S8. Angle (θ) in the optimized peroxides and the length of the peroxy ($\text{O}_1\text{-O}_2$) bond (d)

	Ant-Open-O ₂	Ant-C6-O ₂	Ant-C5-O ₂	Ant-C4-O ₂	Ant-C3-O ₂
$\theta_{9a-9-8a}(^\circ)$	109.40	110.70	109.92	110.77	110.41
$\theta_{4a-10-10a}(^\circ)$	109.40	110.34	110.68	110.06	110.52
$d(\text{O}_1\text{-O}_2)$ (Å)	1.46005	1.45552	1.45266	1.45458	1.45340

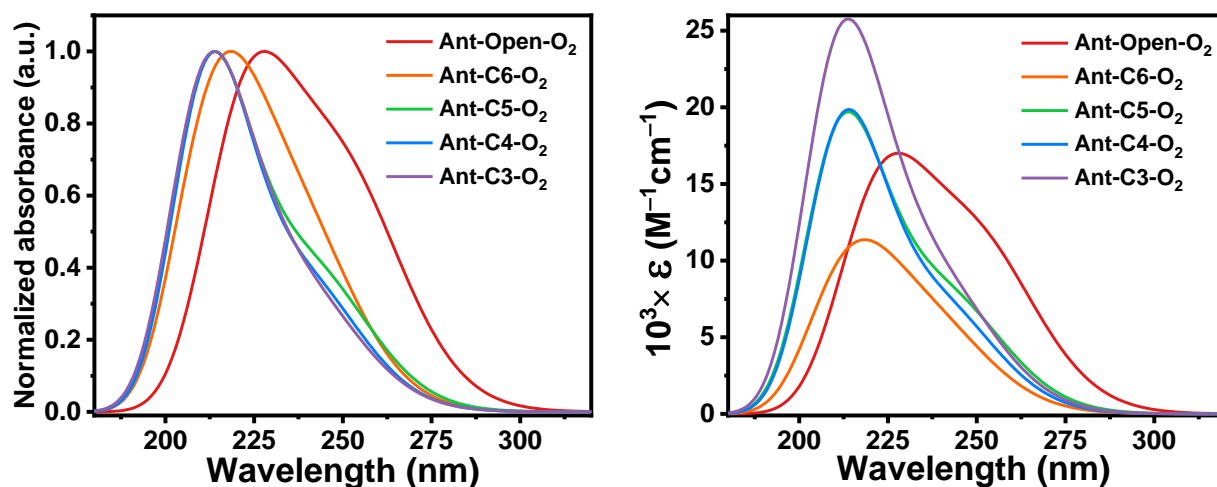


Figure S54. The computational (CAM-B3LYP-6-31G(d)) UV-vis spectra of the twistacene peroxides.

Effect of tether on strain in the tethered anthracene-peroxide core

To analyze the isolated effect of tether length on dihedral angle in the anthracene peroxide core, the **Ant-Cn-O₂'** series was optimized by retaining geometric constraints identical to those on the most reactive part of the corresponding optimized **Ant-Cn-O₂** series members. All other substituents in their parent molecules, the **Ant-C-nO₂** series, were replaced with hydrogen atoms. The variation in strain (Figure S56) arising from variation in tether length could thus be isolated from other steric factors in the actual reactions involving the **Ant-Cn-O₂** series.

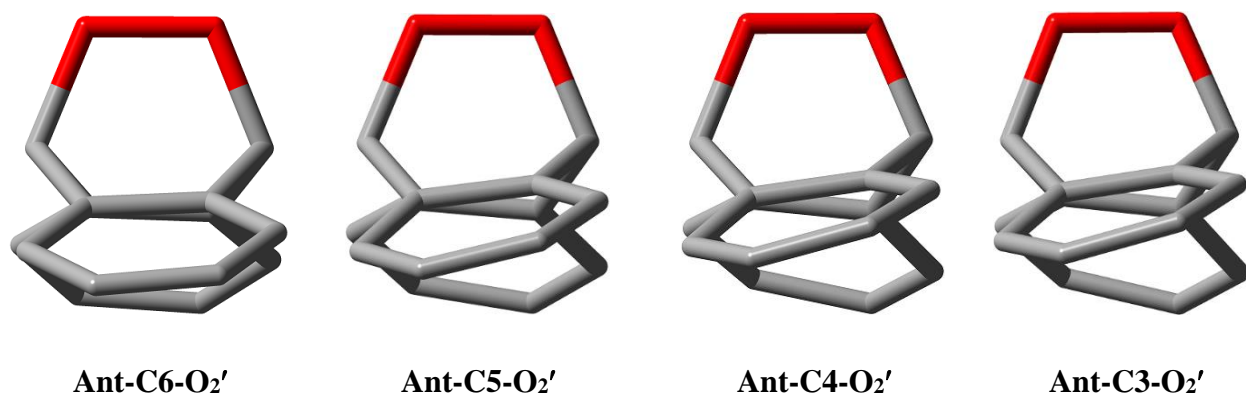


Figure S55. Optimized structures of the **Ant-CnO₂'** series.

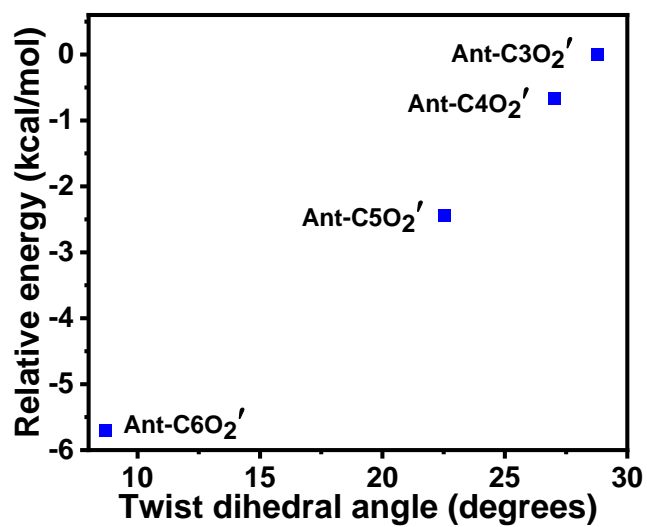


Figure S56. Relative energy of the optimized **Ant-Cn-O₂'** series.

Table S9. Imaginary frequency at the transition state of the photooxidation reaction between singlet twistacene and ¹O₂

Structure	Imaginary frequency (cm ⁻¹)
Ant-Open + ¹O₂	– 65.83
Ant-C6 + ¹O₂	– 36.22
Ant-C5 + ¹O₂	– 57.13
Ant-C4 + ¹O₂	– 94.75
Ant-C3 + ¹O₂	– 77.35

Table S10. Energy of the optimized reactants and products of the photochemical reaction

Molecules	Energy (Hartree)
Oxygen ($^1\Delta_g$)	-150.2574243
Ant-Open	-3040.9062444
Ant-Open-O₂	-3191.2260027
TS (Ant-Open + O ₂)	-3191.1780899
Ant-C6	-3196.9567630
Ant-C6O₂	-3347.2750468
TS (Ant-C6 + O ₂)	-3347.2283569
Ant-5	-3157.6401138
Ant-C5-O₂	-3307.9556000
TS (Ant-C5 + O ₂)	-3307.9216118
Ant-C4	-3118.3242830
Ant-C4-O₂	-3268.6363445
TS (Ant-C4 + O ₂)	-3268.5966119
Ant-C3	-3079.0088599
Ant-C3-O₂	-3229.3223518
TS (Ant-C3 + O ₂)	-3229.2816816

Table S11. Orbital coefficients for the HOMO level of carbons 9 and 10 for the HOMO in the transitions states of **Ant-C3** and **Ant-C6**.

Ant-C6			Ant-C3		
AO	Coefficients at HOMO level for carbons 9 and 10		AO	Coefficients at HOMO level for carbons 9 and 10	
1S	0.00449	0.00447	1S	0.00782	0.00758
2S	0.00021	0.00045	2S	0.00718	0.00634
2PX	0.02085	0.01931	2PX	0.03425	0.03316
2PY	0.07326	0.07324	2PY	0.08081	0.08369
2PZ	0.01903	0.00076	2PZ	0.01139	0.00817
3S	0.07379	0.06751	3S	0.10004	0.09887
3PX	0.02098	0.01405	3PX	0.02201	0.01998
3PY	0.08307	0.07572	3PY	0.08257	0.08395
3PZ	0.00537	0.03343	3PZ	0.00086	0.00546
4XX	0.00212	0.00218	4XX	0.00233	0.00229
4YY	0.00254	0.00135	4YY	0.00238	0.00186
4ZZ	0.00281	0.00154	4ZZ	0.00212	0.00171
4XY	0.00139	0.00157	4XY	0.00108	0.00101
4XZ	0.00011	0.00008	4XZ	0.00095	0.00106
4YZ	0.00161	0.00294	4YZ	0.00388	0.00423
Sum of coefficients	0.311	0.299	Sum of coefficients	0.36	0.36

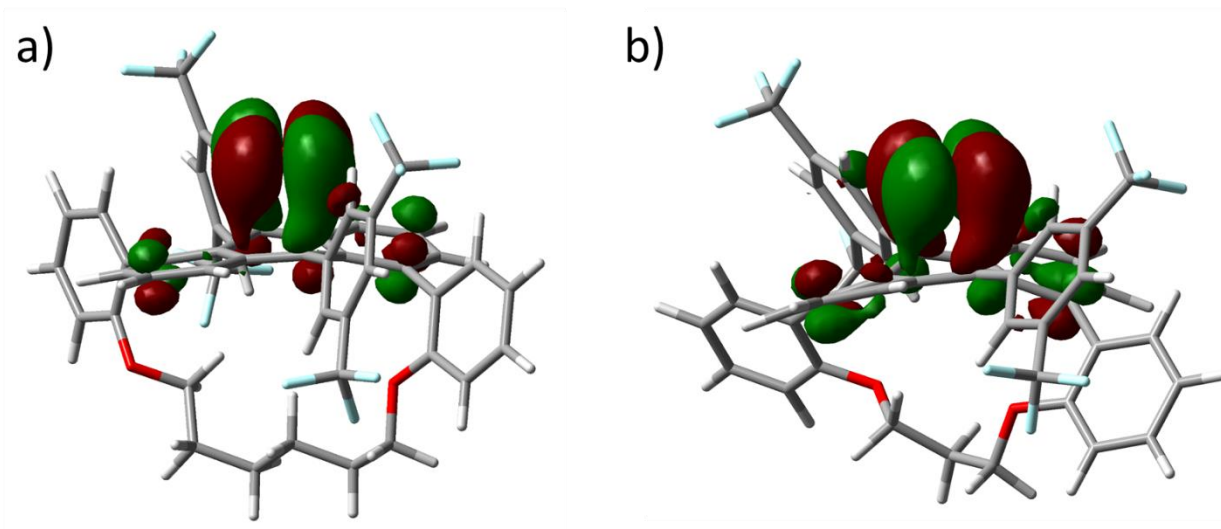


Figure S59. HOMO surfaces of the calculated transition state for (a) **Ant-C6** and (b) **Ant-C3**.

S9 References

- [1] Bedi, A.; Shimon, L. J. W.; Gidron, O., Helically Locked Tethered Twistacenes. *J. Am. Chem. Soc.* **2018**, *140*, 8086-8090.
- [2] MiTeGen, LLC P.O. Box 3867 Ithaca, NY 14852.
- [3] SMART-NT V5.6, BRUKER AXS GMBH, D-76181 Karlsruhe, Germany, **2002**.
- [4] SAINT-NT V5.0, BRUKER AXS GMBH, D-76181 Karlsruhe, Germany, **2002**.
- [5] SHELXTL-NT V6.1, BRUKER AXS GMBH, D-76181 Karlsruhe, Germany, **2002**.
- [6] Gaussian 16, Revision B.01, Frisch, M. J.; Trucks, G. W.; Schlegel, H. B.; Scuseria, G. E.; Robb, M. A.; Cheeseman, J. R.; Scalmani, G.; Barone, V.; Petersson, G. A.; Nakatsuji, H.; Li, X.; Caricato, M.; Marenich, A. V.; Bloino, J.; Janesko, B. G.; Gomperts, R.; Mennucci, B.; Hratchian, H. P.; Ortiz, J. V.; Izmaylov, A. F.; Sonnenberg, J. L.; Williams-Young, D.; Ding, F.; Lipparini, F.; Egidi, F.; Goings, J.; Peng, B.; Petrone, A.; Henderson, T.; Ranasinghe, D.; Zakrzewski, V. G.; Gao, J.; Rega, N.; Zheng, G.; Liang, W.; Hada, M.; Ehara, M.; Toyota, K.; Fukuda, R.; Hasegawa, J.; Ishida, M.; Nakajima, T.; Honda, Y.; Kitao, O.; Nakai, H.; Vreven, T.; Throssell, K.; Montgomery, J. A., Jr.; Peralta, J. E.; Ogliaro, F.; Bearpark, M. J.; Heyd, J. J.; Brothers, E. N.; Kudin, K. N.; Staroverov, V. N.; Keith, T. A.; Kobayashi, R.; Normand, J.; Raghavachari, K.; Rendell, A. P.; Burant, J. C.; Iyengar, S. S.; Tomasi, J.; Cossi, M.; Millam, J. M.; Klene, M.; Adamo, C.; Cammi, R.; Ochterski, J. W.; Martin, R. L.; Morokuma, K.; Farkas, O.; Foresman, J. B.; Fox, D. J. Gaussian, Inc., Wallingford CT, **2016**.
- [9] (a) Parr, R. G.; Yang, W. Density-functional Theory of Atoms and Molecules, Oxford University Press, New York, **1989**. (b) Koch, W.; Holthausen, M. C. A Chemist's Guide to Density Functional Theory, Wiley-VCH, New York, **2000**.
- [10] Lee, C.; Yang, W.; Parr, R. G. Phys. Rev. B 1988, 37, 785. (b) Becke, A. D. J. Chem. Phys. **1993**, 98, 5648.